WILLIAM & MARY

CHARTERED 1693

Dissertations, Theses, and Masters Projects   Theses, Dissertations, & Master Projects

2018

Dynamics of Systems With Hamiltonian Monodromy

Daniel Salmon

College of William and Mary - Arts & Sciences, dasalmon99@gmail.com

Follow this and additional works at: https://scholarworks.wm.edu/etd

Part of the Physics Commons

Dynamics of Systems with Hamiltonian Monodromy

Daniel Salmon
Apex, North Carolina

Master of Science, College of William & Mary, 2014
Bachelor of Science, North Carolina State University, 2012

A Dissertation presented to the Graduate Faculty
of The College of William & Mary in Candidacy for the
Degree of Doctor of Philosophy

Department of Physics

College of William & Mary
August 2018

APPROVAL PAGE

This Dissertation is submitted in partial fulfillment of
the requirements for the degree of

Doctor of Philosophy

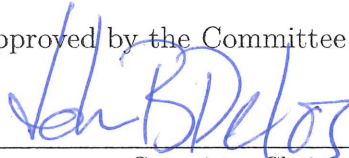_Daniel Salmon_
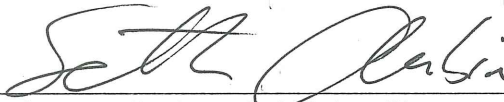
Approved by the Committee July 2018

Committee Chair
Professor John Delos, Physics
College of William & Mary

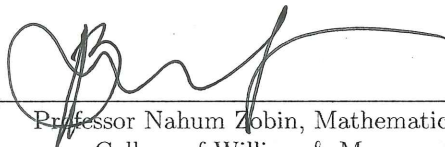Associate Professor Seth Aubin, Physics
College of William & Mary

Professor William Cooke, Physics
College of William & Mary

CSX Professor Dennis Manos, Physics and Applied Science
College of William & Mary

Professor Nahum Zobin, Mathematics
College of William & Mary

ABSTRACT

A system is said to have monodromy if, when we carry the system around a closed circuit, it does not return to its initial state. The simplest example is the square-root function in the complex plane. A Hamiltonian system is said to have Hamiltonian monodromy if its fundamental action-angle loops do not return to their initial topological state at the end of a closed circuit. These changes in topology of angle loops carry through to other aspects of these systems, including the classical dynamics of families of trajectories, quantum spectra and even wavefunctions. This topological change in the evolution of a loop of classical trajectories has been observed experimentally for the first time, using an apparatus consisting of a spherical pendulum subject to time-varying potentials and torques. Presented in this dissertation are the details of this experiment, as well as theoretical calculations on a novel system: a double welled Mexican-hat system with two monodromy points.

This is part of a more general research program that is concerned with the Lagrangian torus fibration of the phase spaces of integrable Hamiltonian systems. In this paradigm, calculations on the double welled system are carried out. In this dissertation, static and dynamical manifestations of monodromy are shown to exist for this system. It has been shown previously that corresponding topological changes occur in wavefunctions of systems with monodromy. Here it is shown that results of quantum wavefunction monodomy carry over intuitively.

TABLE OF CONTENTS

ACKNOWLEDGEMENTS

I would like to thank my advisor John Delos for the years of guidance he has given during my time at William & Mary. By example, he has taught me to think more independently and not be discouraged by setbacks in research. Feeling lost just means you're doing something new and (perhaps) interesting, and I want to thank John for showing me that. I would also like to thank him and Sue for their hospitality throughout these years. When you work for John, you really do feel a part of the family.

Professor Seth Aubin has been a wonderful collaborator and I would like to thank him for his help on the experimental side of this dissertation. Not many people would jump at the prospect of helping theorists do an experiment, and it is in large part due to his experience and advice that our experiment succeeded.

Thank you to the rest of my committee members, Professors Cooke, Manos and Zobin, for their thoughtful advice throughout my time at William & Mary. An additional thank you to Professor Manos, without whom the monodromy experiment would not have been possible.

Thank you to Perry Nerem for not only being a superb partner in research, but for being a good and loyal friend. Thank you to Dr. Chen Chen for her work on these subjects and for her part in making Delos lab a fun and exciting research group.

Thank you Paula, Carol and Ellie for their hard work in keeping the department running. I would not be defending without them, if only because I may have just forgotten to do it.

My gratitude to all of the friends I have made in Williamsburg these last few years, both in and out of the William & Mary Dept. of Physics, for encouraging me when things were not so easy.

Thank you Carlie Crawford, whose love and support have been paramount in keeping me going.

And lastly, thank you to my family, for always encouraging me to pursue my goals. Without them, I would not be here today.

This dissertation is dedicated to my family and friends, who have been waiting and supporting me these last 6 years.

LIST OF TABLES

LIST OF FIGURES

Chapter 1

Introduction

1.1 General Introduction

Classical mechanics is an old subject in which new physics seldom appears. However, a body of recent work is developing on a group of phenomena collectively called *Hamiltonian monodromy.* In brief, it has been found that in a number of systems, action and angle variables are not uniquely defined, and that when we go around certain monodromy circuits, those variables do not come back to their original forms or values. In those cases, action and angle variables are multivalued functions, possessing branch points, and when we continue these variables smoothly on a closed circuit passing around such a branch point, they then correspond to a different state of the system. As a consequence, certain families of classical paths change their topological structure when going around such monodromy circuits.

Monodromy was first introduced theoretically [1] as a change in the topology of action-angle coordinates in the "champagne bottle" system. Since then it has been shown to exist in many physical systems, including the symmetric top and spherical pendulum [2], a top in a fluid [3], and a resonant swing-spring [4]. This classical phenomenon was extended to quantum mechanics [5]. Because action variables are multivalued, their corresponding quantum numbers are multivalued, so there is no unique assignment of quantum numbers to quantum states. The most visible

manifestation of this is a spatial defect in the lattice of eigenvalues. This lattice defect is the archetypal example of the effect of monodromy on the global structure of a quantum system.

This quantum manifestation of monodromy has been predicted theoretically in the energy spectra of atomic hydrogen [6–10], ellipsoidal billiards [11], H_2^+ and HHe^{2+} [12], H_2O and quasi-linear molecules [13], dipolar molecules in electric fields [14, 15], the quantum swing-spring [16], which is a model for the CO_2 molecule [17], and trapped Bose gases [18]. Related phenomena have also been characterized[1], such as "fractional monodromy" [19, 20], "bidromy" [21, 22], and the combination thereof, predicted in HOCl [23]. Monodromy also shows up in collective vibrations of nucleons in bound nuclei(interacting boson model) [24], attractors in theories of nonlinear waves [25] and, most recently, Dicke superradiance [26].

A distinction has been made between static and dynamical manifestations of monodromy [27] [28]. The above are called "static" manifestations of monodromy; they arise from smooth connections of action-angle coordinates on families of static phase-space tori that are present in integrable classical systems. "Dynamical" manifestations of monodromy are analogous topological changes in loops of particles that occur as a system evolves in time [27–29]. We apply a time dependent perturbation to a loop of particles in a system with monodromy, and follow the loop as it evolves in time. The cloud of particles is initially aligned along a canonical angle loop and traverses a monodromy circuit. These particles will display the same topological change associated with static monodromy, namely the topological change of the angle loop itself. This change is classical dynamical monodromy.

Quantum static monodromy has been demonstrated in the spectra of some molecular systems [30], and, previous to the work contained herein, there appears to be only one measurement on a classical system that displayed static manifestations of monodromy [31]. A significant portion of this thesis is dedicated to an experimental recreation

---

[1] "Berry phase jumps" found in graphene also have some similarities to Hamiltonian Monodromy. See J. F. Rodriguez-Nieva and L. S. Levitov, Phys. Rev. B 94, 235406 (2016).

of the prototypical monodromy system: particles moving in a champagne bottle potential. The dynamical consequences of monodromy in this system have been discussed theoretically [27–29] and new experimental results are in Chapter 5.

1.2 Theory Introduction

Before we can continue, we must establish the necessary theoretical concepts required to understand monodromy, namely Lagrangian manifolds and action-angle coordinates. The theory leading to action and angle variables involves considerable effort, so let us begin by saying that the utility of these variables derives from the following facts. (All of these points are developed in the later chapters, particularly Chapter 2, which establishes much of the background theory).

1. We examine Hamiltonian systems having N degrees of freedom, described by coordinates and momenta $(q_1...q_N, p_1...p_N) = (\mathbf{q}, \mathbf{p})$ in which there are N conserved quantities, $\{F_i(\mathbf{q}, \mathbf{p}), i = 1...N\}$. The Hamiltonian $H(\mathbf{q}, \mathbf{p})$ of the system must either be one of the F_i's, or a function of some or all of them.

2. Under general conditions, the points in phase space corresponding to fixed values of all the F's (the set of points such that $\{F_i(\mathbf{q}, \mathbf{p}) = \mathbf{constant}_i, i = 1...N\}$ lie on an N-dimensional torus in the 2N-dimensional phase space.

3. From those conserved quantities, it is possible to construct a set of action variables $\{I_k(\mathbf{q}, \mathbf{p}), k = 1...N\}$, which depend on phase space coordinates only through their dependence on the set of functions $F_i(\mathbf{q}, \mathbf{p})$, so they are also conserved. Those action variables must be independent functions only of the F_i's, and therefore the Hamiltonian can also be expressed as a function of the actions, $H(\mathbf{q}, \mathbf{p}) = \mathcal{H}(\mathbf{I}(\mathbf{q}, \mathbf{p}))$.

4. The actions I_k have a set of canonically conjugate angles ϕ_k, so Hamilton's equations of motion can be written in the form

$$\frac{dI_k}{dt} = -\frac{\partial \mathcal{H}}{\partial \phi_k} = 0 \tag{1.1a}$$

$$\frac{d\phi_k}{dt} = \frac{\partial \mathcal{H}}{\partial I_k} = \omega(I_1...I_k) = \mathbf{constant} \tag{1.1b}$$

5. When ϕ_k increases by 2π holding the other ϕ's fixed, the path traces out a fundamental loop on the torus.

6. There is a canonical transformation between the original variables $(\mathbf{q}, \mathbf{p})$ and this set of action and angle variables $(\mathbf{I}, \phi)$. In this transformation, each of the original variables $(\mathbf{q}, \mathbf{p})$ and any function of them must be a periodic function of the angles, with period 2π. Explicit forms for action-angle variables are given in Section 2.9.3.

Beyond just monodromy, further utility of action-angle variables derives from the following propositions.

A. Action variables are adiabatic invariants. If the system Hamiltonian is explicitly time dependent but changes sufficiently slowly, then we can look at the tori of H at each fixed time, and the trajectory of the system $(\mathbf{q}(t), \mathbf{p}(t))$ will move along and through these tori in such a manner that the numerical values of the action variables are, to good approximation, constant. In other words, the system point $(\mathbf{q}(t), \mathbf{p}(t))$ moves from one torus of the initial Hamiltonian $H(\mathbf{q}, \mathbf{p}, t_i)$ to a torus of the final Hamiltonian $H(\mathbf{q}, \mathbf{p}, t_f)$ and these tori have nearly the same numerical value of their action variables. Proposition (A) is "proved" to the satisfaction of physicists in various textbooks of classical mechanics for systems with one degree of freedom, and it has been found in numerical calculations to be useful for systems with more degrees of freedom.

B. Quantum eigenvalues of a physical system can be found approximately by identifying "eigentori," tori having quantized values of action variables

$$I_k = (n_k + \frac{\mu_k}{4})\hbar \qquad (1.2)$$

This formula is a corrected Bohr-Sommerfeld condition, and it gives accurate eigenvalues of quantum systems when the wavelength is short (and exact eigenvalues for particular systems, such as the quantum harmonic oscillator and hydrogen atom). (n_k is a positive integer, and μ_k is an integer called the Maslov index, frequently 0, 2, or 4.)

In short, while action-angle variables are not necessarily easy to obtain, they give

the simplest possible description of the motion, they provide adiabatic invariants, and they provide approximate quantum eigenvalues and eigenfunctions. With this general framework of how to obtain action and angle variables and associated quantities, we can look at exceptional cases to the underlying conditions in point 2 above. This work is part of a research program that aims to understand the Lagrangian torus fibration of the phase space of integrable Hamiltonian systems.

Let $\mathbf{f}$ be an element of the image of $\mathbf{F} = \{F_i(\mathbf{q}, \mathbf{p}), i = 1...N\}$ and consider the fiber $\mathbf{F}^{-1}(\mathbf{f})$. By the Liouville-Arnol'd theorem, if $\mathbf{f}$ is a regular value, $\mathbf{F}^{-1}(\mathbf{f})$ is a smooth torus $\mathbf{T}^2$ or a union of such tori. This type of information is encoded in the space of level sets, often called a "bifurcation diagram" BD or "spectrum space". All the elements of the image of $\mathbf{F}$ are depicted in the BD and for each value $\mathbf{f}$, the BD shows whether $\mathbf{f}$ is regular or critical, and the type of the fiber $\mathbf{F}^{-1}(\mathbf{f})$.

The basic topological obstruction to the existence of global actions is non-trivial monodromy of the $\mathbf{T}^2$ fiber bundle over $\mathbf{R}$, a connected set of regular values of $\mathbf{F}$. In this case, each fiber of spectrum space is regular except for one critical value, corresponding to a "pinched torus," see Fig. 1.1. This system has non-trivial monodromy due to this singular value and thus no global action-angle coordinates exist.

This standard notion of monodromy has been recently generalized to fractional monodromy. The main difference between standard and this generalized monodromy is that, in the latter, there exists a line C of critical values of $\mathbf{F}$ that correspond to curled tori, see [32]. Thus in fractional monodromy interest is not restricted to the fibration of the phase space over the set R of regular values of $\mathbf{F}$, but is extended to include also sets of critical values of $\mathbf{F}$. Furthermore, this leads naturally to the question of the behavior of the action variables near the line C of critical values of $\mathbf{F}$ [33, 34]. Another generalized monodromy, called bidromy, was proposed in [22]. Bidromy has the defining characteristic of 2-DOF systems with BD's that contain a swallowtail [21], which is characterized by a line C of critical values of $\mathbf{F}$ that correspond to bitori. The system studied in Chapters 4, 6 and 8 of this dissertation closely resembles some properties of this system.
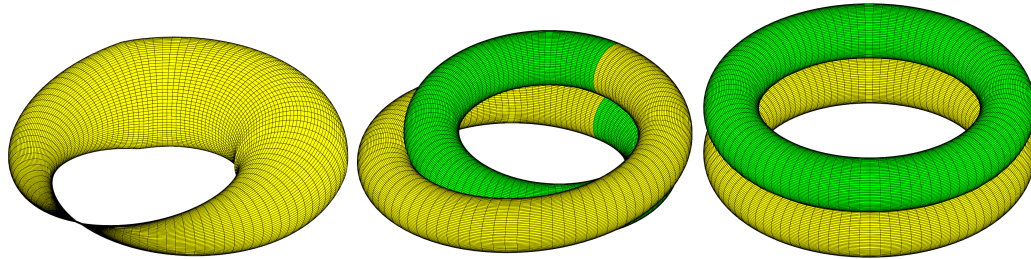
Figure 1.1: Possible singular fibers of (ℓ, h)-space for Hamiltonian systems that exhibit basic or generalized monodromy. (left) a pinched torus, associated with basic monodromy, (middle) a curled torus, associated with fractional monodromy, (right) a bitorus, associated with bidromy.

1.3   Structure of this Dissertation

Chapter 2 goes over much of the background mathematics required for derivation and understanding of monodromy and related phenomena, such as Lagrangian manifolds and action-angle variables. The material covered here, and further related examples, will be covered in a pedagogical article being prepared by Prof. J. B. Delos, with revisions and additional proofs provided by Perry Nerem and Daniel Salmon.

The rest of this dissertation deals with two different systems, the first being particles moving in a Mexican-hat potential, see Sec. 3.1. The second system is a double welled Mexican-hat, a system that has two monodromy points, see Sec. 4.1.

Static Monodromy	Dynamical Monodromy	Quantum Monodromy
Mexican Hat (Ch. 3)	Mexican Hat (Expt.) (Ch. 5)	Mexican Hat (Ch. 7)
Double Well (Ch. 4)	Double Well (Ch. 6)	Double Well (Ch. 8)

Table 1.1: Dissertation Structure

Chapters 3 and 4 show static manifestations of monodromy of each of these systems. Chapters 5 and 6 discuss dynamical monodromy of both systems theoretically, as well as an experimental implementation that was used to observe dynamical monodromy in a Mexican-hat system. Finally, Chapters 7 and 8 discuss the quantum analogues of these systems and show monodromy of wavefunctions for the double well system. For a quick reference of the structure of this dissertation, see Table 1.1. The portions of

this dissertation that contain significant original research are Chapters 4, 5, 6 and 8.

Chapter 2

Dynamics and Symplectic Geometry

In this chapter, we will be describing the geometry of phase space and the dynamics required to understand monodromy. Many of the ideas and equations presented in this section are taken from a pedagogical paper originally prepared by Prof. J. B. Delos, with revisions provided by Perry Nerem and Daniel Salmon.

We will be discussing flows in a $2N$-dimensional phase space $\mathbf{z} = (\mathbf{q}, \mathbf{p})$ generated by a function which is treated as if it were (and often is) a Hamiltonian of a physical system. More generally, we might have a collection of flows generated by a set of N functions $F_i(\mathbf{q}, \mathbf{p})$ whose mutual Poisson brackets (defined in 2.5) all vanish. It is by using the geometry of such flows that we will come to construct action-angle variables on Lagrangian manifolds in phase space, which are the essential concepts for discussing monodromy. For each system in future chapters of this dissertation, $N = 2$ and the F's will consist of $\{F_i(p, q) | i = 1 \cdots N\} = \{H(p, q), L(p, q)\}$, where H and L are the Hamiltonian and angular momentum functions, respectively. However, we will continue discussing the more general framework for now.

2.1 Geometric Constructs in Phase Space

Dynamics is described in a phase space Ω, of dimension $2N$, locally diffeomorphic to a domain of Cartesian space $\mathbb{R}^{2N}$, having coordinates

$$(z_1 \cdots z_{2N}) = (q_1, \cdots, q_n, p_1, \cdots p_N) \tag{2.1a}$$

collected into a column vector

$$\mathbf{z} = \begin{pmatrix} \mathbf{q} \\ \mathbf{p} \end{pmatrix} \tag{2.1b}$$

The dynamical system is defined by an autonomous set of differential equations,

$$\frac{d\mathbf{z}}{dt} = \begin{pmatrix} \dot{\mathbf{q}} \\ \dot{\mathbf{p}} \end{pmatrix} = \mathbf{G}(\mathbf{z}), \tag{2.2a}$$

which define a *velocity vector field* in phase space. Integration of which defines a *flow* in phase space,

$$\mathbf{z}(t; \mathbf{z}^0) = \mathbf{z}^0 + \int_0^t \mathbf{G}(\mathbf{z}(t'; \mathbf{z}^0)) dt' \tag{2.2b}$$

The equations of motion tell us that at every point $\mathbf{z}$, there is a $2N$-dimensional velocity vector $\dot{\mathbf{z}} = \mathbf{G}(\mathbf{z})$ which is an element of a velocity space, the tangent space to phase space at the point $\mathbf{z}^0$, called $T\Omega_{\mathbf{z}^0}$. The velocity spaces are isomorphic to $\mathbb{R}^{2N}$. We define unit vectors $\hat{\dot{q}}_i$ and $\hat{\dot{p}}_i$ along the axes of this velocity space, so the velocity vector $\mathbf{v} = \dot{\mathbf{z}}$ is written in components as

$$\begin{aligned} \mathbf{v} = \dot{\mathbf{z}} &= \sum_{i=1}^N \hat{\dot{q}}_i \frac{dq_i}{dt} + \hat{\dot{p}}_i \frac{dp_i}{dt} \\ &= \sum_{i=1}^N \hat{\dot{q}}_i \, v_{q_i} + \hat{\dot{p}}_i \, v_{p_i} \end{aligned} \tag{2.3}$$

We consider systems for which the equations of motion have Hamilton's form: given

a differentiable function $H(\mathbf{q}, \mathbf{p})$, the differential equations are

$$\dot{q}_i = \frac{\partial H(\mathbf{q}, \mathbf{p})}{\partial p_i}, \dot{p}_i = -\frac{\partial H(\mathbf{q}, \mathbf{p})}{\partial q_i} \tag{2.4}$$

These equation can be written in more compact notation using the gradient. First, we note that the phase space gradient of a function $G(\mathbf{q}, \mathbf{p})$ is officially defined as a covector, and represented by

$$(\frac{\partial G}{\partial \mathbf{q}}, \frac{\partial G}{\partial \mathbf{p}}) \equiv (\frac{\partial G}{\partial q_1}, ..., \frac{\partial G}{\partial q_N}, \frac{\partial G}{\partial p_1}, ..., \frac{\partial G}{\partial p_N}) \tag{2.5}$$

However for Hamiltonian mechanics, we need the transpose of this. So we define the del operation by the corresponding column vector.

$$\nabla_z G(\mathbf{z}) = \frac{\partial G(\mathbf{z})}{\partial \mathbf{z}}\Big|_{z=\hat{z}} = \begin{pmatrix} \frac{\partial G(\mathbf{z})}{\partial \mathbf{q}} \\ \frac{\partial G(\mathbf{z})}{\partial \mathbf{p}} \end{pmatrix}\Big|_{z=\hat{z}} \tag{2.6}$$

Then Hamilton's equations take the form

$$\frac{d\mathbf{z}}{dt} = \mathbf{v}_H(\mathbf{z}) = \underline{J}\nabla_{\mathbf{z}} H(\mathbf{z})$$

$$\underline{J} = \begin{pmatrix} \underline{0} & \underline{1} \\ -\underline{1} & \underline{0} \end{pmatrix} \tag{2.7}$$

2.2   The J-Product and Symplectic Geometry

In each tangent space, $T\Omega_{\mathbf{z}^0}$, we define two scalar products: the Euclidean scalar product

$$\langle \mathbf{u}|\mathbf{v}\rangle = \sum_{k=1}^{2N} u_k v_k = \sum_{i=1}^{N} (u_{q_i} v_{q_i} + u_{p_i} v_{p_i}) \tag{2.8}$$

and the J-product

$$\langle \mathbf{u}|\underline{J}\mathbf{v}\rangle = -\langle \mathbf{v}|\underline{J}\mathbf{u}\rangle$$

$$\langle \mathbf{u}|J\mathbf{v}\rangle = \sum_{i=1}^{N} u_{q_i} v_{p_i} - u_{p_i} v_{q_i}$$

$$= \left(\begin{array}{cc} \mathbf{u_q} & \mathbf{u_p} \end{array} \right) \left(\begin{array}{cc} \underline{0} & \underline{1} \\ -\underline{1} & \underline{0} \end{array} \right) \left(\begin{array}{c} \mathbf{v_q} \\ \mathbf{v_p} \end{array} \right)$$

(2.9)

This is also called the symplectic product or the skew product. Two vectors $\mathbf{u}, \mathbf{v}$ are said to be perpendicular to each other if and only if

$$\langle \mathbf{u}|\mathbf{v}\rangle = 0 \qquad \text{perpendicular} \qquad (2.10a)$$

and they are said to be J-orthogonal to each other if and only if

$$\langle \mathbf{u}|\underline{J}\mathbf{v}\rangle = 0 \qquad J\text{-orthogonal} \qquad (2.10b)$$

The J-product is the most important element of symplectic geometry. Just as Euclidean geometry involves the study of transformations of spatial coordinates or of objects in space under which the familiar scalar product is invariant (translations, rotations, etc.), symplectic geometry is the study of transformations of phase space coordinates or geometric objects under which the J-product is invariant.

Let us also note that $\underline{\widetilde{J}} = \underline{J}^{-1}$ and $\underline{J}^2 = -\mathbf{1}$. A geometric interpretation of the J-product is shown in Fig. 2.1. As we shall see, the J-product is the most important element of the theory.

2.3 Changes of Coordinates and Canonical Transformations

There are various differentiable scalar functions $F(\mathbf{z})$ defined in phase space, and at any point $\hat{\mathbf{z}}$, we define as before the gradient vector of such a function as a column
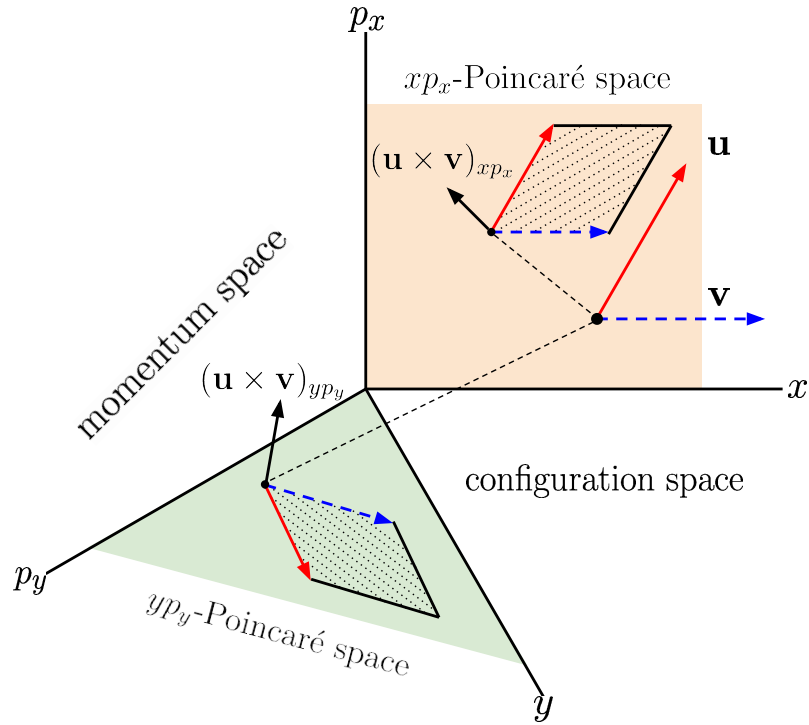
Figure 2.1: Examine two vectors in one tangent space and consider their projections onto each Poincaré plane spanned by (q_i, p_i) for $i = 1 \cdots N$. The two-dimensional cross-product of the projected vectors in each Poincaré plane is equal to the *oriented* area of the parallelogram bounded by the vectors, and the J-product is the sum of these oriented areas in the N distinct Poincaré planes.

vector having coordinates

$$\left. \frac{\partial F(\mathbf{z})}{\partial \mathbf{z}} \right|_{\mathbf{z}=\hat{\mathbf{z}}} = \begin{pmatrix} \partial F(\mathbf{z})/\partial \mathbf{q} \\[2mm] \partial F(\mathbf{z})/\partial \mathbf{p} \end{pmatrix}_{\mathbf{z}=\hat{\mathbf{z}}} \tag{2.11}$$

A set of $2N$ functions $\{Z_k(\mathbf{z}), k = 1 \cdots 2N\}$ with the first N called $Q_i(\mathbf{z})$ and the second N called $P_i(\mathbf{z})$

$$\mathbf{Z}(\mathbf{z}) = \{Z_1(\mathbf{z}) \cdots Z_{2N}(\mathbf{z})\} \tag{2.12a}$$

$$= \{Q_1(\mathbf{z}) \cdots Q_N(\mathbf{z}), P_1(\mathbf{z}) \cdots P_N(\mathbf{z})\} \tag{2.12b}$$

can form a local curvilinear coordinate system in a neighborhood of a point $\mathbf{z}^0$ in phase space, provided that the functions are independent, i.e. provided that in that neighborhood, the gradient vectors are linearly independent, or, equivalently, provided that the determinant of the Jacobian matrix

$$M_{ij}(\mathbf{z}) = \frac{\partial Z_i(\mathbf{z})}{\partial z_j} \tag{2.13a}$$

$$\underline{M}(\mathbf{z}) = \left[\frac{\partial \mathbf{Z}}{\partial \mathbf{z}} \right] = \begin{bmatrix} \frac{\partial \mathbf{Q}}{\partial \mathbf{q}} & \frac{\partial \mathbf{Q}}{\partial \mathbf{p}} \\ \frac{\partial \mathbf{P}}{\partial \mathbf{q}} & \frac{\partial \mathbf{P}}{\partial \mathbf{p}} \end{bmatrix} \tag{2.13b}$$

does not vanish in that neighborhood.

As always, any such set of $2N$ functions $\mathbf{Z}(\mathbf{z})$ can be regarded as new coordinates covering a given neighborhood of phase space, or as a mapping from one neighborhood of phase space to another. Components of velocity vectors are related by

$$\begin{pmatrix} \dot{Q} \\ \dot{P} \end{pmatrix} = \underline{M}(\mathbf{z}) \begin{pmatrix} \dot{q} \\ \dot{p} \end{pmatrix}, \quad \begin{pmatrix} \mathbf{u_Q} \\ \mathbf{u_P} \end{pmatrix} = \underline{M}(\mathbf{z}) \begin{pmatrix} \mathbf{u_q} \\ \mathbf{u_p} \end{pmatrix} \tag{2.14a}$$

whereas components of gradient vectors are related by

$$\begin{pmatrix} \frac{\partial}{\partial \mathbf{Q}} \\ \frac{\partial}{\partial \mathbf{P}} \end{pmatrix} = \tilde{\underline{M}}^{-1}(\mathbf{z}) \begin{pmatrix} \frac{\partial}{\partial \mathbf{q}} \\ \frac{\partial}{\partial \mathbf{p}} \end{pmatrix} \tag{2.14b}$$

Euclidean scalar products transform according to

$$\begin{pmatrix} \mathbf{u_q} & \mathbf{u_p} \end{pmatrix} \begin{pmatrix} \mathbf{v_q} \\ \mathbf{v_p} \end{pmatrix} = \begin{pmatrix} \mathbf{u_Q} & \mathbf{u_P} \end{pmatrix} \tilde{\underline{M}}^{-1} \underline{M}^{-1} \begin{pmatrix} \mathbf{v_Q} \\ \mathbf{v_P} \end{pmatrix} \tag{2.15}$$

while J-products transform according to

$$\begin{pmatrix} \mathbf{u_q} & \mathbf{u_p} \end{pmatrix} \underline{J} \begin{pmatrix} \mathbf{v_q} \\ \mathbf{v_p} \end{pmatrix} = \begin{pmatrix} \mathbf{u_Q} & \mathbf{u_P} \end{pmatrix} \tilde{\underline{M}}^{-1} \underline{J} \underline{M}^{-1} \begin{pmatrix} \mathbf{v_Q} \\ \mathbf{v_P} \end{pmatrix} \tag{2.16}$$

A transformation $\mathbf{Z}(\mathbf{z})$ defined for $\mathbf{z}$ in a domain $\mathcal{D}$ of phase space is called canonical if at each point in that domain the J-product is preserved.

$$\langle\, \mathbf{u}|\underline{J}\,\mathbf{v}\,\rangle = \langle\, \mathbf{U}|\underline{J}\,\mathbf{V}\,\rangle$$

$$\tilde{\mathbf{u}}\underline{J}\,\mathbf{v} = \widetilde{(\underline{M}\,\mathbf{u})}\underline{J}\,(\underline{M}\,\mathbf{v})$$

$$= \tilde{\mathbf{u}}\underline{\tilde{M}}\,\underline{J}\,\underline{M}\,\mathbf{v} \therefore$$

$$\underline{J} = \underline{\tilde{M}}(\mathbf{z})\underline{J}\,\underline{M}(\mathbf{z}) \tag{2.17a}$$

For any such transformation, we also have

$$\underline{J} = \underline{\tilde{M}}^{-1}\underline{J}\,\underline{M}^{-1} \tag{2.17b}$$

$$= \underline{M}\,\underline{J}\,\underline{\tilde{M}} \tag{2.17c}$$

$$= \underline{M}^{-1}\underline{J}\underline{\tilde{M}}^{-1} \tag{2.17d}$$

Eq. 2.17c is obtained by taking the inverse of Eq. 2.17b, noting that $\underline{J}^{-1} = -\underline{J}$. According to Eq. 2.16, canonical transformations preserve the form of J-products.

2.4 Symmetries and Generating Functions

Canonical transformations have symmetries which permit the construction of some exact differentials, integration of which give "generating functions" for the canonical transformation. However, these symmetries occur only when we mix the new variables with the old ones.

Suppose a canonical transformation can be rewritten using $\boldsymbol{q}$ and $\boldsymbol{P}$ as independent variables. We partially invert the expression $\boldsymbol{P}(\boldsymbol{q},\boldsymbol{p})$ to obtain $\boldsymbol{p}$ as a function of $(\boldsymbol{q},\boldsymbol{P})$, and then substitute that result into $\mathbf{Q}(\mathbf{q},\mathfrak{p}(\boldsymbol{q},\boldsymbol{P}))$, so

$$\boldsymbol{p} = \mathfrak{p}(\boldsymbol{q},\boldsymbol{P}), \quad \mathbf{Q} = \mathcal{Q}(\mathbf{q},\mathbf{P}) \tag{2.18}$$

With these independent variables, the transformation has remarkable symmetries:

$$\frac{\partial \mathfrak{p}_i}{\partial q_j} = \frac{\partial \mathfrak{p}_j}{\partial q_i}, \quad \frac{\partial \mathcal{Q}_i}{\partial P_j} = \frac{\partial \mathcal{Q}_j}{\partial P_i}, \quad \frac{\partial \mathfrak{p}_i}{\partial P_j} = \frac{\partial \mathcal{Q}_j}{\partial q_i} \tag{2.19a}$$

From these symmetries, it follows that

$$\mathfrak{p} \cdot d\mathbf{q} + \mathcal{Q} \cdot d\mathbf{P} \tag{2.19b}$$

is a closed differential form. If these hold in a ball within $\mathbb{R}^{2N}$ spanned by coordinates $(\mathbf{q}, \mathbf{P})$, then the differential form is exact in that region, and there exists a generating function $S(\mathbf{q}, \mathbf{P})$ such that

$$\mathfrak{p}_i(\mathbf{q}, \mathbf{P}) = \frac{\partial S(\mathbf{q}, \mathbf{P})}{\partial q_i}, \quad \mathcal{Q}_i(\mathbf{q}, \mathbf{P}) = \frac{\partial S(\mathbf{q}, \mathbf{P})}{\partial P_i} \tag{2.20}$$
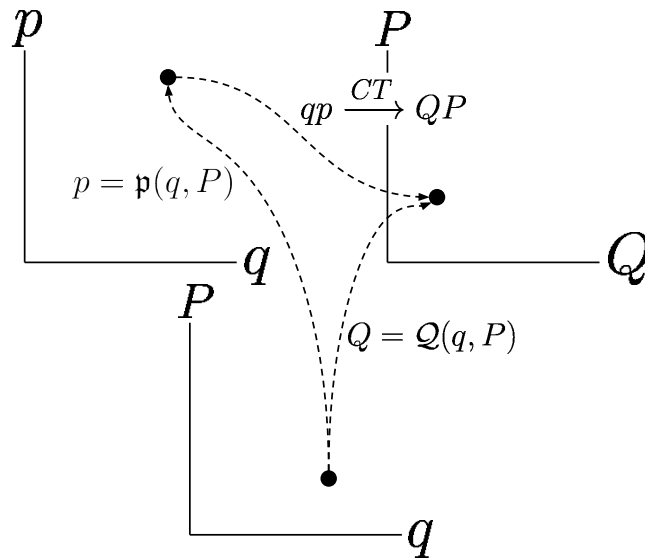
Figure 2.2: A schematic representation of the transformations in this section

$S(\boldsymbol{q}, \boldsymbol{P})$ is called [35] a "type-2" generating function of canonical transformations.

Proof of Eqs. 2.19: We partition the $2n \times 2n$ matrix $\underline{M}$ into four $n \times n$ blocks,

$$\begin{pmatrix} d\mathbf{Q} \\ d\mathbf{P} \end{pmatrix} = \underline{M} \begin{pmatrix} d\mathbf{q} \\ d\mathbf{p} \end{pmatrix} = \begin{bmatrix} \underline{A} & \underline{B} \\ \underline{C} & \underline{D} \end{bmatrix} \begin{pmatrix} d\mathbf{q} \\ d\mathbf{p} \end{pmatrix} \tag{2.21}$$

Solving for $d\mathbf{p}$ and $d\mathbf{Q}$ in terms of $d\mathbf{q}$ and $d\mathbf{P}$, we obtain

$$\begin{pmatrix} d\mathbf{p} \\ d\mathbf{Q} \end{pmatrix} = \begin{bmatrix} -\underline{D}^{-1}\underline{C} & \underline{D}^{-1} \\ \underline{A} - \underline{B}\underline{D}^{-1}\underline{C} & \underline{B}\underline{D}^{-1} \end{bmatrix} \begin{pmatrix} d\mathbf{q} \\ d\mathbf{P} \end{pmatrix} \tag{2.22}$$

The symmetries (2.19) follow if this matrix is symmetric. When we express $\underline{M}$ in terms of its submatrices $\{\underline{A} \cdots \underline{D}\}$ and substitute into Eq. 2.17a, we find

$$\tilde{\underline{B}}\underline{D} = \tilde{\underline{D}}\underline{B} \tag{2.23a}$$

from which it follows

$$\widetilde{\underline{B}\underline{D}^{-1}} = \underline{B}\underline{D}^{-1} \tag{2.23b}$$

Eq. 2.17c gives us

$$\underline{C}\tilde{\underline{D}} = \underline{D}\tilde{\underline{C}} \tag{2.23c}$$

which implies

$$\widetilde{\underline{D}^{-1}\underline{C}} = \underline{D}^{-1}\underline{C} \tag{2.23d}$$

Eq. 2.17c also produces

$$\underline{A}\tilde{\underline{D}} - \underline{B}\tilde{\underline{C}} = 1 \tag{2.23e}$$

whence (multiplying on the right by $\tilde{\underline{D}}^{-1}$)

$$\begin{aligned} \tilde{\underline{D}}^{-1} &= \underline{A} - \underline{B}\tilde{\underline{C}}\tilde{\underline{D}}^{-1} \\ &= \underline{A} - \widetilde{\underline{B}\underline{D}^{-1}\underline{C}} \\ &= \underline{A} - \underline{B}\underline{D}^{-1}\underline{C} \end{aligned} \tag{2.23f}$$

The last equation follows from Eq. 2.23d. Thus we have proved the stated symmetries. $\square$

There is another set of canonical symmetries and a corresponding generating function. Suppose instead of $(\boldsymbol{q}, \boldsymbol{P})$, the transformation can be represented using $(\boldsymbol{p}, \boldsymbol{Q})$ as independent variables. Then Eqs. 2.18-2.20 are replaced by

$$\boldsymbol{q} = \mathfrak{q}(\boldsymbol{p}, \boldsymbol{Q}), \quad \boldsymbol{P} = \mathcal{P}(\boldsymbol{p}, \boldsymbol{Q}) \tag{2.24}$$

$$\frac{\partial \mathfrak{q}_i}{\partial p_j} = \frac{\partial \mathfrak{q}_j}{\partial p_i}, \quad \frac{\partial \mathcal{P}_i}{\partial Q_j} = \frac{\partial \mathcal{P}_j}{\partial Q_i}, \quad \frac{\partial \mathfrak{q}_i}{\partial Q_j} = \frac{\partial \mathcal{P}_j}{\partial p_i} \tag{2.25a}$$

and the differential form conventionally written as

$$- \mathfrak{q} \cdot d\boldsymbol{p} - \mathcal{P} \cdot d\boldsymbol{Q} \tag{2.25b}$$

is closed. If these hold everywhere inside a ball in $\mathbb{R}^{2N}$ then there exists a generating function $\overline{S}(\boldsymbol{p}, \boldsymbol{Q})$ in that ball, with

$$\mathfrak{q}_i(\boldsymbol{p}, \boldsymbol{Q}) = -\frac{\partial \overline{S}(\boldsymbol{p}, \boldsymbol{Q})}{\partial p_i}, \quad \mathcal{P}_i(\boldsymbol{p}, \boldsymbol{Q}) = -\frac{\partial \overline{S}(\boldsymbol{p}, \boldsymbol{Q})}{\partial Q_i} \tag{2.26}$$

(The minus sign is an arbitrary convention). Two other generating functions $S_1(\mathbf{q}, \mathbf{Q})$ and $S_4(\mathbf{p}, \mathbf{P})$ can also be defined, but we will not be using them here.

2.5 Poisson Brackets

Given any two differentiable functions $F_1(\mathbf{z}), F_2(\mathbf{z})$, their Poisson Bracket is defined as the J-product of their gradients,

$$[F_1(\mathbf{z}), F_2(\mathbf{z})] = \langle \nabla_{\mathbf{z}} F_1(\mathbf{z}) | J \nabla_{\mathbf{z}} F_2(\mathbf{z}) \rangle \tag{2.27a}$$

$$= \sum_k \left(\frac{\partial F_1}{\partial q_k} \frac{\partial F_2}{\partial p_k} - \frac{\partial F_2}{\partial q_k} \frac{\partial F_1}{\partial p_k} \right) \tag{2.27b}$$

The basic Poisson brackets are

$$[q_i, q_j] = 0, \quad [p_i, p_j] = 0, \quad [q_i, p_j] = \delta_{ij} \tag{2.28}$$

From Eqs. 2.14b and 2.17a, Poisson brackets are invariant under canonical transforma-
tions. Indeed necessary and sufficient conditions for a transformation[1] $(\mathbf{q}, \mathbf{p}) \rightarrow (\mathbf{Q}, \mathbf{P})$
to be canonical is that

$$[Q_i, Q_j] = 0, \quad [P_i, P_j] = 0, \quad [Q_i, P_j] = \delta_{ij}. \tag{2.29}$$

The reader can verify this by applying Eqs. 2.27a, 2.14b, and 2.17a to each bracket in
2.29.

Functions are independent in any domain of phase space if their gradients are
linearly independent vectors. Independent functions for which the Poisson bracket
vanishes in a domain in phase space are said to "Poisson-commute." No more than N
independent functions can be mutually Poisson commuting (the maximum number of
J-orthogonal vectors is N).

It follows directly from Hamilton's Eqs. 2.7 and the definition of the Poisson
bracket that the equations of motion can be written in the form

$$\frac{dz_i}{dt} = [z_i, H(\mathbf{z})] \tag{2.30}$$

and it follows that for any function $G(\mathbf{z})$, its rate of change along the trajectory is

$$\frac{dG(\mathbf{z})}{dt} = [G(\mathbf{z}), H(\mathbf{z})] \tag{2.31}$$

Functions that Poisson commute with the Hamiltonian are thus conserved on the
trajectory.

---

[1]See appendix A.1 for proof.

2.6 Hamiltonian Flow in Phase Space

Any differentiable scalar function $F(\mathbf{z})$ generates a vector field $\mathbf{v}_F(\mathbf{z})$ and its associated flow through the definition

$$\frac{d\mathbf{z}}{dt} \equiv \mathbf{v}_F(\mathbf{z}) = \underline{J}\nabla_{\mathbf{z}}F(\mathbf{z}) \tag{2.32a}$$

$$\mathbf{z}(t;\mathbf{z}^0) = \mathbf{z}^0 + \int_0^t \mathbf{v}_F(\mathbf{z}(t'))\,dt' \tag{2.32b}$$

i.e. $\mathbf{v}_F(z)$ may be represented by the column vector $\left(\frac{\partial F}{\partial p_1}, \ldots, \frac{\partial F}{\partial p_n}, -\frac{\partial F}{\partial q_1}, \cdots, -\frac{\partial F}{\partial q_n}\right)^T$. Any such vector field is called a "Hamiltonian vector field", and the scalar function $F(\mathbf{z})$ is called "the Hamiltonian generating the field."

A theorem from Arnol'd [36] shows that two flows can be said to be "commuting" (i.e. the order of their integration does not matter) if their mutual Poisson brackets commute. Consider a rectangle $0 \leq t \leq t_0$, $0 \leq s \leq s_0$, where s and t are the limits of integration of the flows of two Poisson commuting functions, G and F respectively (See Fig. 2.3). In such a case, it can be shown that any combinations of flow integrations along a finite grid such as the one shown will correspond to the same termination point, s_0, t_0.
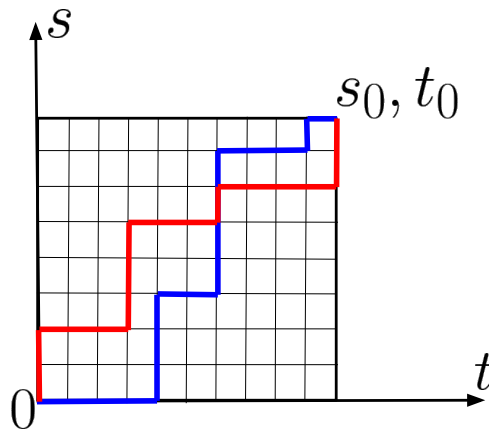
Figure 2.3: Illustration of the meaning of commuting flow.

2.7   Lagrangian Planes and Lagrangian manifolds

Any plane in a tangent space $T\Omega_{\mathbf{z_o}}$ is said to be a Langrangian plane if every pair of vectors in it are J-orthogonal to each other. For any two vectors in such a plane, the sum of oriented areas subtended by their projections into Poincaré planes adds to zero. One example of a Langrangian plane is "configuration space" (strictly speaking, we should say any plane tangent to configuration space at a point is a Lagrangian plane); any vector $\mathbf{v}$ in this plane has all momentum components vanishing, $(v_{p_i} = 0, \forall i)$, so the J-product of any pair of such vectors vanishes. Similarly, "momentum space", vectors having $(v_{q_i} = 0, \forall i)$, is Lagrangian. The 2-dimensional plane spanned by q_1 and p_2 is Lagrangian (any vector in it must have $v_{p_1} = 0$ and $v_{q_2} = 0$, so any pair of vectors spans zero area in each of the (p_1, q_1) and (p_2, q_2) planes).

A set of 2^N "Langrangian coordinate planes" is obtained by taking for each i from 1 to N either q_i or p_i; each resulting N-dimensional plane is Lagrangian. A Langrangian plane can have any dimension less than or equal to N (as that is the maximum number of linearly independent J-orthogonal vectors in a 2N-dimension phase space).

A k-dimensional manifold is a surface that is locally equivalent to $\mathbb{R}^k$, and, if it is embedded in a higher-dimensional space, that embedding is smooth. In a neighborhood of any point on the manifold, there is a differentiable and invertible mapping from k-dimensional Euclidean space $\mathbb{R}^k$ to the points on the manifold. This mapping provides smooth coordinates for the manifold. If the surface is embedded in a larger space, it must be smoothly embedded, with no creases or corners. Any manifold in phase space is called a *Lagrangian manifold* if all of its tangent planes are Lagrangian planes.

From Eqs. (2.16) and (2.17), the Lagrangian property is invariant under canonical transformations: a canonical mapping of a Lagrangian manifold is a Lagrangian manifold, and a new canonical set of coordinates applied to a given Lagrangian manifold leaves it Lagrangian.

2.8   Level Sets and Lagrangian Manifolds

Suppose we have a set of n smooth functions which are independent in some domain $\mathcal{D}$ of phase-space (their gradients $\nabla_{\mathbf{z}} F(\mathbf{z})$ are linearly independent vectors for all $\mathbf{z} \in \mathcal{D}$). A level-set of these functions is the set of points $\mathbf{z}$ such that each $F_i(\mathbf{z})$ has some specified numerical value f_i:

$$\mathbf{F}(\mathbf{z}) = \mathbf{f}, \quad \text{i.e.} \quad F_i(\mathbf{z}) = f_i \tag{2.33}$$

Since the functions are independent and smooth, each level set, labelled by the values $\mathbf{f}$, is a smooth n-dimensional manifold in the $2n$-dimensional phase space, and we will call it $\Lambda_{\mathbf{f}}$.

Suppose in addition, the mutual Poisson brackets of these functions all vanish for $\mathbf{z} \in \mathcal{D}$

$$[F_i(\mathbf{z}), F_j(\mathbf{z})] = 0 \quad \forall (i, j), \mathbf{z} \in \mathcal{D} \tag{2.34}$$

Such sets of functions are said to be "Poisson-commuting".

The resulting level sets have a remarkable geometrical property: they are Lagrangian manifolds – every plane tangent to the manifold is a Lagrangian plane. Once again, if we examine a neighborhood of any point $\mathbf{z^0}$ on the manifold, and construct two vectors $\mathbf{w}, \mathbf{x}$ both tangent to the manifold at that point, then the sum of the oriented areas subtended by the projections of those vectors into the N different Poincaré planes equals zero.

$$\langle \mathbf{w} | J\mathbf{x} \rangle = 0 \tag{2.35}$$

Proof: Consider the vector $\mathbf{v}^{(i)} = J\nabla_{\mathbf{z}} F_i(\mathbf{z})|_{\mathbf{z}^0}$ representing the Hamiltonian flow

generated by $F_i(\mathbf{z})$. In this flow all $F_j(\mathbf{z})$ are conserved ($j = 1 \cdots n$) because

$$
\begin{aligned}
\frac{dF_j(\mathbf{z})}{dt} &= \sum_k \frac{\partial F_j}{\partial q_k}\frac{dq_k}{dt} + \frac{\partial F_j}{\partial p_k}\frac{dp_k}{dt} \\
&= \sum_k \frac{\partial F_j}{\partial q_k}\frac{\partial F_i}{\partial p_k} - \frac{\partial F_j}{\partial p_k}\frac{\partial F_i}{\partial q_k} \\
&= [F_j, F_i] = 0
\end{aligned}
\tag{2.36}
$$

Therefore each $\mathbf{v}^{(i)}$ is tangent to $\Lambda_\mathbf{f}$. If we consider any pair, $(\mathbf{v}^{(i)}, \mathbf{v}^{(j)})$, tangent at a given point

$$
\begin{aligned}
\langle \mathbf{v}^{(i)}|\underline{J}\mathbf{v}^{(j)}\rangle &= \langle \underline{J}\nabla_\mathbf{z} F_i|\underline{J}\,\underline{J}\nabla_\mathbf{z} F_j\rangle \\
&= \langle \nabla_\mathbf{z} F_i|\underline{J}\nabla_\mathbf{z} F_j\rangle \\
&= [F_i, F_j] \\
&= 0
\end{aligned}
\tag{2.37}
$$

The N flow vectors $\mathbf{v}^{(i)}$ are linearly independent (the gradients $\nabla_\mathbf{z} F_i(\mathbf{z})$ are linearly independent so the flow vectors $\mathbf{v}^{(i)} = \underline{J}\nabla F_i(\mathbf{z})$ are also linearly independent), so they span the n-dimensional tangent space to the manifold at point $\mathbf{z_0}$. The J-product is bilinear in $\mathbf{w}$ and $\mathbf{x}$, so if $\mathbf{w}, \mathbf{x}$ are any linear combinations of flow vectors at a point on the manifold then Eq. 2.35 follows.

2.9 Canonical Coordinates for Families of Lagrangian Manifolds

We are getting close to the construction of action and angle variables. There are four steps: (1) Use the commuting flows on a single Lagrangian manifold to get a set of time-like coordinates $\mathbf{t} = (t_1...t_N)$ telling the location on that one Lagrangian manifold. (2) Extend the process to obtain corresponding time-like coordinates on adjacent Lagrangian manifolds. Then the values $\mathbf{f} = (f_1...f_N)$ of the commuting functions together with values of the time-like variables give a set of coordinates in a

domain phase space. Those coordinates are canonical. (3) If each Lagrangian manifold is closed, bounded and connected, then the study of the construction of $\mathbf{t}$-coordinates shows that the manifold must be a torus. (4) A canonical transformation converts coordinates $(\mathbf{f}, \mathbf{t})$ to action and angle variables $(\mathbf{I}, \boldsymbol{\theta})$.

2.9.1 t-coordinates on a single Lagrangian manifold

Consider now a single Lagrangian Manifold $\Lambda_{\mathbf{f}}$ which is a level set of n Poisson-commuting functions, $\mathbf{F}(\mathbf{z}) = \mathbf{f}, [F_i, F_j] = 0$. We wish to construct n local coordinates spanning at least a portion of this manifold. The commuting flows provide just what we need – we simply generalize the method given in section G above.

We construct N coordinates $(t_1 \ldots t_N)$ for the manifold by the following procedure.

1. Select a reference point on the manifold, $\mathbf{z_r}$

2. Integrate the flow generated by $F_1(\mathbf{z})$ to obtain a curve through $\mathbf{z_r}$:

$$\mathbf{z}(t_1, 0 \cdots 0) = \mathbf{z_r} + \int_0^{t_1} [\mathbf{z}, F_1(\mathbf{z})]_{\mathbf{z} = \mathbf{z}(t'_1, 0 \cdots 0)} dt'_1 \qquad (2.38)$$

   Since all $F_i(\mathbf{z})$ are conserved under this flow, that curve stays on $\Lambda_{\mathbf{f}}$.

3. Then for each value t_1 in some domain, integrate the flow generated by $F_2(\mathbf{z})$ to generate a two-dimensional surface also lying on $\Lambda_{\mathbf{f}}$

$$\mathbf{z}(t_1, t_2, 0 \ldots 0) \quad = \quad \mathbf{z}(t_1, 0 \cdots 0) \quad + \quad \int_0^{t_2} [\mathbf{z}, F_2(z)]_{\mathbf{z} = \mathbf{z}(t_1, t'_2, 0 \cdots 0)} dt'_2 \quad (2.39)$$

4. From each point on the two-dimensional surface, integrate the flow generated by $F_3(\mathbf{z})$ to sweep out a three-dimensional region.

5. Continue in this way until we have generated an n-dimensional domain of $\Lambda_{\mathbf{f}}$. If $\Lambda_{\mathbf{f}}$ is multiply-connected, (for example if $\Lambda_{\mathbf{f}}$ is a torus), then for now let us restrict

the maximum values of the t_i so that integration stays in a simply-connected domain.

Now $\mathbf{t} = (t_1 \ldots t_N)$ provides N coordinates uniquely specifying each point in this simply-connected domain of $\Lambda_{\mathbf{f}}$. The coordinates are smooth and leave no holes (points in the domain not covered by the coordinates) because $\mathbf{z}(\mathbf{t})$ is a continuous function of each t_i provided that $F_i(\mathbf{z})$ is a continuous function of $\mathbf{z}$. Thus we have obtained good coordinates for a single Lagrangian manifold.

2.9.2 $(\mathbf{t}, \mathbf{f})$-coordinates on a family of Lagrangian manifolds

We need to generalize this construction to obtain coordinates for a family of Lagrangian manifolds $\Lambda_{\mathbf{f}}$, where the values f_i each vary over some domain. The space spanned by values of $f_1 \cdots f_n$ is called "spectrum space" (or in some cases "energy-momentum space").

A level set of Poisson-commuting functions is said to be "regular" if at every point $\mathbf{z_0}$ on that level set, the gradients of the functions are linearly independent (otherwise it is singular). A point $\mathbf{f_0}$ in spectrum space is said to be regular if the corresponding level set is regular.

A domain $\mathcal{F}$ in spectrum space is said to be regular if it consists only of regular points.

Consider a simply-connected regular domain of spectrum space. For each point $\mathbf{f}$ in that domain, there is a Lagrangian manifold, $\Lambda_{\mathbf{f}}$, and this collection of Langrangian manifolds foliates a region of phase space. We consider a point $\mathbf{z}^0$ in this region, and a sufficiently small neighborhood of this point. In this neighborhood, we wish to construct a canonical set of variables $\{t_1(z), \ldots, t_N(z), F_1(z), \ldots, F_N(z)\}$ such that the Poisson-commuting functions themselves constitute the canonical momenta. (Note that we are being careful to do this construction in a sufficiently small domain; the coordinates $\mathbf{t}$ cannot extend continuously over the whole of even a single torus, and the problems of monodromy arise when we try to extend this construction too far in spectrum space.)

We begin from any N-dimensional Lagrangian manifold Φ_0 passing through the point $\mathbf{z}^0$ transversely to the level sets $\{\mathbf{z}|\mathbf{F}(\mathbf{z}) = \mathbf{f}\}$. Then the values $\mathbf{f}$ provide suitable coordinates for that surface. Since the surface is Lagrangian, the vectors tangent to the surface

$$\phi_i = \frac{\partial \mathbf{z}}{\partial f_i} \quad F_j(\mathbf{z}) \text{ fixed } j \neq i \tag{2.40a}$$

are all mutually J-orthogonal,

$$\langle \phi_\mathbf{i}|\underline{J}\phi_\mathbf{j}\rangle = 0 \tag{2.40b}$$

Each point on this initial manifold Φ_0 is considered to be a reference point $\mathbf{z_r}(\mathbf{f})$, which we use as a starting point on $\Lambda_\mathbf{f}$ for constructing coordinates $\mathbf{t}(\mathbf{z})$ on $\Lambda_\mathbf{f}$. Then $(\mathbf{t}, \mathbf{f})$ provide coordinates for a $2n$-dimensional neighborhood of the original point $\mathbf{z_0}$.

Theorem: The $(\mathbf{t}, \mathbf{f})$ cooridnates are a canonical set of coordinates.

We prove this by showing that the J products of tangent vectors, and equivalent Poisson brackets, satisfy Eq. 2.29. Choose a point on the manifold, and let $\boldsymbol{\tau}_j = (\partial \mathbf{z}/\partial t_j)_{t_k,\mathbf{f}}$. This vector is tangent to the manifold $\Lambda_\mathbf{f}$, and it points in a direction such that $t_k, k \neq j$ are fixed, but t_j is increasing.

$$\langle \boldsymbol{\tau}_j|\underline{J}\boldsymbol{\tau}_i\rangle = 0 \tag{2.41a}$$

Eq. 2.41a holds because $\Lambda_\mathbf{f}$ is Lagrangian and $\boldsymbol{\tau}_i, \boldsymbol{\tau}_j$ are tangent to it at a point.

Now consider the n-dimensional surface having $\mathbf{t}$ fixed and the values $\mathbf{f}$ varying. Vectors tangent to that surface are

$$\phi_i = \frac{\partial \mathbf{z}}{\partial f_i} \quad \mathbf{t} \text{ fixed}, f_j \text{ fixed } j \neq i \tag{2.41b}$$

That surface is Lagrangian because the initial surface was Lagrangian, and Hamiltonian flow preserves the Lagrangian property. Therefore

$$\langle \boldsymbol{\phi}_i|\underline{J}\boldsymbol{\phi}_j\rangle = 0 \tag{2.41c}$$

And now the cross terms,

$$\langle \boldsymbol{\tau}_j | \underline{J}\boldsymbol{\phi}_k \rangle$$

$$= \sum_i \frac{\partial q_i}{\partial t_j}\frac{\partial p_i}{\partial f_k} - \frac{\partial p_i}{\partial t_j}\frac{\partial q_i}{\partial f_k}$$

$$= \sum_i \frac{\partial F_j}{\partial p_i}\frac{\partial p_i}{\partial f_k} + \frac{\partial F_j}{\partial q_i}\frac{\partial q_i}{\partial f_k}$$

$$= \frac{\partial F_j(\mathbf{q}(\mathbf{t},\mathbf{f}),\mathbf{p}(\mathbf{t},\mathbf{f}))}{\partial f_k} \quad \mathbf{t}, f_\ell \text{ fixed }, \ell \neq k$$

$$= \delta_{jk} \tag{2.41d}$$

where in the second equality we have substituted Hamilton's equations. This completes the proof that $\mathbf{t}, \mathbf{f}$ comprises a set of $2n$ canonical coordinates. Thus there exists a canonical transformation from the original set $(\mathbf{q}, \mathbf{p})$ to the new set, $(\mathbf{t}, \mathbf{f})$.

Now let us look in a region of partial invertibility in the manner of Eqs 2.18, so each t_i can be regarded as a function of $\mathbf{q}$ and $\mathbf{f}$. Then the canonical symmetry property 2.19 implies

$$\frac{\partial t_i(\mathbf{q}, \mathbf{f})}{\partial f_j} = \frac{\partial t_j(\mathbf{q}, \mathbf{f})}{\partial f_i} \tag{2.42}$$

This equation will be important to us later (2.9.3). It means that for each fixed $\mathbf{q}$, there is a differential form

$$\omega_{\mathbf{q}} = \sum_k t_k(\mathbf{q}, \mathbf{f}) df_k$$

which is closed. It might also be exact, depending on the topology of the space in which it is well-defined (Hamiltonian monodromy arises when it is not exact.).

2.9.3   Tori and Action-Angle Variables

Construction of Angle Variables

Suppose over a regular domain $\mathcal{F}$ in spectrum space, each Lagrangian manifold $\Lambda_{\mathbf{f}}$ is compact and connected. Because the domain is regular, each manifold admits n independent commuting flows, with continuous velocity fields $\mathbf{v}_{F_i}$ (Eqs 2.32) that

never vanish. A theorem in topology asserts that the only structure which admits n everywhere-independent continuous non-vanishing flows is an N-dimensional torus. (It is not hard to show that an N-torus can admit N independent non-vanishing flows [37]. More difficult is the proof that an N-torus is the only structure that can do so. A kind of proof is given by Arnol'd [38].) We show below that the work of constructing coordinates for the Lagrangian manifolds leads to a convincing argument that the manifolds must all be tori.

A torus is, of course, multiply connected. This means that our coordinates $\mathbf{t}$ are good only for portions of the torus sufficiently close to the reference point. We need another set of coordinates for global use on a single torus. Our discussion below spells out the theory for $N = 2$; The generalization to larger N is straightforward.

Let's first think about directed curves on a torus. In Fig. 2.4, we show three closed directed curves on a 2-torus. One is called "trivial" because it can be shrunk to a point; such curves are henceforth ignored. Each of the other two traces out a fundamental loop on the torus. A cycle is defined as a family of homotopically equivalent, continuous, closed, directed curves. "Homotopically equivalent" means that any member of the family can be smoothly distorted to any other without breaking the curve or leaving the torus [37].

An N-torus has N nontrivial independent fundamental cycles $\{\mathcal{C}_i, i = 1 \cdots n\}$. Other cycles can be constructed as integer combinations of the fundamental cycles (e.g. $5\mathcal{C}_1 - 3\mathcal{C}_2$ means follow $\mathcal{C}_1$ five times, then follow $\mathcal{C}_2$ backwards three times). Families of curves in each cycle can be chosen such that they form good coordinates for a torus (because the flows commute).

Let us choose one Lagrangian Manifold Λ_{f_o} with its two continuous non-vanishing vector fields. Assume that the points on this manifold constitute a connected, closed and bounded set in phase space. The following argument indicates that Λ_{f_o} must be a torus, and it shows how to find its fundamental cycles.

Let us choose one arbitrary initial point $\mathbf{z}^0$ on this Λ_{f_o}. Then, for all (t_1, t_2) with $-\infty < t_i < \infty$, i.e. all $\mathbf{t} \in \Re^2$, the set of points $\{\mathbf{z}(\mathbf{t}; \mathbf{z}^0) = U(\mathbf{t})\mathbf{z}^0\}$ also lies on Λ_{f_o}.
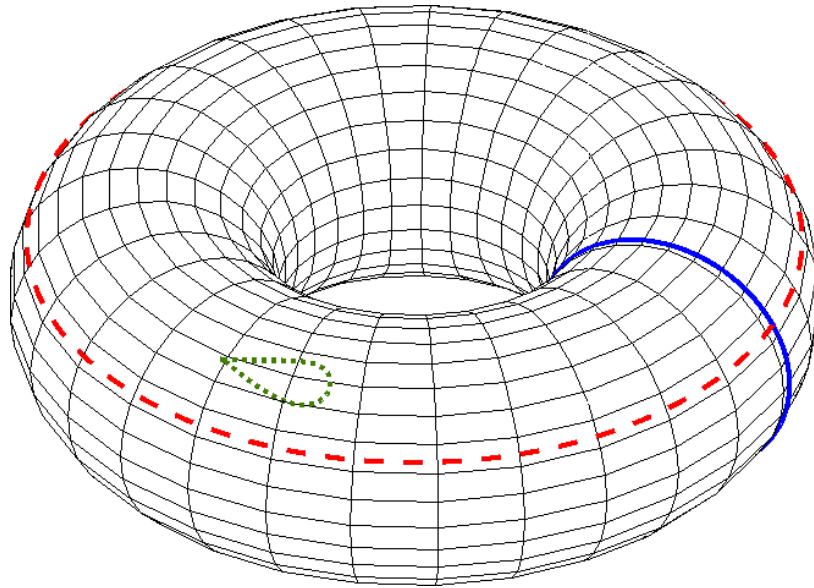
Figure 2.4: This 2-torus has two fundamental loops.

But the Euclidean plane $\Re^2$ is an infinite open set, whereas we assumed that Λ_{f_o} is closed and bounded. Therefore, the mapping from $\mathbf{t}$ to $\mathbf{z}$ on Λ_{f_o} must be many-to-one. Hence there must be many points $\hat{\mathbf{t}}$ such that

$$U(\hat{\mathbf{t}})\mathbf{z}^0 = \mathbf{z}^0 \tag{2.43}$$

Here, we have defined a useful object called a "classical evolution operator", $U(t_1, t_1)$, a nonlinear, non-unitary operator acting on points in phase space $\mathbf{z}^0$ such that

$$U(t_1, t_2)\mathbf{z}^0 = \mathbf{z}(t_1, t_2; \mathbf{z}^0) \tag{2.44}$$

We need to select one of these points $\hat{\mathbf{t}}$ having short but nonzero Euclidean length $\sqrt{t_1^2 + t_2^2}$), and call it $\mathbf{T}^a = (t_1^a, t_2^a)$. To start, let's choose the one with the shortest length (if more than one have equal shortest length, choose any of those). Now let's draw a straight line segment in $\mathbf{t}$-space connecting the origin with that $\mathbf{T}^a$. Let us call the resulting line segment L^a, and consider the corresponding set of points on Λ_{f_o} in phase space, $\mathbf{C}^a = \mathbf{z}(L^a) = \{\mathbf{z}(\mathbf{t}; \mathbf{z_0}))|\mathbf{t} \in L^a\}$. That set of points begins and ends at

$\mathbf{z}^0$, but the line L^a cannot be shrunk to zero. Therefore this set of points $\mathbf{C}^a$ must go around a loop on Λ_{f_o}. If L^a is extended to $K\mathbf{T}^a$, where K is any positive or negative integer, then that same loop $\mathbf{C}^a$ is traced out repeatedly, since

$$U(\mathbf{t} + \mathbf{T}^a)\mathbf{z}^0 = U(\mathbf{t})U(\mathbf{T}^a)\mathbf{z}^0 = U(\mathbf{t})\mathbf{z}^0 \tag{2.45}$$

Now if we start again at the origin ($\mathbf{t} = \mathbf{0}, \mathbf{z} = \mathbf{z}^0$), and consider lines in $\mathbf{t}$-space transverse to L^a, those lines span the rest of the plane, which is again an open unbounded set. So it must have a many-to-one mapping to our closed and bounded Λ_{f_o}. Therefore there must exist some other points $\hat{\mathbf{t}}$ satisfying Eq. 2.43. Again, we may select one of the shortest of nonzero length, call it $\mathbf{T}^b$, and consider the straight line segment L^b in $\mathbf{t}$-space from the origin to $\mathbf{T}^b$. The corresponding set of phase space points $\mathbf{C}^b = \mathbf{z}(L^b) = \{\mathbf{z}(\mathbf{t}; \mathbf{z_0}))|\mathbf{t} \in L^b\}$ must trace out another loop on Λ_{f_o} different from $\mathbf{C}^a$.

The set of points $\{m\mathbf{T}^a + n\mathbf{T}^b|m, n \in integers\}$ form a lattice in $\mathbf{t}$-space called the period lattice, and the quadrilateral subtended by L^a and L^b can be regarded as a unit cell of $\mathbf{t}$-space. For any point $\mathbf{t}'$ in that cell, there is a corresponding point $\mathbf{z}' = U(\mathbf{t}')\mathbf{z}^0$ on Λ_{f_o}, and

$$U(m\mathbf{T}^a + n\mathbf{T}^b)\mathbf{z}' = \mathbf{z}' \tag{2.46}$$

because the flows commute. By this argument, we have shown that this Lagrangian manifold Λ_{f_o} has the topological structure of a torus, and further, we have shown that the period lattice is independent of the initial point $\mathbf{z}^0$ on the torus. This argument also applies to any connected, closed and bounded Lagrangian Manifold with independent non-vanishing flows.

If we move continuously in spectrum space from one torus to another, changing the initial point $\mathbf{z}^0(\mathbf{f})$ smoothly, any point on the period lattice $\hat{\mathbf{t}}(\mathbf{f})$ changes continuously and differentiably. This means that as we move from one torus to another, it is possible to choose $(\mathbf{T}^a(\mathbf{f}), \mathbf{T}^b(\mathbf{f}))$ such that they are differentiable functions of $\mathbf{f}$. (Above we said
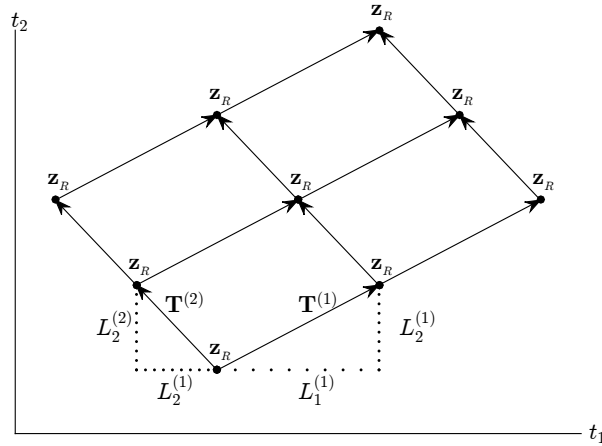
Figure 2.5: The fundamental cycles on a torus form a period lattice. Each lattice vertex corresponds to returning to the same location on the torus. The vectors $\mathbf{T}^{(j)}$ correspond to the jth fundamental cycles on the torus.

that we start on one torus Λ_{f_o} by choosing $\mathbf{T}^a$ and $\mathbf{T}^b$ to be the $\hat{\mathbf{t}}$'s of shortest length. However, as the $\hat{\mathbf{t}}$'s vary with $\mathbf{f}$, we require that $\mathbf{T}^a$ and $\mathbf{T}^b$ change differentiably.) Furthermore, since $(\mathbf{t}, \mathbf{f})$ are canonical variables, each of the period vectors $\mathbf{t}^\alpha(\mathbf{f})$, $\alpha = a, b$ obey the canonical symmetry.

$$\frac{\partial T_i^{(\alpha)}}{\partial f_k} = \frac{\partial T_k^{(\alpha)}}{\partial f_i} \tag{2.47}$$

Proof: Assume that there exists at least one point on the torus Λ_f which is surrounded by a neighborhood having good projection into configuration space, i.e. a neighborhood such that the relationship $\mathbf{q}(\mathbf{t}; \mathbf{f})$ between time and positions on the torus is differentiable and invertible. Then the transverse "starter manifold" may be taken to be $\mathbf{q} = $ constant, and we can use the $(\mathbf{q}, \mathbf{f})$ as coordinates for nearby points in phase space. There, the time coordinates on the nearby tori are functions $\mathbf{t}(\mathbf{q}, \mathbf{f})$. This is partial invertibility discussed around Eq. 2.41c, and 2.47 is a special case of Eq. 2.42.

Construction of Angle and Action Variables

We have already said, and it is apparent from Fig. 2.5 that the time coordinates generally cannot be used over the whole of even one torus. We transform time variables

to angle variables $\boldsymbol{\theta} = \{\theta_\alpha, \alpha = 1, 2...N\}$ on each torus using the elements of the period vectors $T_i^{(\alpha)}(\mathbf{f})$. On each torus Λ_f, we define the angles such that

$$t_j = \sum_\alpha \frac{T_j^\alpha(\mathbf{f})\theta_\alpha}{2\pi}$$

$$\boldsymbol{\theta} = 2\pi [\underline{T}(\mathbf{f})]^{-1}\mathbf{t}$$

(2.48)

Then, on traversing each fundamental cycle $\mathbf{C}^\alpha$ on the torus, the angle θ_α increases by 2π (The matrix representing the period lattice is invertible because $\mathbf{T}$ vectors are independent).

Let us now seek a collection of new momenta $\mathbf{I} = \{I_j, j = 1 \cdots n\}$ such that the transformation $(\mathbf{t}, \mathbf{f}) \leftrightarrow (\boldsymbol{\theta}, \mathbf{I})$ is canonical (these are the action angle variables). For this purpose, we consider the transformation[2] $(\boldsymbol{q}, \mathbf{p}) \leftrightarrow (\boldsymbol{\theta}, \mathbf{I})$. The canonical symmetries are expressed by thinking of $(\mathbf{q}, \mathbf{I})$ as independent variables with the others expressed as $\boldsymbol{p}(\mathbf{q}, \mathbf{I})$, $\boldsymbol{\theta}(\mathbf{q}, \mathbf{I})$,

$$\frac{\partial p_i}{\partial q_j} = \frac{\partial p_j}{\partial q_i}, \quad \frac{\partial \theta_i}{\partial I_j} = \frac{\partial \theta_j}{\partial I_i}, \quad \frac{\partial p_i}{\partial I_j} = \frac{\partial \theta_j}{\partial q_i}$$

(2.49a)

and the differential form

$$\sum_i p_i dq_i + \theta_i dI_i$$

(2.49b)

is closed. If everything we have said this section is valid in a simply-connected domain $\mathcal{F}$ of spectrum space, then we can construct a generating function, $S(\mathbf{q}, \mathbf{I})$, single-valued in $\mathbf{I}$ though multivalued in $\mathbf{q}$, such that

$$dS = \sum_i p_i dq_i + \theta_i dI_i$$

(2.49c)

$$p_k = \frac{\partial S}{\partial q_k} \quad \theta_k = \frac{\partial S}{\partial I_k}$$

(2.49d)

---

[2] This presumes that each torus has a good projection into $\mathbf{q}$ space. Such a thing cannot exists for the entire torus, and to do everything properly, we have to consider projection into other Lagrangian coordinate planes. However, it suffices if a neighborhood of the reference point on each torus has a good projection into $\mathbf{q}$-space.

Holding $\mathbf{I}$ fixed, let us integrate this differential form around the kth fundamental loop on the torus. For this purpose, let us use $(\boldsymbol{\theta}, \mathbf{f})$ as independent variables and integrate

$$\Delta S^{(k)} = \oint_0^{2\pi} \sum_i p_i(\mathbf{q}(\boldsymbol{\theta}, \mathbf{f})) \left(\frac{\partial q_i}{\partial \theta_k}\right) d\theta_k \qquad (2.50)$$

The superscript (k) means that this is the change of the generating function on one circuit of the kth fundamental loop, when θ_k goes from 0 to 2π with all other θ's fixed. At the end of that loop,

$$\theta_k = \theta_k(\mathbf{T}^{(k)}, \mathbf{f}) = 2\pi = \frac{\partial \Delta S^{(k)}}{\partial I_k} \qquad (2.51)$$

and therefore

$$I_k(\mathbf{f}) = \frac{1}{2\pi} \Delta S^{(k)}(\mathbf{f}) \qquad (2.52a)$$

$$= \frac{1}{2\pi} \oint_{\mathcal{C}_k} \boldsymbol{\mathcal{P}}(\mathbf{q}, \mathbf{f}) \cdot d\mathbf{q} \qquad (2.52b)$$

This integral around the kth fundamental loop on the torus gives the value of the kth action variable as a function of the values of the conserved quantities $\mathbf{f}$. Thus we have obtained canonical action-angle variables $(\boldsymbol{\theta}, \mathbf{I})$ for describing the tori.

2.10 Fibrations of the Level Sets F

Now that we have a thorough understanding of how we come to have objects like Lagrangian manifolds and action-angle variables, it must be emphasized that all of this methodology holds true provided that all of the assumptions hold everywhere in a $2N$-dimensional ball in phase space, and therefore in a corresponding N-dimensional ball in spectrum space. If there are points, lines or regions in which any of the assumptions fail, then we have a problem. In particular, consider a two dimensional cylindrically-symmetric system such as is defined in the following Chapter, Sec. 3.1. In this case: (1) the differential form 2.49c is closed but not exact, so the action variables

are multivalued functions of the conserved quantities. (2) Furthermore, the "time-like" variable related to angular momentum actually corresponds to an angle, and angles are notoriously multivalued: $T_i^\alpha(\mathbf{f})$ is a multivalued function of $\mathbf{f}$. The fundamental cycles themselves are "multivalued": i.e. *the map from conserved quantities* $\mathbf{f}$ *specifying a torus to the fundamental cycles on that torus is one-to-many.* This is the problem that leads to nontrivial monodromy of the action and angle variables.

In order to understand and categorize these cases we should aim to understand the Lagrangian torus fibration of the phase space of our system. Let $\mathbf{f}$ be an element of the image of $\mathbf{F}$ and consider the fiber $\mathbf{F}^{-1}(\mathbf{f})$. By the Liouville-Arnol'd theorem, if $\mathbf{f}$ is a regular value, $\mathbf{F}^{-1}(\mathbf{f})$ is a smooth torus $\mathbf{T}^2$ or a union of such tori. As mentioned in the introduction, this type of information is encoded in the space of level sets, and our goal is understanding how each of the regular and critical fibers $\mathbf{F}^{-1}(\mathbf{f})$ affect the global topology of the action-angle variables. In the following section, we will be looking at the basic topological obstruction to the existence of global actions, a system with one singular value $\mathbf{f}$ whose fiber is a pinched torus.

Chapter 3

Static Monodromy: Mexican

Hat System

Now that we have introduced the general framework of action-angle variables and their relations to geometric concepts in phase space, we will introduce "Hamiltonian monodromy." This chapter focuses on monodromy of the action-angle variables themselves, which manifests itself in topological changes of the angle loops on tori. This chapter deals primarily with the first of our two systems, the Mexican-hat system, which is in many ways the archetypal system with monodromy. We show that one of the actions of this system, and its associated angle variable, are multi-valued functions of the conserved quantities, energy and angular momentum. The theory of static monodromy of this system has been well established before my PhD work [1], but the concepts are important for the work in the following chapters.

3.1   Mexican Hat System

Take a system with two degrees of freedom (x, y) in a cylindrically symmetric well $V(\rho)$. A particle in this system can either oscillate radially, along $\rho = \sqrt{x^2 + y^2}$, rotate around the origin azimuthally, or some combination of the two. The specific model

considered is often called a "Mexican-hat" or "Champagne-bottle" system:

$$V(\rho) = -a\rho^2 + b\rho^4 \quad (a, b > 0) \tag{3.1}$$

$$H(\mathbf{q}, \mathbf{p}) = \tfrac{1}{2}\mathbf{p}^2 + V(\rho) = h \tag{3.2}$$

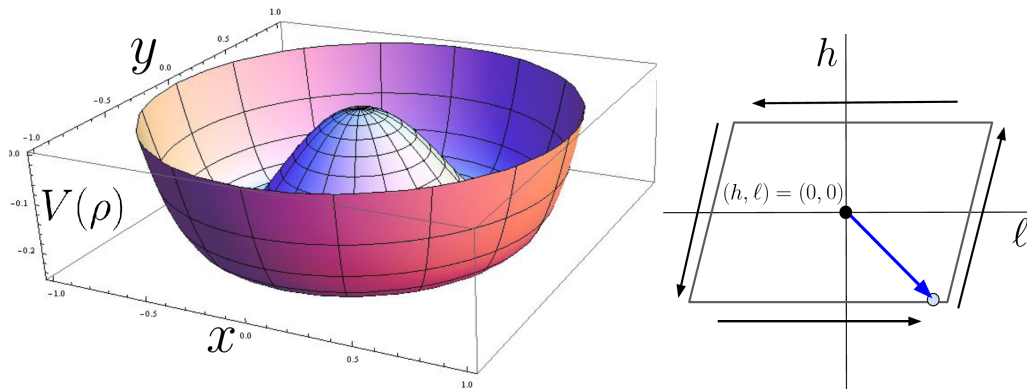$$L(\mathbf{q}, \mathbf{p}) = xp_y - yp_x = \ell \tag{3.3}$$

Figure 3.1: (Left)A Mexican Hat potential. (Right) An example monodromy circuit. There is only one singular value in (ℓ, h)-space, at the monodromy point at $(\ell = 0, h = 0)$.

The Hamiltonian and angular momentum are conserved quantities, so we can take $\{L(\mathbf{z}), H(\mathbf{z})\}$ as the flow generators for this system. That is to say, either can be used to obtain Hamiltonian differential equations, the solution to which is a flow in phase space. These functions satisfy all of the conditions to be flow generators except at the singular point $\mathbf{z}_0 = (x, y, p_x, p_y) = (0, 0, 0, 0)$.

$$\nabla_{\mathbf{z}} L = (p_y, -p_x, -y, x)^T \tag{3.4}$$

$$\nabla_{\mathbf{z}} H = \left(\frac{\partial V(\rho)}{\partial x}, \frac{\partial V(\rho)}{\partial y}, \frac{p_x}{m}, \frac{p_y}{m} \right)^T \tag{3.5}$$

The derivatives of $H(\mathbf{z})$ and $L(\mathbf{z})$ vanish at $\mathbf{z}_0$ and the two gradients are no longer linearly independent. The corresponding point in spectrum space, $(\ell, h) = (0, 0)$, is a singular value, often called a "monodromy point."

Next, we examine level sets $\Lambda_{(\ell,h)}$ of these functions: the set of phase space points $\mathbf{z}$ such that all flow generators are constants is given by

$$\Lambda_{(\ell,h)} = \{\mathbf{z} \mid L(\mathbf{z}) = \ell,\ H(\mathbf{z}) = h\} \tag{3.6}$$

The "Liouville-Arnol'd" theorem asserts that any such level set that is compact and connected is topologically equivalent to a torus [38]. Futhermore there exists a set of canonical action-angle variables that make good coordinates on the $\Lambda_{(\ell,h)}$ tori. However, the fiber $\Lambda_{\mathbf{f}_o} = \mathbf{F}^{-1}(\mathbf{f}_o)$, where $\mathbf{f}_o = (\ell = 0, h = 0)$, corresponds to a pinched torus. This will prevent the existence of globally defined action and angle variables. For tori corresponding to this system, see Figs. 3.3 and 5.10.

When a phase space point $\mathbf{z}$ traces out fundamental loops on the torus, the angle variable $\phi_\alpha(\mathbf{z})$ varies from 0 to 2π, while the action variables $I_\alpha(\mathbf{z})$ are constant on the torus $\Lambda_{(\ell,h)}$. The $I_\alpha(\mathbf{z})$ are constant because they are functions of the flow generators, $I_\alpha(\mathbf{z}) = \mathcal{I}_\alpha(L(\mathbf{z}),\ H(\mathbf{z}))$, and a torus is defined by the level sets of constant values (ℓ, h). This also means that we can identify a torus by either the level set $\Lambda_{(\ell,h)}$ or the action variables $\mathcal{I}_\alpha(\ell,\ h)$.

A monodromy circuit is a closed directed path $[l(s), h(s)]$ in spectrum space that surrounds the singular value (s is continuous timelike variable that parameterizes the monodromy circuit). One of the action variables is

$$\mathcal{I}_2(\ell, h) = \frac{1}{2\pi} \oint L(\mathbf{z}) d\phi = \ell. \tag{3.7}$$

Letting superscripts i and f represent initial and final states on the monodromy circuit, the first action variable after completing the circuit is unchanged,

$$\mathcal{I}_2^i(\ell, h) = \ell^i, \quad \mathcal{I}_2^f(\ell, h) = \ell^f \tag{3.8}$$

because ℓ^i and ℓ^f are the same.

Now we attempt to calculate a radial action integral by fixing ϕ and using

$$
\begin{aligned}
\mathcal{I}_1(\ell, h) &= \frac{1}{2\pi} \oint \mathcal{P}_\rho(p; \ell, h) d\rho \\
&= \frac{1}{2\pi} \oint \sqrt{2m \left(h - V(\rho) - \frac{\ell^2}{2m\rho^2} \right)} d\rho
\end{aligned}
\tag{3.9}
$$

However, the above form is manifestly symmetric in ℓ, and when we examine $\partial \mathcal{I}_1/\partial \ell$ for $h > 0$ and $\ell \to 0^+$, we find that it does not vanish:

$$
\frac{\partial \mathcal{I}_1}{\partial \ell} = \frac{-1}{2\pi} \oint \frac{(\ell/\rho^2)}{\sqrt{2m \left(h - V(\rho) - \frac{\ell^2}{2m\rho^2} \right)}} d\rho
\tag{3.10}
$$

From Hamilton's equations,

$$
\frac{d\phi}{dt} = \frac{\ell}{m\rho^2}
\tag{3.11a}
$$

$$
\frac{d\rho}{dt} = \frac{p_\rho}{m} = \frac{1}{m} \left[2m \left(h - V(\rho) - \frac{\ell^2}{2m\rho^2} \right) \right]^{1/2}
\tag{3.11b}
$$

so

$$
\frac{\partial \mathcal{I}_1}{\partial \ell} = \frac{-1}{2\pi} \oint \frac{d\phi/dt}{d\rho/dt} d\rho
\tag{3.12a}
$$

$$
= \frac{-1}{2\pi} \int \frac{d\phi}{d\rho} d\rho
\tag{3.12b}
$$

$$
= \frac{-1}{2\pi} \Delta(\ell, h)
\tag{3.12c}
$$

where $\Delta(\ell, h)$ is the geometrical angle subtended in one radial oscillation from outer turning point to outer turning point. For $h > 0$ and $\ell \to 0^+$

$$
\Delta(\ell \to 0, h > 0) \to \pi
\tag{3.13}
$$

Hence we see that for *any* cylindrically symmetric system, Eq. 3.9 leads to an action variable that has a discontinuous derivative at $\ell = 0, h > 0$, where zero energy is defined by the top of the barrier at $\rho = 0$ (Worse, the angle variables are discontinuous

functions at $\ell = 0, h > 0$, see appendix A.2).

Now let's construct the fundamental cycles. We define the time of first return in the radial coordinate as

$$T_1^{(1)} = \oint dt_1 \tag{3.14a}$$

$$= \oint \frac{dt_1}{d\rho} d\rho = \oint \frac{1}{\frac{d\rho}{dt_1}} d\rho \tag{3.14b}$$

$$= \oint \frac{m}{\mathcal{P}_\rho(\rho; \ell, h)} d\rho \tag{3.14c}$$

$$= 2 \int_{\rho_{\min}}^{\rho_{\max}} \frac{m}{\left[2m \left(h - V(\rho) - \frac{\ell^2}{2m\rho^2} \right) \right]^{1/2}} d\rho \tag{3.14d}$$

and the azimuthal angle subtended in a cycle of ρ motion as

$$\Delta_1(\ell, h) = \oint d\varphi \tag{3.15a}$$

$$= -2\pi \frac{\partial \mathcal{I}}{\partial \ell} \tag{3.15b}$$

$$= 2 \int_{\rho_{\min}}^{\rho_{\max}} \frac{\ell/\rho^2}{\left[2m \left(h - V(\rho) - \frac{\ell^2}{2m\rho^2} \right) \right]^{1/2}} d\rho \tag{3.15c}$$

Here we have gone backwards from the RHS of Eq. 3.12b to the RHS of Eq. 3.10. Eq. 3.15c might look trivial, but it needs careful examination. It is manifestly an antisymmetric function of ℓ. If $h > 0$, we can see geometrically that $\Delta_1(\ell, h)$ passes smoothly through zero when ℓ passes through zero. However, when $h > 0$, $\Delta_1(\ell, h)$ approaches π when ℓ approaches zero, and then jumps discontinuously to $-\pi$. Therefore it cannot be the derivative of a smooth action variable.

We can get a smooth function, but only at a price: the function must be multivalued. We may define a function Δ_2 on a multi-sheeted surface over the (ℓ, h) plane,
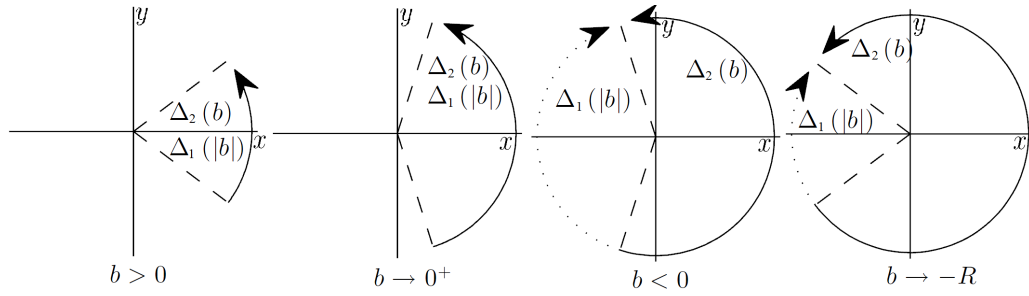
$$\Delta_2 = \Delta_1(\ell, h) + 2n\pi \tag{3.16}$$

Figure 3.2: As b (the x component of $\mathbf{z}^0$) changes from $R \to -R$, Δ_1 is discontinuous where Δ_2 smoothly changes from $0 \to 2\pi$, as described by Eq. 3.16. Δ_1 and Δ_2 are identical in the two left-hand figures, but $\Delta_1 = 2\pi - \Delta_2$ in the two right hand figures.

Starting with $\ell = 0$ and $h < 0$, we choose $n = 0$; then we may follow any path in the (ℓ, h) plane avoiding the origin; add 1 to n for every counterclockwise passage through the half-line $\ell = 0, h > 0$, and subtract 1 from n for every clockwise passage through that line.

This formula for Δ_2 corresponds to a rule for closing the cycles, see Fig. 3.2. For $h < 0$, $\ell > 0$, we construct a cycle by integrating the trajectory under H, starting an ending at $\rho_{\max}$, and then returning to the initial point by going counterclockwise at $\rho = \rho_{\max}$. For $\ell < 0$, we continue to run counterclockwise at $\rho_{\max}$. This makes Δ_2 continuous through $\ell = 0$ if $h < 0$. Now if we traverse a monodromy circuit (a counterclockwise path around the origin in the (ℓ, h) plane), we want the return path to change in a continuous fashion. Thus if we start and end the circuit at $\ell = 0, h < 0$, Δ_2 increases from 0 to 2π. (If we go around the circuit again, there is another increase by 2π.) Smooth closure of the cycles gives Eq. 3.16.

In this way, smooth closure of the cycles is consistent with Eq. 3.16, and it also produces a smooth action variable $\mathcal{I}_1$.

$$\mathcal{I}_1 = \oint_{\mathcal{C}_1} \mathbf{p} \cdot d\mathbf{q} \tag{3.17}$$

However, the cycles are "multivalued": after a journey around a monodromy circuit,

$$\mathcal{C}_1 \to \mathcal{C}_1 - \mathcal{C}_2 \tag{3.18}$$

and so the action variable is also a multivalued function of (ℓ, h)

$$\mathcal{I}_1 \rightarrow \mathcal{I}_1 - \mathcal{I}_2 \tag{3.19}$$

After completing the monodromy circuit the action variables have changed to

$$\mathcal{I}_1'(\ell, h) = \mathcal{I}_1(\ell, h) - \mathcal{I}_2(\ell, h),$$
$$\mathcal{I}_2'(\ell, h) = \mathcal{I}_2(\ell, h) \tag{3.20}$$

Therefore $\mathcal{I}_1$ must be a multivalued function. The conjugate angle variables also change after going through the monodromy circuit,

$$\phi_1' = \phi_1,$$
$$\phi_2' = \phi_2 + \phi_1. \tag{3.21}$$

The new angle variables defined in Eq. 3.21 are canonically conjugate to the new actions defined in Eq. 3.20, see appendix A.3 for proof. When the system is carried through the monodromy circuit, the initial and final torus are the same, $\Lambda_{(\ell,h)}$, and the action and angle variables are now continuous, but it is at the price of being multivalued. Reference [29] details a method for plotting the angle loops of this system. Due to the monodromy of this system, the angle loop displays a topological change when going around a monodromy circuit, called a static manifestation of monodromy, see Fig. 3.3.
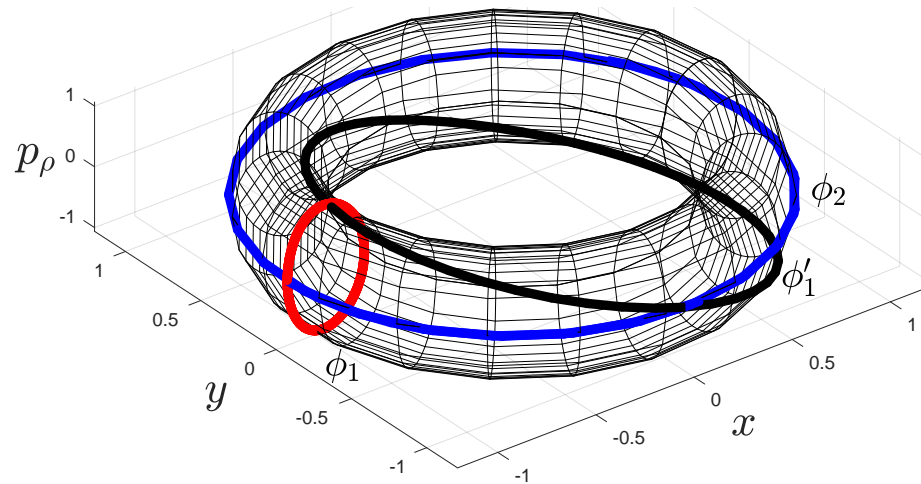
Figure 3.3: The original ϕ_1 (red) and ϕ_2 (blue), plotted on a torus. After going around the monodromy circuit, ϕ_1 smoothly changes into $\phi'_1 = \phi_1 + \phi_2$ (black).

Chapter 4

Static Monodromy: Double Well System

In this section, we will look at a generalization of the previous situation: a system with two monodromy points. The hydrogen atom in crossed electric and magnetic fields is a system with two monodromy points [7, 8]. We sought a simpler system with some of the same properties. The work in this chapter is all new.
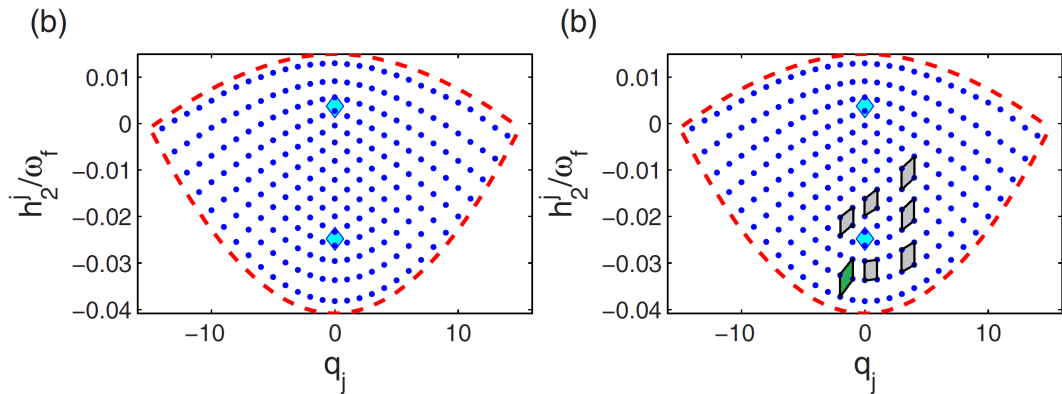

Figure 4.1: The quantum spectrum of a spinless hydrogen atom in near-perpendicular electromagnetic fields. The lattice has two defects, each shown as cyan diamonds. The inception of the system discussed in this chapter was inspired by this work. Compare with Figs. 4.2 and 8.1. This figure is taken from [8]. A monodromy circuit of a unit cell of the quantum spectrum is shown in the right figure, compare the original unit cell (grey) with the final unit cell (green).

4.1   Double Monodromy Point System

Here is our simplified model

$$V(\rho) = -a\rho^2 + b\rho^4 - c\rho^6 + d\rho^8 \quad (a, b, c, d > 0) \tag{4.1}$$

$$H(\mathbf{q}, \mathbf{p}) = \tfrac{1}{2}\mathbf{p}^2 + V(\rho) = h \tag{4.2}$$

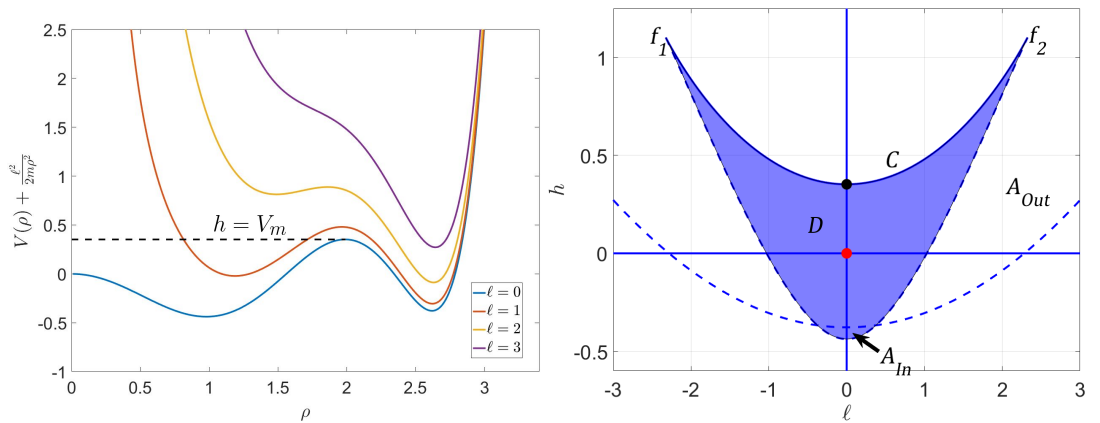$$L(\mathbf{q}, \mathbf{p}) = xp_y - yp_x = \ell \tag{4.3}$$

Figure 4.2: (Left) Potential energy plotted vs. ρ for various values of angular momentum ℓ. Parameter values used in this plot, as well as throughout this entire section are: $a = 1.04$, $b = 0.75$, $c = 0.157$, $d = 0.01$. (Right) The Bifurcation Diagram of the system, showing classically allowed regions as well as singular points and lines. The two monodromy points are shown as the black and red dots and correspond to the peaks of the potential at $\ell = 0$.

This system has two monodromy points: one at $(\ell = 0, h = 0)$ and another at $(\ell = 0, h = V_m)$, where V_m corresponds to the local maximum of $V(\rho)$ at $\ell = 0$, see Fig. 4.2. The structure of (ℓ, h)-space is shown in Fig. 4.2. There is an open set D (the shaded region, but above the dashed line) corresponding to the region where both wells are classically allowed, meaning the fiber $\mathbf{F}^{-1}(\mathbf{f})$ is the disjoint union of two smooth tori, $\mathbf{T}_{In}^2$ and $\mathbf{T}_{Out}^2$. There are two regions where only one well is classically allowed and thus only one torus. These are A_{In}, which is the shaded region below
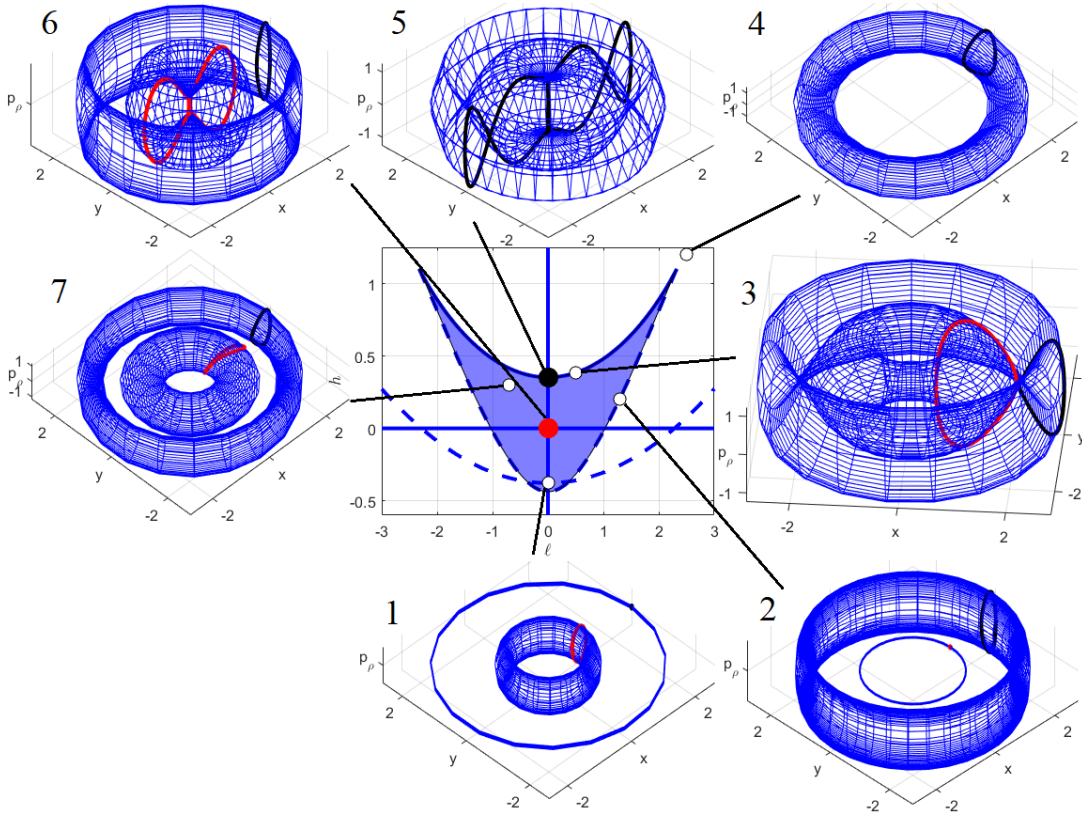
Figure 4.3: Each of the fiber types present in the Bifurcation Diagram of the double well system. Pictured are (1) torus $\mathbf{T}^2_{In}$ and circle $\mathbf{S}^1_{Out}$, (2) torus $\mathbf{T}^2_{Out}$ and circle $\mathbf{S}^1_{In}$, (3) bitorus bi$\mathbf{T}^2$, (4) torus $\mathbf{T}^2_{Out}$, (5) pinched bitorus bi$\mathbf{T}^2$, (6) pinched torus $\mathbf{T}^2_{In}$ and torus $\mathbf{T}^2_{Out}$, and (7) torus $\mathbf{T}^2_{In}$ and torus $\mathbf{T}^2_{Out}$.

the dashed line, and A_{Out}, the white region above the dashed line. The two dashed lines correspond to values where one of the tori degenerates into a circle, either $\mathbf{S}^1_{In}$ or $\mathbf{S}^1_{Out}$. The points along the solid line C (not including the endpoints f_1 and f_2), each correspond to a bitorus bi$\mathbf{T}^2$, which can be thought of as the two tori $\mathbf{T}^2_{In}$ and $\mathbf{T}^2_{Out}$ joined along a azimuthal orbit. This structure is very similar to ones seen in systems with "bidromy" which also contain continuous lines of bitori. However, the structure in this system is not exactly the same swallowtail catastrophe seen in those systems (see [21]), largely due to the Hamiltonian containing a second order angular momentum term $\frac{\ell^2}{2m\rho^2}$. All of the structures discussed in this section can be seen in Fig. 4.3 and the reader is encouraged to examine it carefully.

The derivation for the multivalued action-angle variables for this system are in direct correspondence with the derivation in the previous section, so the arguments will not be repeated here. However, we have two tori, and therefore two radial actions. We must therefore keep track of two different winding numbers, one for each of the monodromy points, and apply same fix stated in Eq. 3.16 for both Δ_{In} and Δ_{Out}.

$$\Delta_{In} = \Delta_{In}(\ell, h) + 2m\pi$$

$$\Delta_{Out} = \Delta_{Out}(\ell, h) + 2n\pi$$

(4.4)

Here, m, n increase by 1 for each counterclockwise winding about their respective monodromy points, and decrease by 1 for each clockwise winding. The result is that the angle loops of this system have two distinct static manifestations of monodromy, which can be seen in Figs. 4.4 and 4.5. The first manifestation, Fig. 4.4, shows the topological change of an angle loop (red) of the inner torus as it traverses a monodromy circuit that encloses the lower (red) monodromy point, but does not enclose the black monodromy point. This is exactly the same as the change found in the Mexican-hat system. The loop on the outer torus is unaffected.

The second manifestation, Fig. 4.4, shows the topological change of an angle loop (black) of the outer torus as it traverses a monodromy circuit that encloses the upper (black) monodromy point. Again, it is very similar to the Mexican-hat system in that it also involves only one component, the outer torus in this case. The inner torus is present at low energies, but it collapses to a circle and then disappears outside the blue shaded region.

To help understand the manifestations of monodromy (and related phenomena) for a particular system, it is often useful to construct an object called an *unfolded bifurcation diagram*. Each point on this surface corresponds to only one component of the fibration, e.g. a single torus or bitorus. The unfolded bifurcation diagram for our system can be seen in Fig. 4.6. This is useful particularly in Fig. 4.5, because this object allows us to see how we are following only one component of the fibration (the
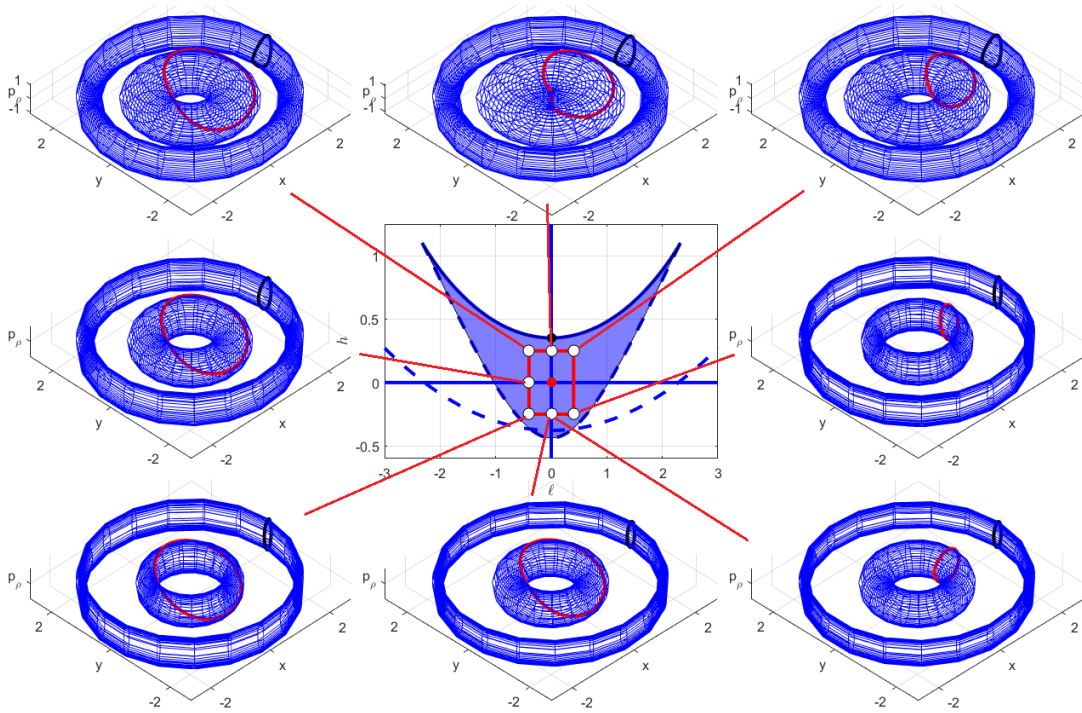
Figure 4.4: A static manifestation of monodromy about the first of two monodromy points that exist in this system. The angle loop undergoes a topological change analogous to the previous Mexican-hat example. To read this figure, begin in the lower right hand corner and proceed around the monodromy circuit counter-clockwise from torus to torus, following the shape of the red angle loop at each step.

outer torus) on a path that crosses the dashed line, which denotes the disappearance of the inner torus. The inner monodromy circuit shown in Fig. 4.4 stays on the tongue of the unfolded diagram, and thus it too involves only one component (the inner torus).

We have not yet discussed what occurs in this system when one crosses the continuous line C of bitori. There is a discontinuity of the action variables on this line. Analysis of the precise behavior of the action variables near lines of this type (often called "separatrix crossings") have been studied in other contexts [33] [34]. To close approximation, crossing this line can be thought of as a summation of the inner and outer radial actions, see Fig 4.7. This summation of action can be calculated to be
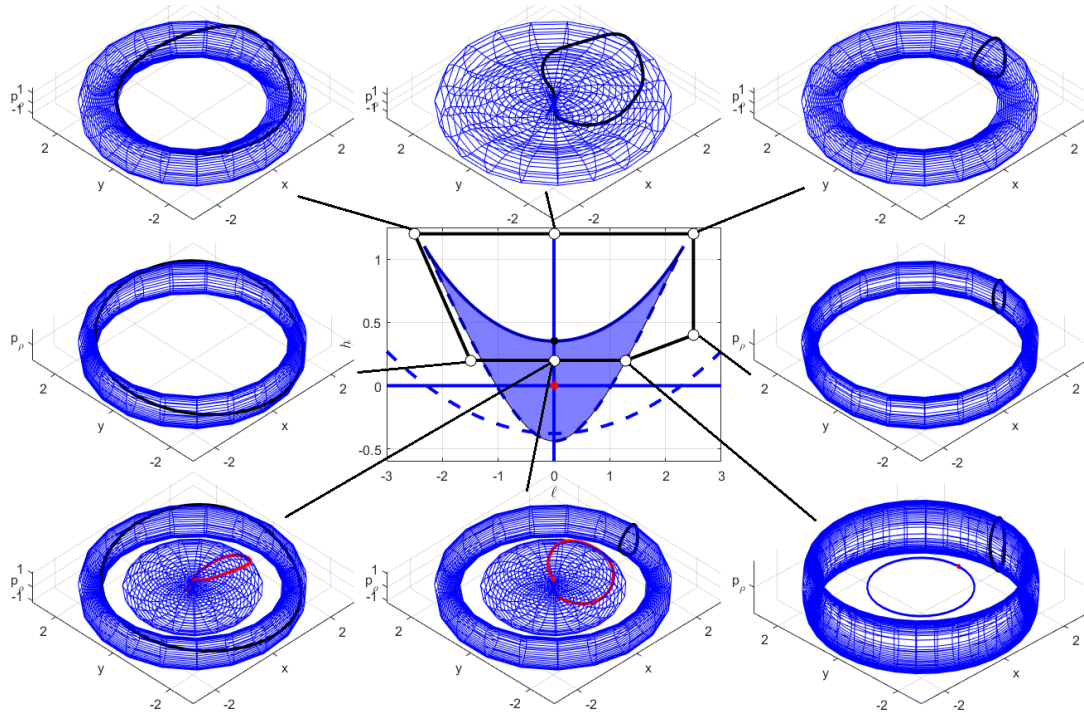
Figure 4.5: A static manifestation of monodromy about the second of two monodromy points that exist in this system. This path crosses the dashed line that separates the two regions with one and two tori, respectively. It is on this line that one of the tori degenerates to a circle. To read this figure, begin with the lower middle torus and proceed around the monodromy circuit counter-clockwise from torus to torus, following the shape of the black angle loop at each step.

$$\mathcal{I}_{Above}(\ell, h) \approx \mathcal{I}_{Below,In}(\ell, h) + \mathcal{I}_{Below,Out}(\ell, h)$$

$$\frac{1}{2\pi} \oint_{Above} \mathcal{P}(\rho) \cdot d\rho \approx \frac{1}{2\pi} \oint_{Below,In} \mathcal{P}(\rho) \cdot d\rho + \frac{1}{2\pi} \oint_{Below,Out} \mathcal{P}(\rho) \cdot d\rho \tag{4.5}$$

Further analysis of crossings like this were not pursued, since a more rigorous approach is beyond the scope of this work on monodromy, which is more interested in global properties of such quantities.
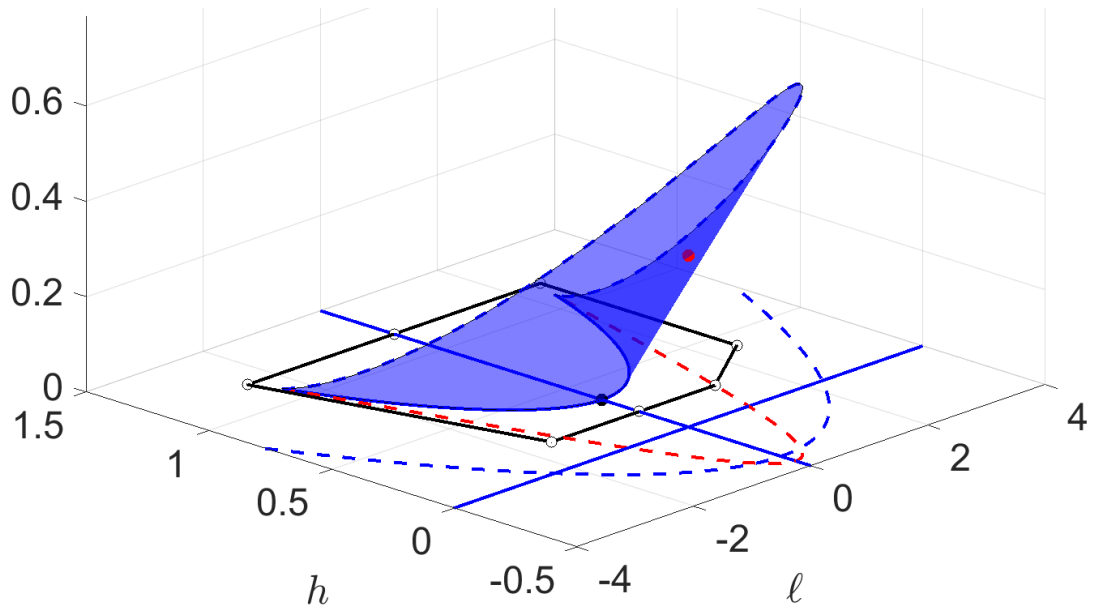
Figure 4.6: The unfolded bifurcation diagram of the double monodromy system. The figure can be thought of as an unfolding of Fig. 4.2 so that each point on the surface corresponds only to one component of the fibration, be that a torus, bitorus or circle. The different regions are depicted in the same color and style as Fig. 4.2. Additionally, the lower curve connecting points f_1 and f_2 is projected onto the lower surface as a red dashed line. Also plotted is a monodromy circuit from Fig. 4.5 (and that is also very similar to Fig. 6.3). The unfolding shows clearly how this path encloses only one of the monodromy points.
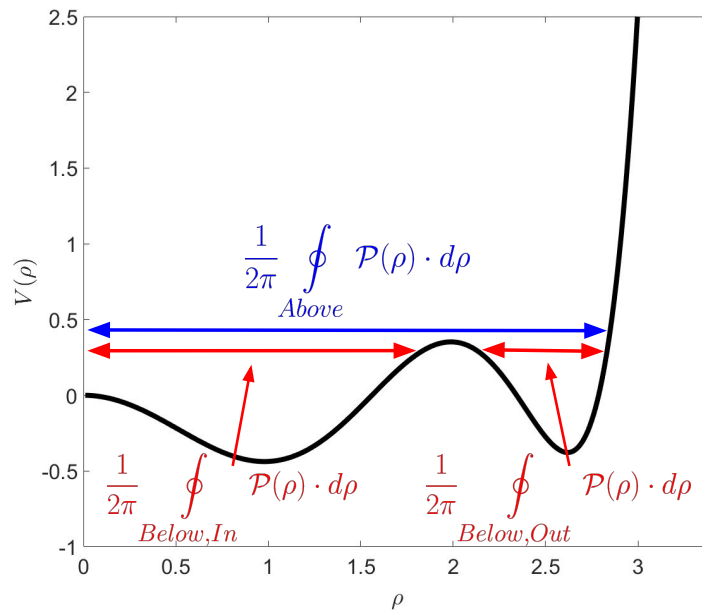

Figure 4.7: The summation of radial actions above and below the crossing $\mathcal{C}$

Chapter 5

Dynamical Monodromy

5.1 The Phenomenon

We show for the first time an experimental demonstration of dynamical manifestations of Hamiltonian monodromy. This was published in [39]. The discussions of the previous chapters were for static manifestations of monodromy. We examined how angle coordinates on (ℓ, h) tori changed along the monodromy circuit, and these static manifestations have been observed before [31]. What if instead of looking at the tori at different (ℓ, h) values along the monodromy circuit, we dynamically change the system's angular momentum and energy? We can add an additional perturbing force that drives a system around a monodromy circuit and evolves it from one torus to the next.

$$\Lambda_{(\ell^i, h^i)} \rightarrow \Lambda_{(\ell(t), h(t))} \rightarrow \Lambda_{(\ell^f, h^f)} \tag{5.1}$$

In "dynamical monodromy," this same topological change can be implemented by driving a loop of non-interacting particles around a monodromy circuit. First we start with a family of non-interacting particles on the initial torus ($\ell = 0, h < 0$) with initial positions and momenta corresponding to the ϕ_1 canonical angle loop of Fig. 3.3. In position space, particles oscillate radially between the inner and outer classically forbidden regions as shown in Fig. 5.1 I. Then we apply external forces to dynamically

change the particles' angular momenta and energies, following a monodromy circuit in spectrum space, $(\ell(t), h(t))$, around the monodromy point.

The Mexican-hat system was shown previously to exhibit dynamical monodromy theoretically [29]. We will now go through the several steps that are required to drive the particles adiabatically and dynamically around the circuit show in Fig. 5.1. (i) Start all particles with the same energy $h_0 < 0$ and angular momentum $\ell = 0$ as shown in Fig. 5.1 I. (ii) Apply external forces so that the particles are given positive angular-momentum and begin to rotate counterclockwise around the classically forbidden region, shown in Fig. 5.1 II. (iii) Increase the energy of each particle to $h > 0$, shown in Fig. 5.1 III. (iv) Reduce the angular momentum to zero (When we focus on the structure of the loop in configuration space, this is the critical point on the monodromy circuit). (v) Continue to reduce the angular momentum to a negative value. During this evolution (steps iii-v), the angular-momentum is zero for an instant and the classically forbidden central region vanishes simultaneously, shown in Fig. 5.1 IV. After this critical moment, the classically forbidden region reappears *inside* the loop and we see the predicted topological change, shown in Fig. 5.1 V. The family of particles had been confined to one side of the classically forbidden region, but now the family surrounds the forbidden region. The remainder of the monodromy circuit returns the angular-momentum and energy to their initial values. (vi) Reduce the energy of each particle to $h < 0$ as seen in Fig. 5.1 VI. (vii) Apply final torques to bring the angular-momentum back to zero and the energy to the initial value h_0. Under "ideal" evolution, all particles have equal angular-momenta and energies at any given time, and the final values are equal to the initial values. However the topological structure of the loop of particles has changed, as seen in Fig. 5.1 I and VIII.

The loop of particles cannot be broken, but it is initially on one side of the classically forbidden region I, and at the end it surrounds the forbidden region VIII. Computation[27–29] has shown that the loop of particles follows the behavior of the angle loop: at the end of the circuit, the loop will have changed its topological structure. This topological change is the very definition of dynamical monodromy. The loop of
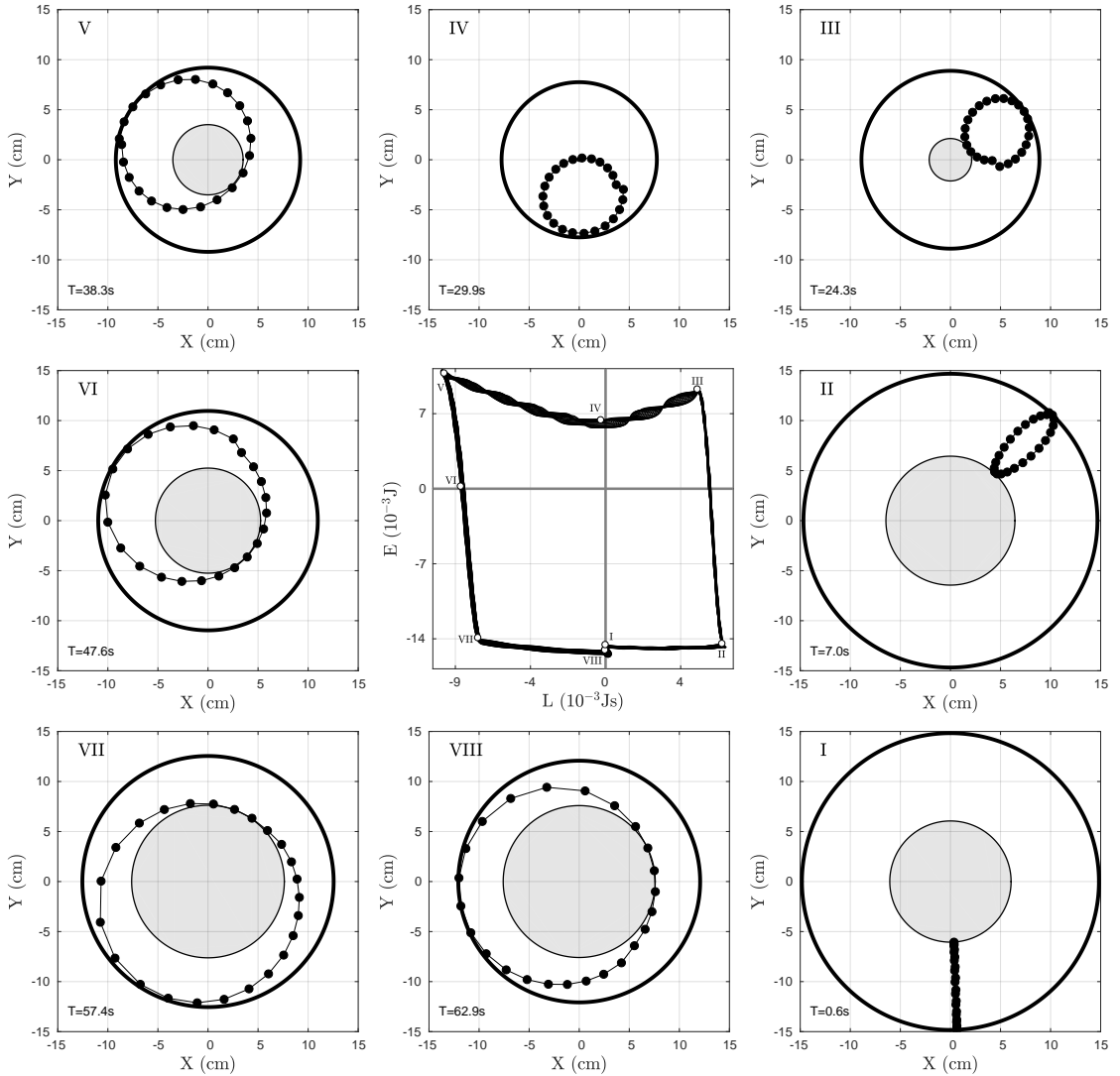
Figure 5.1: A dynamical monodromy circuit for the Mexican-hat system. To read this figure, turn 90° and begin in the lower right hand corner. Proceed counter-clockwise around the monodromy circuit. The loop of particles, initially on one side of the classically forbidden region, proceeds to enclose the forbidden region as the particles complete the circuit. The paths traveled by these particles in spectrum space are shown in the center plot, with snapshots corresponding to each Roman numeral. The individual steps of the circuit are outlined in the body of the text, see Sec. 5.1. This plot was generated from computer simulations of experimental data, details of which are outlined in Sec. 5.2.

particles, as it evolves in time, has experienced the same topological change as the angle loops in Fig. 3.3. In the following section, we carry out this process in the laboratory.

5.2 Dynamical Monodromy Experiment

This section outlines the first experimental observation of dynamical monodromy [39] and describes the apparatus and results in detail.

5.2.1 Our System: A Magnetic Pendulum

To realize this evolution in a classical experiment, we can observe a family of trajectories of a single object with different initial conditions instead of several non-interacting particles. We constructed a spherical pendulum using a rigid Al rod (length $d = 2.502 \pm 3.2 \times 10^{-3}$ m) with a permanent magnet at its end. The kinetic energy for our spherical pendulum is $KE = \frac{1}{2} I_{\text{pend}}(\sin^2\theta \, \dot{\phi}^2 + \dot{\theta}^2)$, where θ and ϕ are the typical spherical coordinate system, see Fig. 5.2. The rigid pendulum and magnet together have a moment of inertia I_{pend}. The magnet[1] is a cylinder neodymium magnet of mass 382.0 ± 0.1g and magnetic moment $|\mu| = 56.8 \pm 0.35$J/T. It was modeled as a dipole moment $|\mu|$ aligned coaxially with the pendulum.

$$\boldsymbol{\mu} = \frac{|\mu|}{d} \left(-x\,\hat{x} - y\,\hat{y} + \sqrt{d^2 - x^2 - y^2}\,\hat{z} \right) \tag{5.2}$$

A circular coil placed beneath the center of the pendulum provides a cylindrically symmetric repulsive force on the magnet creating the inner barrier of the potential well. Thus the full Hamiltonian is

$$\mathcal{H} = KE + V_{\text{well}} = KE + (m_d d_{cm} + md)g\cos\theta - \boldsymbol{\mu} \cdot \boldsymbol{B}_{\text{coil}}, \tag{5.3}$$

where m_d is the mass of the rod (713 ± 1g), m is the mass of the magnet, d_{cm} is the

---

[1]Specifically, the magnet is a K&J Magnetics RY04X0.

center of mass of the pendulum, and $\boldsymbol{B}_{\mathrm{coil}}$ is the magnetic fields from the center coil [40].

The torus seen in Fig. 5.10 was plotted using the P_θ momentum as cast as a function of the energy and angular momentum,

$$P_\theta = \left\{ 2I_{\mathrm{pend}} \left(h - \frac{\ell^2}{2I_{\mathrm{pend}} \sin^2 \theta} \right) \right\}^{1/2}. \tag{5.4}$$

After differentiation, the equations of motion take the form

$$\ddot{\theta} = (\dot{\phi}^2 I_{\mathrm{pend}} \cos(\theta) \sin(\theta) - (\frac{d_{cm}}{d} m_d + m) gd \sin(\theta) - \frac{dV_{well}}{d\theta})/I_{\mathrm{pend}} - \beta\dot{\theta} \tag{5.5}$$

$$\ddot{\phi} = (-2\dot{\phi}\dot{\theta} I_{\mathrm{pend}} \cos(\theta) \sin(\theta) - \frac{dV_{well}}{d\phi})/(I_{\mathrm{pend}} \sin^2(\theta)) - \beta\dot{\phi}, \tag{5.6}$$

where β is introduced as a uniform damping friction term to be measured experimentally. This was done by fitting experimental data of our pendulum's motion with numerical integration of our model Hamiltonian, see Fig. 5.3. From this fitting, moment of inertia $I_{\mathrm{pend}} = 4.12 \pm .01 \, kg \cdot m^2$, damping constant $\beta = 6.0 \pm .3 \times 10^{-3} \frac{1}{s}$, magnetic moment $|\mu| = 56.8 \pm 0.35 \mathrm{J/T}$ and center coil vertical position $z_c = -10.5 \pm .1 \, cm$ were extracted.

5.2.2 Electronic Components and Experimental Implementation

The magnitude of current in the center coil defines the height of the inner barrier. Instead of adjusting the energy of the pendulum, we can decrease the current (and the resulting field-strength of the central coil), lowering the barrier. The center coil is a composite 4 layer stacked coil, with each layer hand wound on a lathe using copper ribbon wire and cast in epoxy. Each coil has an inner radius of 3.8 cm and an outer radius of 7.3 cm and had 40 turns of wire. They were then mounted to perpendicular 3-d printed plastic sliding stages to allow for transverse alignment with the vertical axis of the hanging pendulum. These stages were custom made using a $\frac{1}{4}$" brass bolt
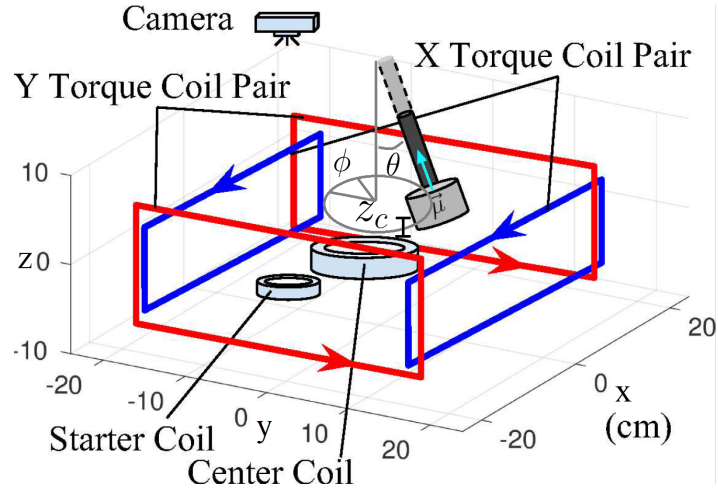
Figure 5.2: A diagram of our apparatus. Shown (to scale) are the starter coil, central barrier coil, torque coils. The magnet, camera position and pendulum are also shown (not to scale), though the pendulum extends beyond the top of the figure.

and had an approximate precision of .3mm translations.

A camera recording at thirty frames per second mounted above the system tracks the pendulum's position. Due to the slight curvature of the trajectory of the pendulum (as seen by the camera) and the camera viewing off axis, an interpolated pixel-to-real space map was generated by manually placing the pendulum and snapshotting each location of a 700 point grid. We use a Savitzki-Golay (SG) convolution[41] to smooth the pendulum's position data. Similarly, the velocity was found with a five point first order SG convolution. Subsequent quantities, such as the energy and angular momentum, were calculated using the SG-smoothed position and velocity. The experiment used eighteen "particles" (i.e. initial conditions) on the initial angle loop. In Figs. 5.1 and 5.10, we connect initially adjacent particles to visualize the loop in configuration and phase space.

To control the angular momentum, four square coils surround the perimeter of the pendulum and are connected in two Helmholtz pairs. Partially inspired by the design of time-orbiting-potential (TOP) traps for cold atoms[42], this configuration is shown in Fig. 5.2. The coils were hand wound with copper wire on a laser cut acrylic frame. This frame also provided a static background for determining the position of
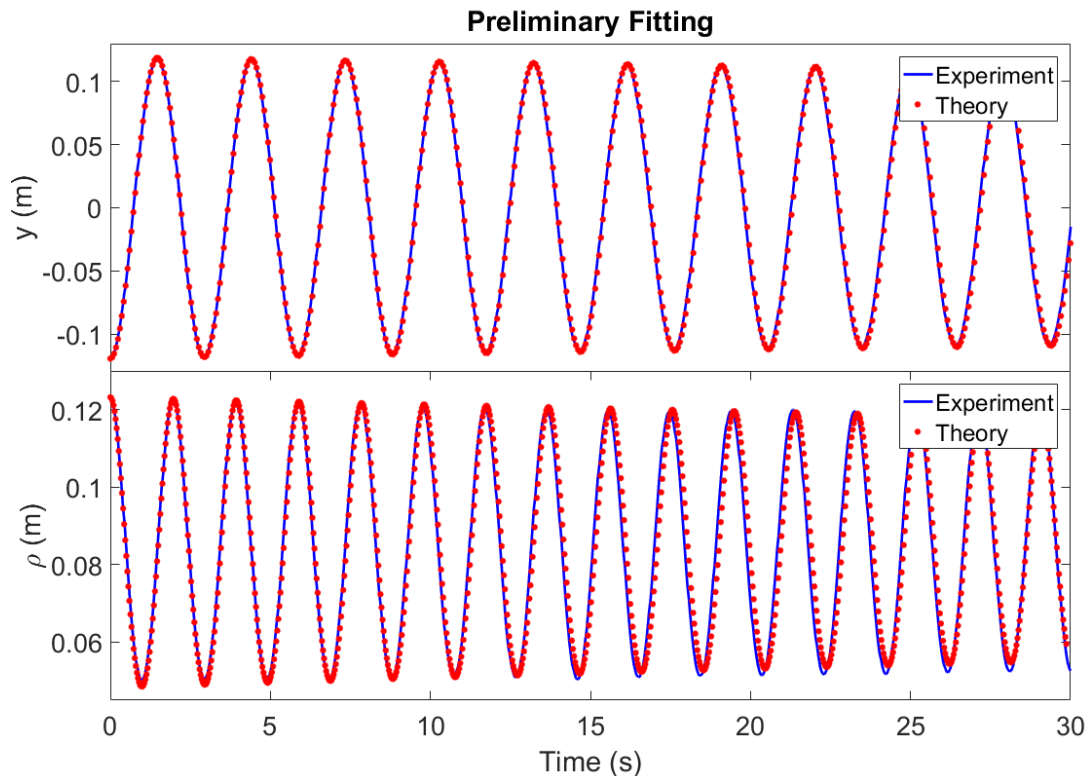
Figure 5.3: Preliminary data to determine various parameters of our experiment. (Top) This shows the free motion of the pendulum while all electronics are off. From this run, moment of inertia $I_{\mathrm{pend}} = 4.12 \pm .01\, kg \cdot m^2$ and damping constant $\beta = 6.0 \pm .3 \times 10^{-3}\frac{1}{s}$ were extracted by fitting the motion of the model Hamiltonian to our data, also shown. (Bottom) A similar preliminary run showing the radial motion of the pendulum bouncing off a constant center barrier generated by the coil. By fitting this run, the magnetic moment $|\mu|$ and center coil vertical position $z_c = -10.5 \pm .1\, cm$ were extracted. β was also re-measured in this case, and was consistent with its previous measurement. The breakdown in this fit is likely due to probably asymmetries in the center coil potential or inaccurate alignment of the center coil with the pendulum.

the pendulum from the acquired images. Expressions for the fields generated by these coils are taken from [43]. A full configuration of the coils and their positioning in relation to the pendulum is shown in Fig. 5.2 and a photograph of the data acquisition region of the pendulum is shown in Fig 5.4. Table 5.1 summarizes the dimension of the torque coils.

The forces from these torque coils on the pendulum can sum in any direction in the xy plane (any force along the length of the pendulum is negated by its rigidity). By

	X Torque Coils	Y Torque Coils
Length (cm)	48	45
Height (cm)	11.25	14
Distance from center (cm)	21.25	20.5

Table 5.1: Dimensions of the torque coils in cm. All of the torque coils have 55 turns each.
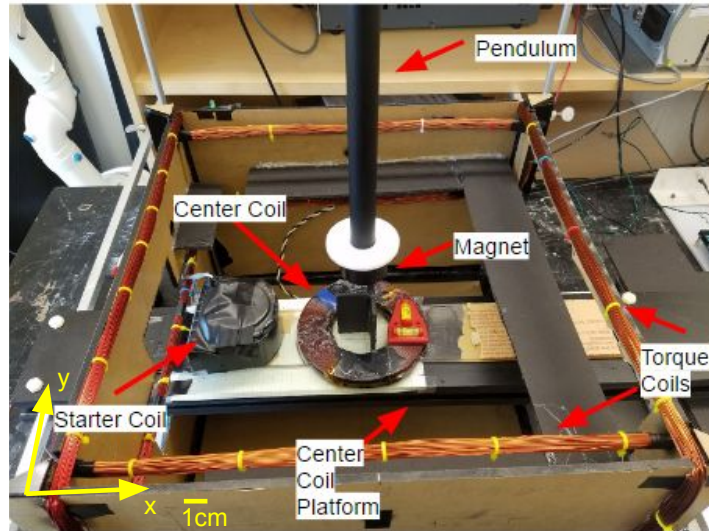

Figure 5.4: An annotated photo of our experimental apparatus with each of the components from Fig 5.2 labeled. The coils are mounted on an acrylic frame with aluminum supports.

adjusting the currents in these coil pairs, we can create and maintain a net azimuthal force on the magnet, thereby controlling the angular momentum of the pendulum. The potential generated by the torque coil pairs ($V_{\mathbf{mag}} = \boldsymbol{\mu} \cdot \mathbf{B}$) for various values of current can be seen in Fig. 5.5. Tilting of the magnetic moment as the pendulum swings in an arc is accounted for in the potentials shown in Fig. 5.5 and is required to understand the behavior of the pendulum in Helmholtz generated fields.

The timing of changes of current in these coils is set by the precession frequency of the pendulum for each particular initial condition, as determined by a priori simulation, as seen in Fig. 5.8. This simulation is a numerical integration of our model Hamiltonian given the initial conditions obtained via the camera. We do not have any active feedback
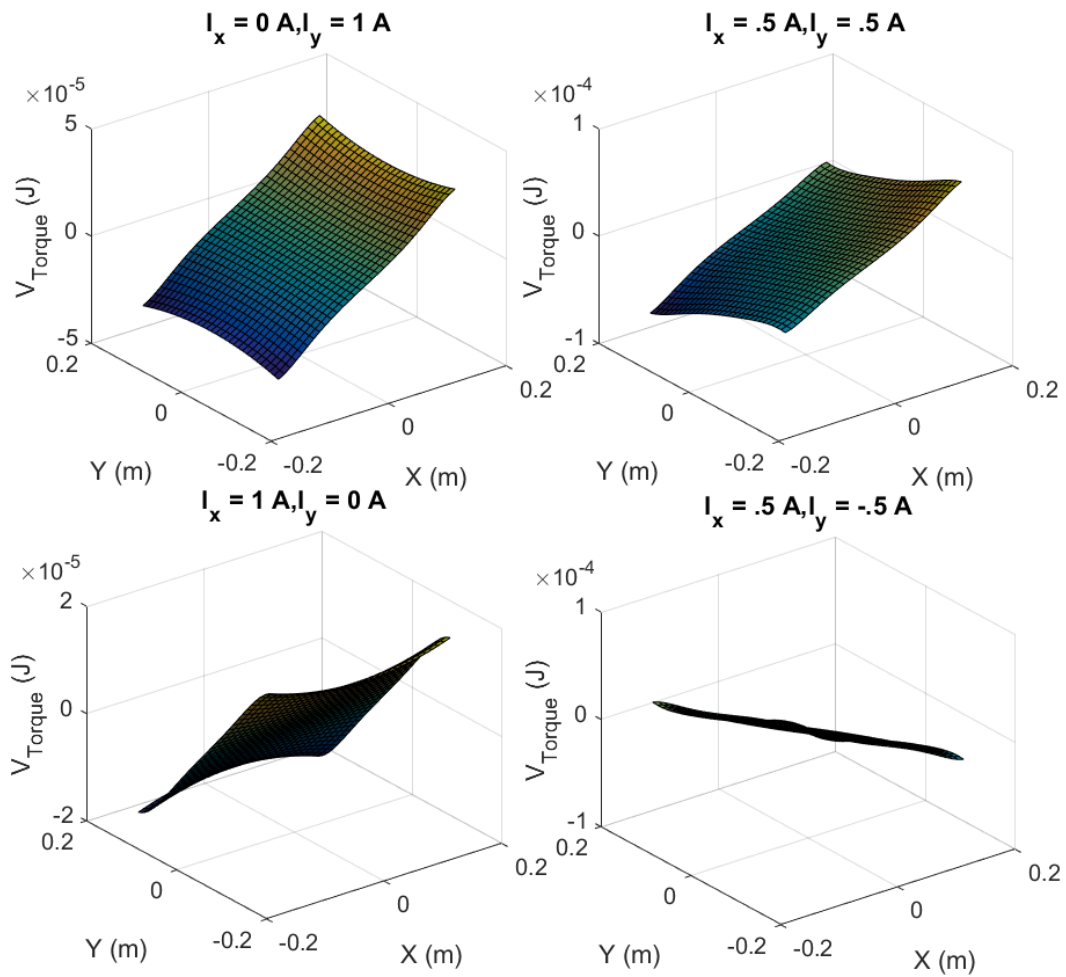
Figure 5.5: Potentials generated by the square torque coils for various values of current. For these potentials, current in the center coil $I_{center} = 0$. By controlling the currents, the force can be rotated to torque the pendulum and move it along the monodromy circuit.

system to adjust the forces to the instantaneous location of the pendulum. Lastly, there is a small coil off-center, beneath the pendulum. This is a starter coil and can be turned on and off quickly with a MOSFET circuit, as it is used to capture and release the pendulum cleanly and from a consistent location, creating our loop of initial conditions.

All of the electronics are managed via an Arduino micro-controller[2]. The control circuitry is bipolar in design, due to the requirements of the torque coils, and connects

---

[2] Arduino Due Model A000062

Arduino outputs to the current source inputs through inverting op-amp circuits. The torque coils required a fast response and were therefore controlled via the on-board digital analog converter outputs (DAC's), while the center coil was controlled through a pulse width modulated (PWM) signal, see Fig. 5.7. The power supplies driving the torque coils are bipolar, with one being a Kepco BOP 20-5 and the other a lab-built current cource. The center coil is driven by a Kepco ATE 25-10 and the starter coil is driven by a Kepco ATE 15-15. A connected diagram of each component of our electronics setup can be seen in Fig. 5.6. Arduino code for a monodromy data taking run is shown in Appendix B.1.

A difficult aspect of this experiment is that, because the potential energy in Eqn. 5.3 is cylindrically symmetric, the angular motion of the pendulum is at best neutrally stable. There are small instabilities in the pendulum's motion caused by possible asymmetries in the center coil. Further exacerbating the stability is the timing of the external "torquing" forces, as they are dependent on the predicted position of the pendulum at any given time. Any deviation between the pendulum's actual and simulated position will grow due to a non-ideal torque being applied. Hence the pendulum easily drifts away from the location computed in the simulation, and "torque" forces can destabilize the angular motion. For these reasons we record multiple trials[3] for each "particle" on the loop. When we plot the positions of the particles, we use the "trimmed mean," the mean position of the middle 50% of the experimental runs.

5.2.3   Experimental Results

Fig. 5.10 V compares the experimental data with simulation right after the monodromy circuit has crossed the critical point $(\ell = 0, h > 0)$. The steps that occur in Fig. 5.10 are the same as in Fig. 5.1 and the red loop of particles in Fig. 5.10 is the same as the loop of particles in Fig. 5.1. We begin by kicking the particles, see Fig. 5.10I, followed by lowering the barrier to bring the pendulum to an energy higher than the barrier peak, as seen in Fig. 5.10 II-III. This is followed by a torque in the opposite

---

[3]For a given initial condition, i.e. "particle," we record either five or ten trials.
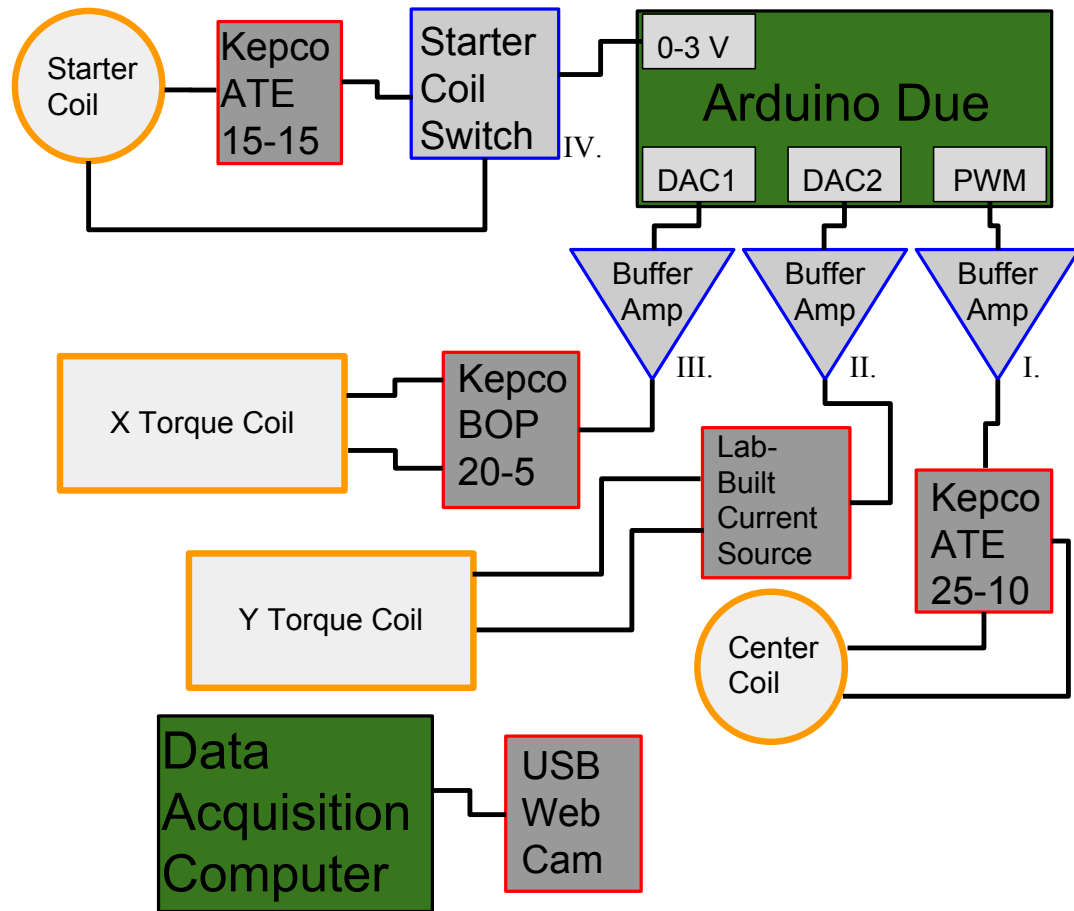
Figure 5.6: The complete setup of the circuitry for independently controlling each of the four coils. The Arduino signals to each of the four power supplies through associated circuits, each of which are shown in detail in Fig. 5.7 (the Roman numerals in this figure are in correspondence with Fig. 5.7). The data were acquired separately via the USB webcam shown near the bottom.

direction to bring the particles from positive angular momentum towards negative angular momentum, as seen in Fig. 5.10 IV. It is at this point in the circuit the loop of particles has changed from being on one side of the classically forbidden region to surrounding it instead, as seen upon examining Fig. 5.10 IV-VII.

Comparing with the simulation of the monodromy circuit in Fig. 5.10 we see that our experiment has followed a slightly different monodromy circuit. As a result of the spread in spectrum space and especially the angular drift of particles from their simulated positions, the family was unable to complete the monodromy circuit by
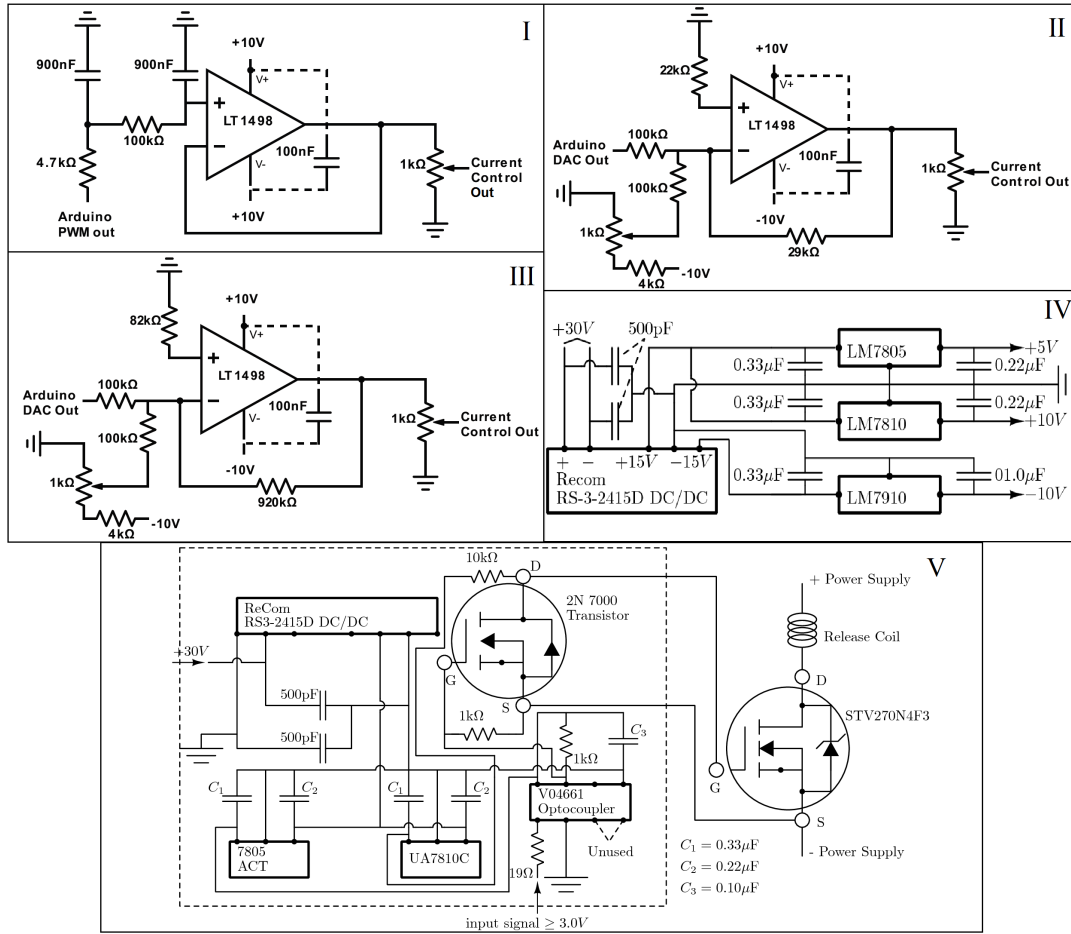
Figure 5.7: Schematics of the control circuitry built to interface the Arduino with the driving current sources used in the experiment. (I-III) These are inverting amplifier circuits that take the Arduino analog output signal and convert it to bipolar signals the power supplies can read. (IV) A floating DC supply circuit for creating necessary supply voltages in Circuits I-III and V. (V) A floating MOSFET Driver circuit controlling the release of the starter coil. The dotted box region is the driver circuit, external to the high-current MOSFET (STV270N4F3). The input signal from the Aruduino determines if current can flow through the MOSFET transistor, making the MOSFET an electronically controlled on/off switch for the release coil.

returning to $\ell = 0$. This spread is post apparent in the steps after the one shown in Fig. 5.10 V. Fig. 5.9 shows this spread in energy and angular moment for one example particle. Nevertheless, the topological change is robust and visible in Fig. 5.10 IV-VII. This process of a loop of particles, reasonably localized together in spectrum space, and moving from positive to negative angular momentum is the intended phenomenon

we wished to observe.

This experiment could be improved by more accurate means of alignment of the center coil to prevent drift. Additionally, development of a system of instantaneous determination and response to the location of the pendulum at any given was considered (i.e. a "feedback system"), but ultimately deemed unnecessary. Such a system would in principle reduce inconsistencies in torques between trials.
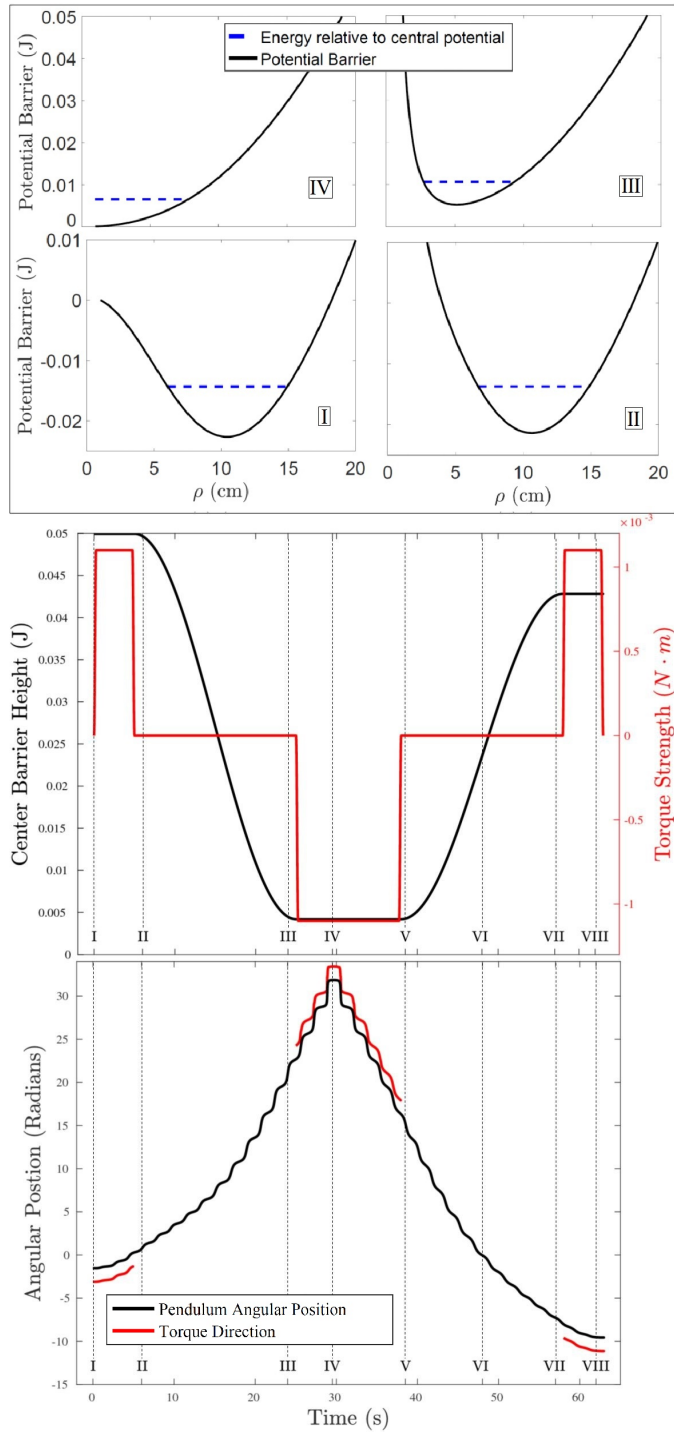
Figure 5.8: Experimental control and timing (Top) These plots show the potential barrier, $V(\rho) + \ell^2/(2m\rho^2)$, at the first four time steps. The Roman numerals match with Figs. 5.1 and 5.10. Zero energy is in reference to the coil potential energy at $\rho = 0$. (Middle) The timing sequence of our experiment, showing the barrier height and magnitude of torques on each particle. The difference in initial and final barrier heights is a characterization of the energy lost due to friction over the course of the experiment. (Bottom) A representative timing sequence of the torque coils tailored a priori to keep an azimuthal applied force for a particular trajectory (this figure is shown for the particle that begins on the outer turning radius).
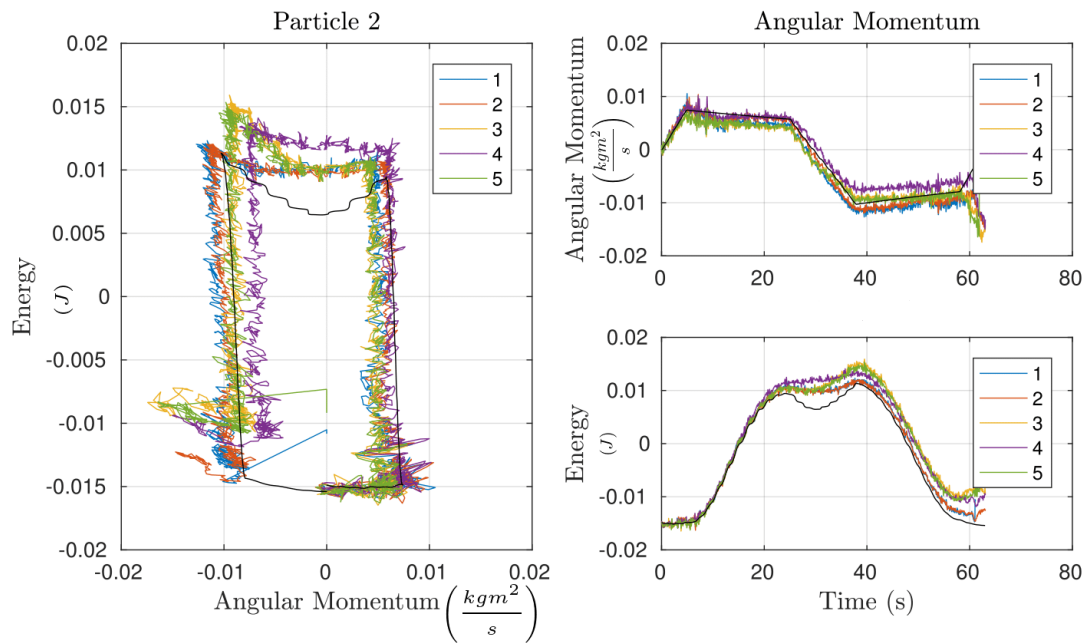
Figure 5.9: Energy and angular momentum for each run of an individual trajectory. These runs were then Cartesian averaged and presented in the data in Fig. 5.10. Shown are the path in spectrum space (left) as well as the time dependence of both energy and angular momentum (right). The black line is the theoretical path as determined by the model Hamiltonian.
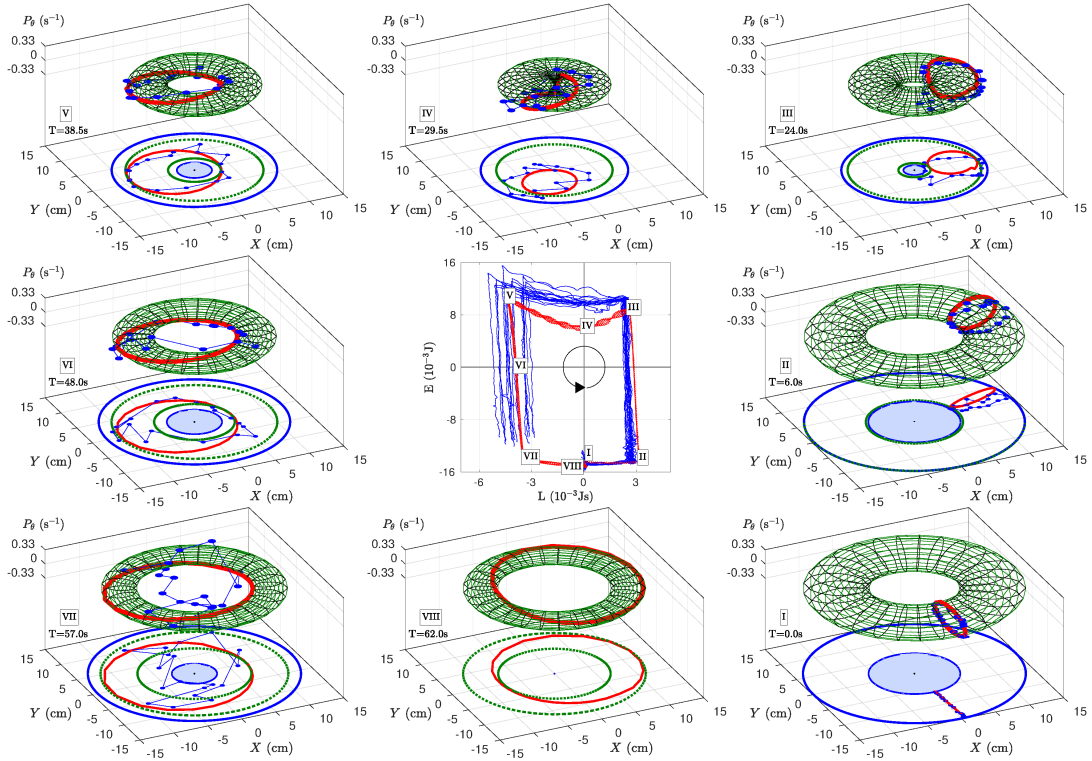
Figure 5.10: A dynamical monodromy loop with theory (red) and experiment (blue). The red loop is the same loop shown in Fig. 5.1. The center plot shows the monodromy circuit in spectrum space while the outer plots are snapshots of the torus and loop of particles at marked points along the circuit. The torus was plotted using P_θ, defined in Eq. 5.4, using simulation data. The filled blue sections in XY-space are the inner turning radii for the experimental data and the green dash circles are projections of the inner and outer radii of the tori. The loop of particles undergoes a topological change (see III and V) as the classically forbidden region disappears in the intervening time, IV. Comparing I and V, the loop of particles has experienced the same change as the static monodromy angle loop, Fig. 3.3. I and VIII correspond to the same torus defined by $(\ell = 0, h < 0)$. By this time however, the experiment has diverged from the ideal path and does not complete the circuit.

Chapter 6

Dynamical Monodromy: Double Well System

In this section, we will examine the dynamical monodromy properties of the previously discussed system with two monodromy points, see Section 4.1. Following an analogous procedure, it is quick to show that loops of particles in this system dynamically experience topological changes in correspondence with each of the angle loops shown in Figs. 4.4 and 4.5, see Figs. 6.2 and 6.3.

In each case, we start with a loop of particles that are on an angle loop. In the first case, Fig. 6.2, the particles begin in the inner well. This is because the trajectory in spectrum space is topologically equivalent to the one in Fig. 4.4, so we want to begin the particles on the angle loop that exhibits the topological change in that figure. As can be seen in Fig. 6.2, the particles show the associated topological change by surrounding the origin.

There are many possible schemes for the application of forces required to drive a loop around a monodromy circuit, and here we choose one of the simplest. For the portions of the loop that adjust the angular momentum, we apply a purely azimuthal force $F_{Trq} = .015$. This force also will adjust the energy of the particles, as can be seen by the upward curving of those portions of the monodromy loop. For the vertical
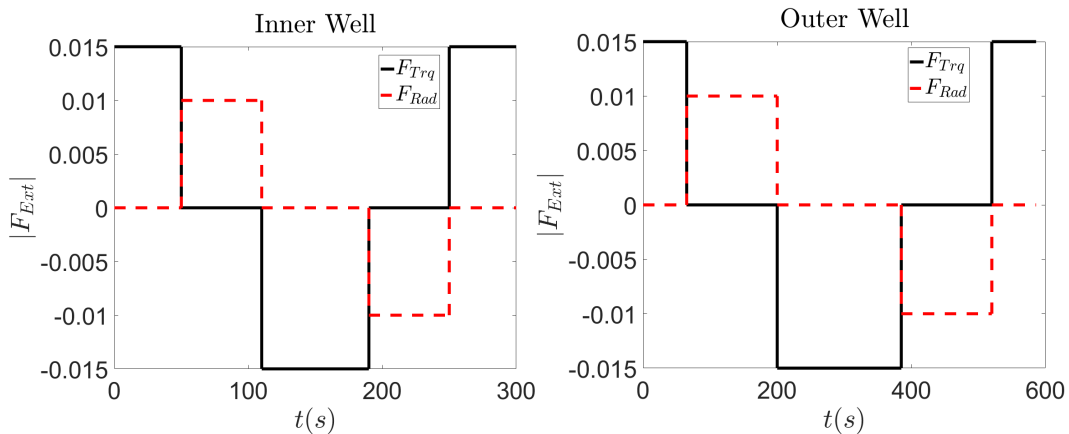
Figure 6.1: The timing of torques and radial forces on the particles for the inner dynamical loop (left) and the outer dynamical loop (right). The magnitude of azimuthal torques are shown in solid black while the radial forces are shown in dashed red.

portions of the loop, we apply a purely radial force $F_{Rad} = .01$. These forces are turned on and off instantaneously at different times during the evolution, as can be seen in the timing sequences shown in Fig. 6.1. A positive value of these forces correspond to increasing their respective spectrum space value (angular momentum for F_{Trq} and the energy for F_{Rad}), whereas a negative value corresponds to working against the particle and decreasing these values.

In the second example, we follow a dynamical monodromy circuit that is topologically equivalent to the loop shown in Figs. 4.5 and 4.6. In this case, it is the outer torus's angle loop that exhibits the topological change, which is why the loop of particles begin in the outer well. This monodromy circuit is not as smooth as Fig. 6.2. This is due to small variations in the torques and boosts each particle receives in the simulation as they oscillate radially. However, the topological change is still apparent in comparing the initial and final states in Fig. 6.3. A more careful choice in torquing scheme may allow for a neater loop at this point in its evolution [29].

Figure 6.2: A dynamical monodromy circuit associated with the inner torus and that encloses the lower monodromy point. To read this figure, begin in the lower right hand corner and proceed around the monodromy circuit counter-clockwise from torus to torus. In this procedure, all of the particles remain in the inner well at all times. The inner turning points of each classically allowed region are shown as red circles while the outer turning points are shown in blue.
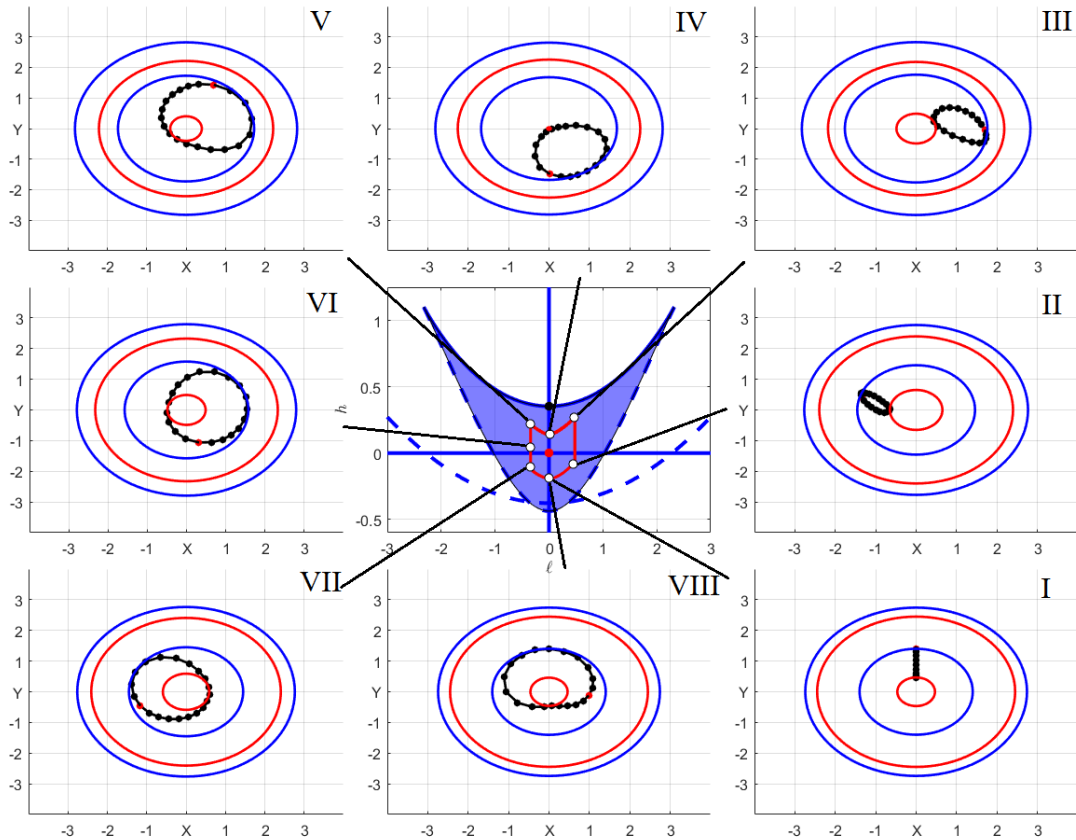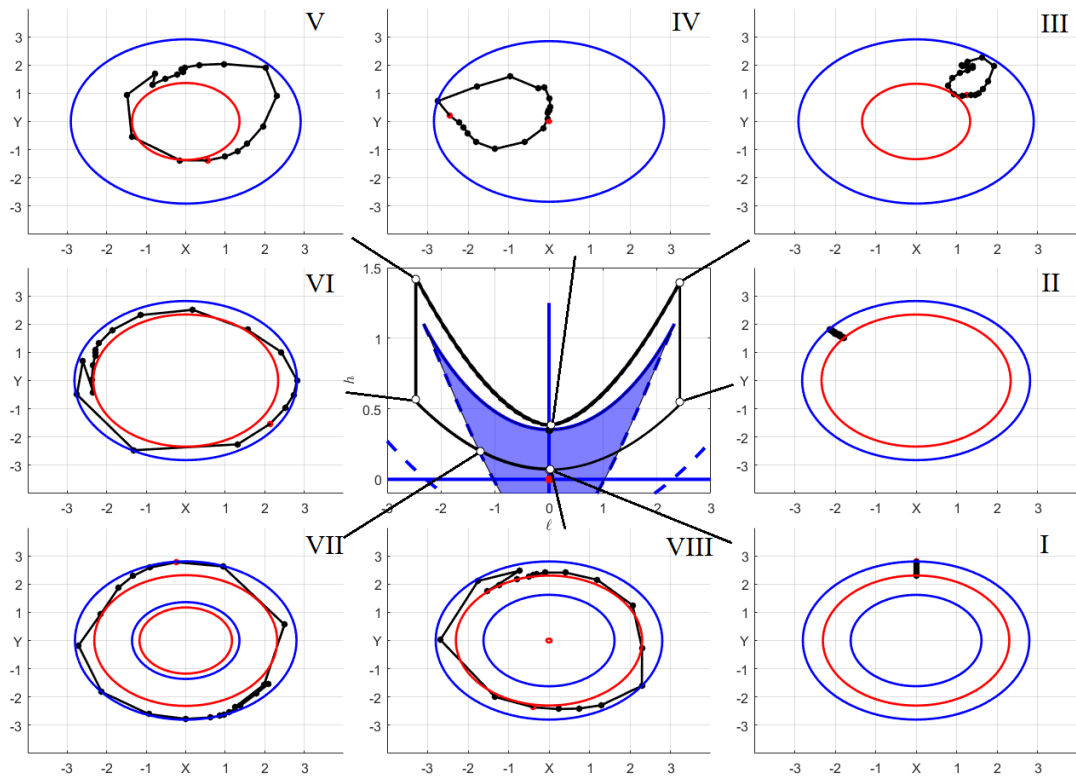
Figure 6.3: A dynamical monodromy circuit associated with the outer torus and that encloses the upper monodromy point. To read this figure, begin in the lower right hand corner and proceed around the monodromy circuit counter-clockwise from torus to torus. In this procedure, all of the particles remain in the outer well at all times. For the steps that the loop is in the unshaded region of (ℓ, h)-space, the outer well is the only classically region. The inner turning points of each classically allowed region are shown as red circles while the outer turning points are shown in blue.

Chapter 7

Quantum Monodromy: Mexican Hat System

In the previous few chapters, we have been analyzing all of the ways in which monodromy and related phenomena manifest themselves in the action-angle variables and behavior of classical particles in each of the systems. However, monodromy has a quantum aspect as well, which has been known theoretically nearly as long as it has been known classically [5]. The most typically associated aspect of quantum monodromy is a spacial defect in the lattice of allowed eigenvalues of the system [1, 44]. This means that a unit cell of the lattice does not retain its shape when taken around a monodromy circuit, see Fig. 7.1.

It has also been shown that quantum wavefunctions themselves exhibit topological changes in analogy with the angle loops [45]. The purpose of this chapter is to briefly summarize the most important results and concepts of this previous work which are necessary for understanding the original work in the following chapter. All of the figures and calculations from this chapter are from [45].

7.1 Smooth Action and Semiclassical Eigenstates

As was stated in the introduction, quantum eigenenergies can be calculated with good accuracy by quantization of action

$$\mathcal{I}_2 = \ell = m\hbar$$
$$\mathcal{I}_1(m, h_{m,n}) \approx (n - \frac{1}{2}\hbar)$$

$$(7.1)$$

For systems with monodromy, there is another labeling of quantum states that is useful

$$\mathcal{I}_1'(m, h_{m,n_s}) \approx (n_s - \frac{1}{2}\hbar) \tag{7.2}$$

where $\mathcal{I}_1'$ is the smooth but multi-valued action variable and n_s is the quantization of that action, often called the "smoothed" action variable. The multivalued nature carries over into the assignment of n_s. If we begin with $n_s = n$ with $m > 0$, then upon crossing the line $\ell = 0$, $h > 0$ n_s becomes $n_s = n - |m|$. This is a useful concept because there are many dynamical processes in which a classical system follows contours of smooth action and corresponding quantum systems follow n_s. Fig. 7.1 shows the quantum spectrum for the Mexican hat system, along with contours of smooth action.
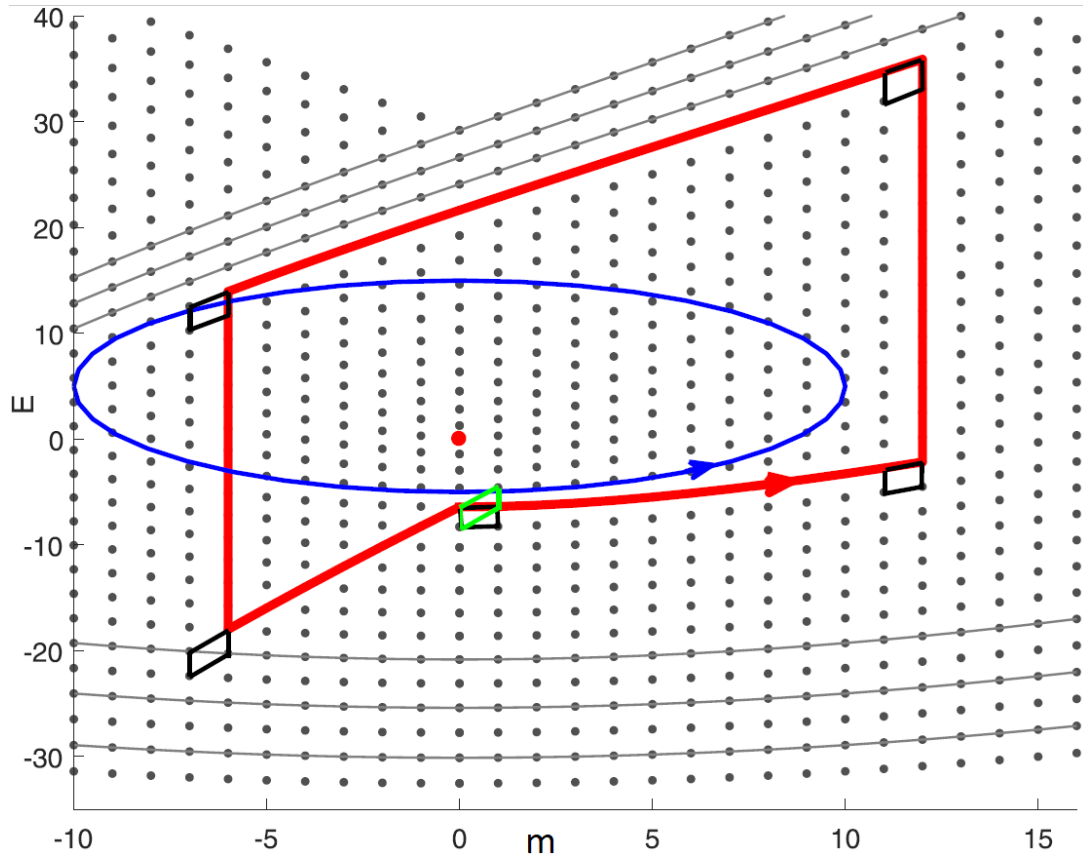
Figure 7.1: The spectrum space picture of the quantum Mexican hat. Shown are semiclassical eigenvalues (which are identical to the exact values at this scale), contours of smooth action (grey) and an example monodromy circuit (red). The red dot denotes the monodromy point. The defect in the lattice is shown by carrying a unit cell around this monodromy circuit and can be seen to have changed its shape upon returning to itself. This figure is taken from [45].

7.2 Monodromy of Wavefunctions

Here we define a set of nonstationary superposition states that display a topological change similar to that of angle loops. This is done by first defining a superposition of eigenfunctions of the Hamiltonian which have the appearance of the angle loop in configuration space. For reasons that are explained in [45], the superposition that is most closely localized to an angle loop is a Gaussian:

$$\psi(\rho, \phi) = \sum_m C_{m,n_r} \chi_{m,n_r}(\rho, \phi)$$

$$C_{m,n_r} = \exp\left[-\left(\frac{m - \hat{m}}{2.5}\right)\right]^2 \tag{7.3}$$

Here, $\chi_{m,n_r}(\rho, \phi)$ refers to Mexican hat eigenfunctions. Taking this superposition around a monodromy circuit subsequently changes the structure of the loop to encapsulate the barrier. Fig. 7.2 shows these superpositions and the monodromy circuit used while Fig. 7.3 plots the wavefunction and shows the topological change. Reference [45] shows this behavior of the quantum Mexican hat by hopping from state to state statically, or by continuous unitary time-dependent transformations driving the expectations values of (ℓ, h), and by a physically realizable time-dependent Hamiltonian with an "appropriate radiation field".
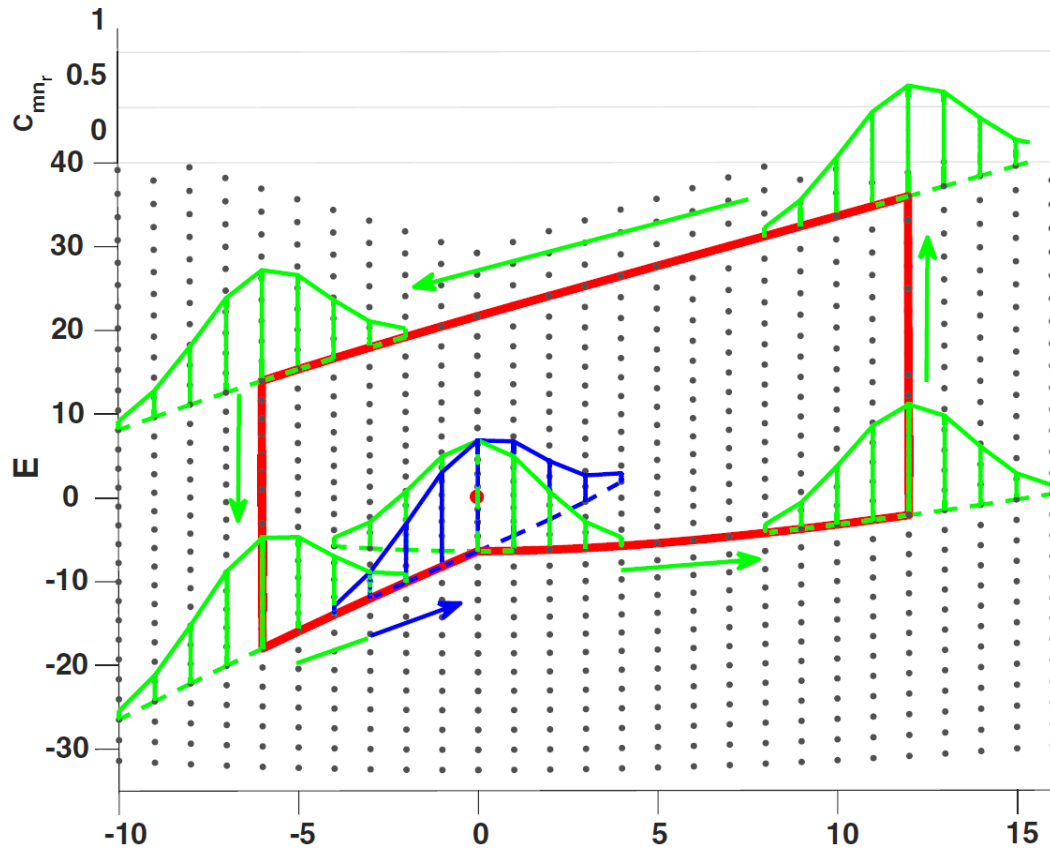
Figure 7.2: A 3 dimensional plot of the coefficients of the superposition C_{m,n_r} on (ℓ, h). The gray dots correspond to eigenvalues of the Mexican hat. The superpositions are Gaussian. Each leg of the monodromy circuit follows a contour of a smooth action (the two vertical portions follow contours of constant $\mathcal{I}_2 = m\hbar$ and each other portion follows contours of the smoothed action $\mathcal{I}_1'$). Fig. 7.3 corresponds to the top right and top left portions of the circuit, the portion which showcases the desired topological change. It is also worth noting that upon traversing the entire monodromy circuit, the superposition has changed to a different superposition (shown in blue). This figure is taken from [45].
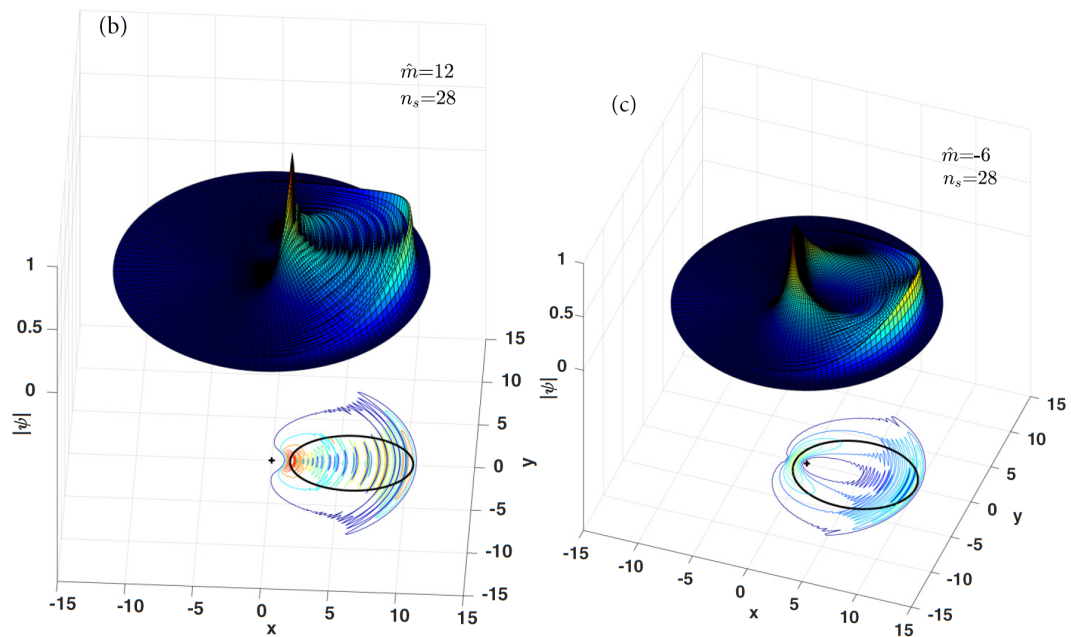
Figure 7.3: The change in topology of a wavefunction superposition of the Mexican hat system upon traversing the top portion of a monodromy circuit. Shown here is the magnitude of the wavefunction with a contour map below it. The equivalent angle loop is highlighted in black and the origin is shown with a black star to highlight the change in topology. This figure is taken from [45].

Chapter 8

Quantum Monodromy: Double Well System

In this section, we show that the results from [45] carry over to this system with two monodromy points. We begin by looking at the semiclassical eigenstates shown in Fig. 8.1. Eigenenergies can be approximated by a Bohr-Sommerfeld quantization of the radial action integral

$$\mathcal{I}_1(\ell, h) = \frac{1}{2\pi} \oint \sqrt{2m\left(h - V(\rho) - \frac{\ell^2}{2m\rho^2}\right)} d\rho = (n + \frac{1}{2})\hbar. \qquad (8.1)$$

The contours of constant action were integrated numerically using

$$\left(\frac{\partial H}{\partial L}\right)_{\mathcal{I}_1} = -\frac{\partial \mathcal{I}_1/\partial L}{\partial \mathcal{I}_1/\partial H} = -\frac{\Delta_1(\ell, h)}{T_1(\ell, h)} \qquad (8.2)$$

where the definitions of Δ_1, the azimuthal angle subtended in a cycle of ρ motion, and T_1, the time of first return in the radial coordinate, have been used (see Eqns. 3.14 and 3.15).

By looking at this lattice of eigenstates, the change in the unit cell when traversing a monodromy circuit can be seen plainly in Fig. 8.1.

In analogy with the correction to the action variables in section 3.1, we can define a smooth quantum number n_s. We do this so that we have a quantum number that

does not change as we follow a contour of smooth action above a monodromy point from the right-hand side to the left-hand side of Fig. 8.1. n_s is defined as

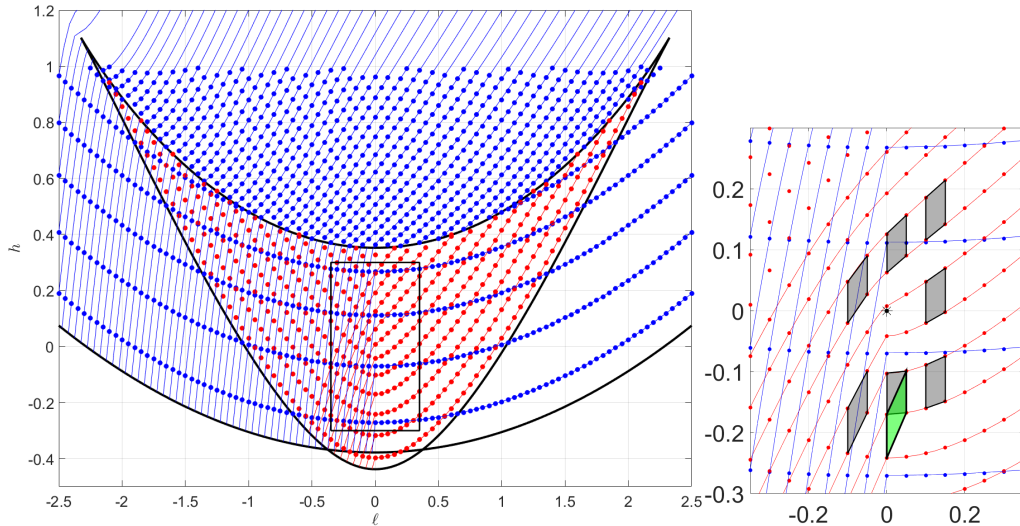$$n_s = \begin{cases} n & \ell \geq 0 \\ n - |\ell| & \ell < 0 \end{cases} \tag{8.3}$$

Figure 8.1: The quantum spectrum of the double well system. Plotted are inner well semiclassical eigenstates (red) and outer well semiclassical eigenstates (blue). Contours of constant radial action are also plotted with red again corresponding to the inner well and blue corresponding to the outer well. The change in the unit cell of the lattice of quantum eigenstates around a monodromy circuit is plotted on the right hand side zoomed portion. For this figure and throughout this chapter, we use a value of $\hbar = .05$

8.1   Wavefunction Monodromy

It was shown in [45] that a wave packet centered on a single angle loop shows the same topological change when taken around a monodromy circuit. It was also shown that the wave packet that is localized to an angle loop is a Gaussian superposition in ℓ, centered on its expectation value, $<\ell>$, and following the contour of smooth action. This loop can be represented by

$$\Psi(\rho, \phi) = \sum_{\ell,n} c_{\ell,n} R_{\ell,n}(\rho) e^{i\ell\phi}, \tag{8.4}$$

where the $R_{\ell,n}(\rho)$ are the radial eigenfunctions of the system and the $c_{\ell,n}$ are coefficients of a Gaussian distribution in ℓ,

$$c_{\ell,n} = e^{-\pi\left(\frac{\ell-<\ell>}{5}\right)^2}. \tag{8.5}$$

This superposition can be seen in Figs. 8.3 and 8.5.

Next, we must calculate the radial wavefunctions. This was done numerically as an expansion in circular box eigenfunctions: Bessel functions.

$$R_{\ell,n}(\rho) = \sum_i N_{\ell,i}^{(n)} J_\ell(k_{\ell,i}\rho) \tag{8.6}$$

This expansion was truncated to 200 terms. To check for convergence, these numerical eigenstates were compared with WKB approximated radial eigenfunctions, see Fig. 8.2.
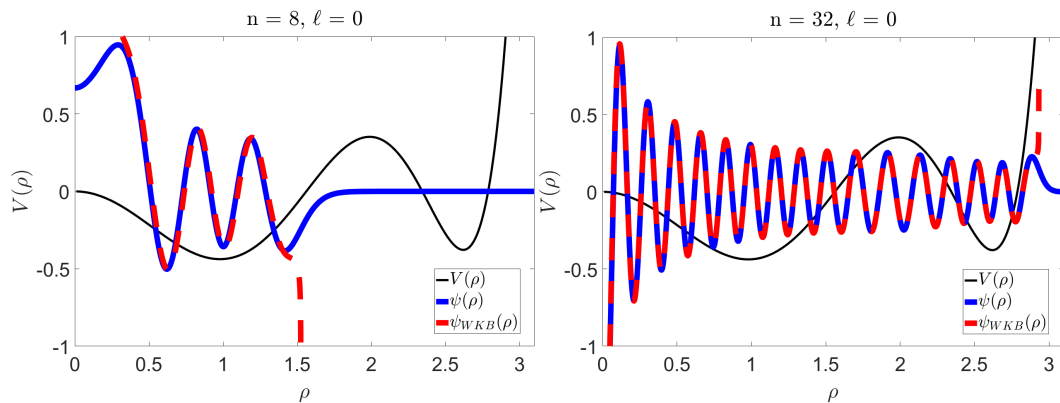
Figure 8.2: Radial wavefunctions for the n = 8 and n = 32, $\ell = 0$ states. Both the numerical expansion in Bessel functions (blue solid line) as well as a WKB aproximation (red dashed line) are plotted. WKB wavefunctions were calculated to ensure good convergence of the numerical eigenstates. We have good agreement in the classically allowed regions, where the WKB approximation does not diverge.

Now that we have the radial eigenfunctions, we can proceed to plot the angle loop superposition states. As the results in [45] show, only the top portion of the monodromy loop needs to be plotted in order to see the associated topological change. However, since we have two monodromy circuits, we go through plotting the top portion of each.

The superpositions are shown in Figs. 8.3 and 8.5, while the wavefunctions themselves are shown in Figs. 8.4 and 8.6. For each of these plots, the wavefunctions are not transformed in any time-dependent manner.

Figure 8.3: The top portion of a quantum monodromy circuit for the lower monodromy point, shown with a green star. The Gaussian superposition begins on the right hand side and travels along a contour of smooth action to the left hand side. The topological change of the wave function(and equivalent angle loop) is shown in Fig. 8.4.

We expect that the results from [45] show that this work could be generalized to continuous time-dependent transformations of the wavefunctions, either through ideal unitary transformation or physical forces.

Figure 8.4: Wavefunction monodromy of the lower monodromy point. The surface plot is the wavefunction itself, while a contour plot of the wavefunction is shown underneath. Also shown underneath are the equivalent angle loops (black). The origin is also designated with a red star to highlight the topological change.
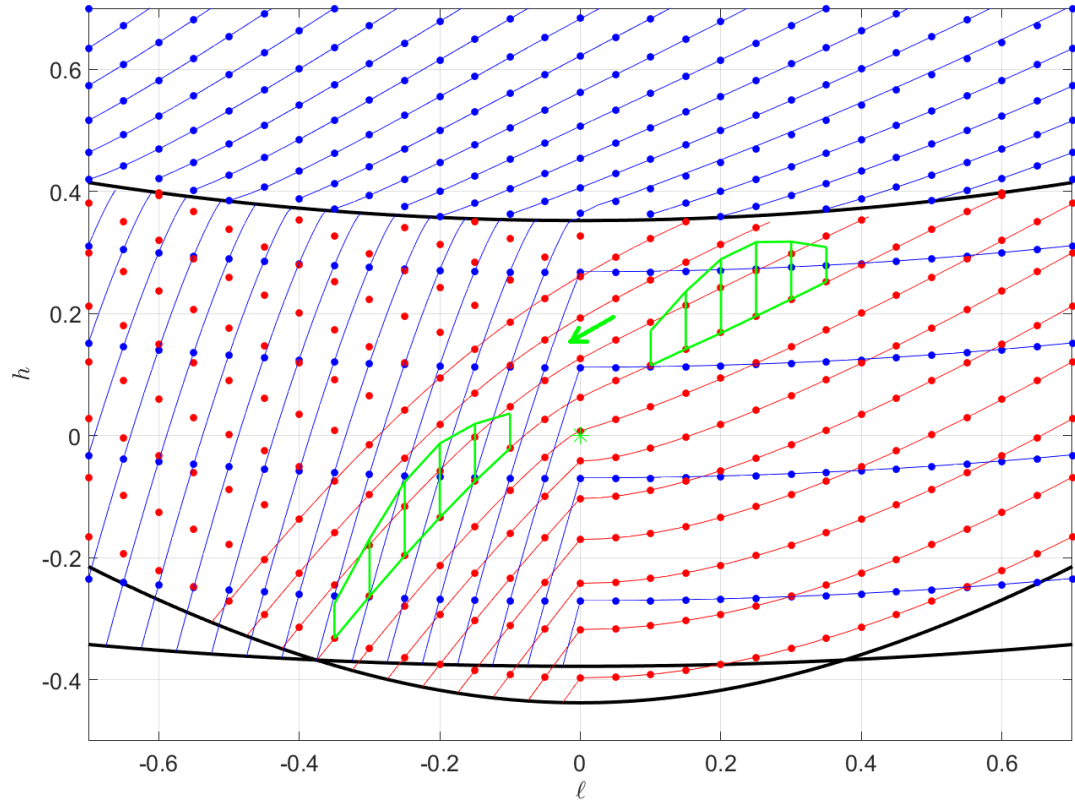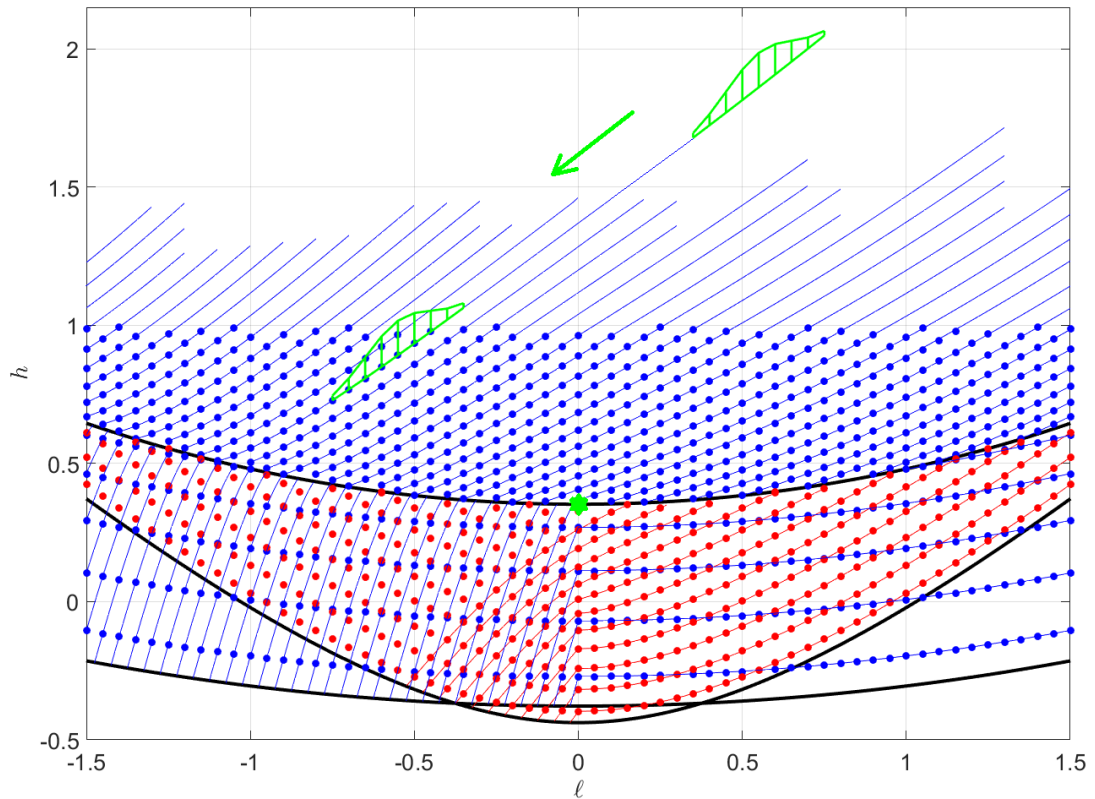
Figure 8.5: The top portion of a quantum monodromy circuit for the upper monodromy point, shown with a green star. The Gaussian superposition begins on the right hand side and travels along a contour of smooth action to the left hand side. The topological change of the wave function(and equivalent angle loop) is shown in Fig. 8.6.
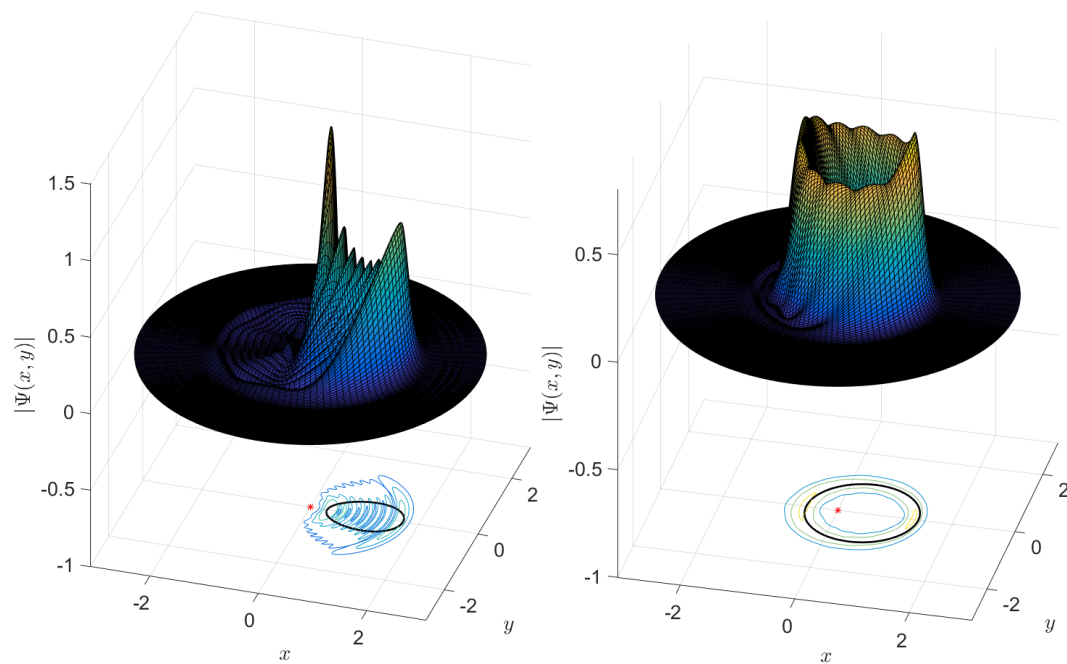
Figure 8.6: Wavefunction monodromy of the upper monodromy point. The surface plot is the wavefunction itself, while a contour plot of the wavefunction is shown underneath. Also shown underneath are the equivalent angle loops (black). The origin is also designated with a red star to highlight the topological change.
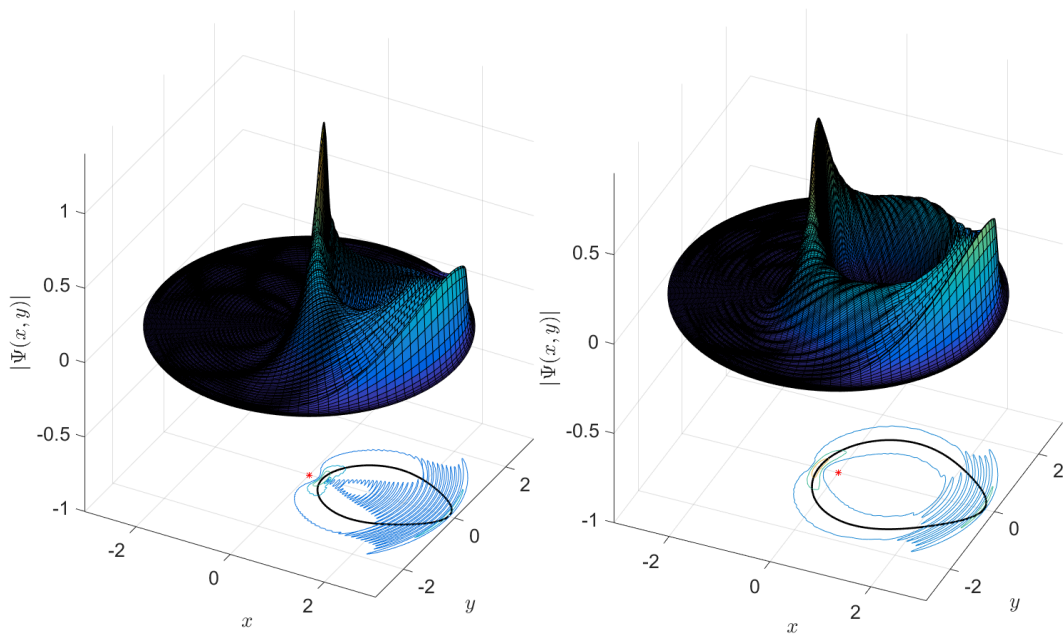
Chapter 9

Conclusions and Outlook

As stated in the introduction, new phenomena in classical mechanics do not appear frequently. This dissertation explores previously unknown manifestations of Hamiltonian monodromy, which are the consequences of multivalued action and angle variables in some integrable dynamical systems. We summarize much of the background mathematics on these types of systems needed to understand and contextualize with previously established results, including concepts of symplectic geometry, Lagrangian manifolds, and action-angle variables. The design and implementation of the first experimental observation of dynamical manifestations of monodromy are outlined, as well as our experimental results. These same theoretical techniques are applied to a novel system with two monodromy points, and many of the previously established results of monodromy were shown to carry through. The results include topological changes of the fundamental angle loops, dynamical monodromy of loops of particles, and topological changes of quantum wavefunctions themselves.

There is much left to be known about monodromy and related phenomena. There are immediate questions concerning generalization of dynamical and quantum wavefunction monodromy to the related phenomena of bidromy and fractional monodromy. The work on the double monodromy point system presented herein may provide some answers, because it features the same continuous line of bitori in its bifurcation diagram. A more complete theory tying together global concepts of monodromy with local

concepts of separatrix crossings is desirable, especially since fractional monodromy presents similar features [34].

On the experimental side, there are other candidate systems for observations of dynamical monodromy, including cold atom systems [29]. At present, Perry Nerem is exploring manifestations of monodromy in optical systems. It is not yet known what applications monodromy may have in such systems. The answer may lie in bridging the gap of this work on monodromy with work on geometric phases in similar systems in solid state physics, such as graphene Dirac quantum dots [46]. Topological states of quantum systems are of much interest currently, due to speculations regarding their use in implementing topological quantum computing schemes.

Appendices

Appendix A

Supplemental Proofs

A.1   Fundamental Poisson Bracket Identities

Using the J-product definition of a Poisson Bracket we show that the fundamental Poisson bracket identities, Eq. 2.29, are necessary and sufficient conditions for a transformation to be canonical. The three Poisson brackets in Eq. 2.29 can be succinctly written as

$$
\begin{aligned}
J_{ij} &= \langle \nabla_{\mathbf{z}} Z_i | \underline{J} | \nabla_{\mathbf{z}} Z_j \rangle \\
&= \langle \underline{\tilde{M}} \nabla_{\mathbf{Z}} Z_i | \underline{J} | \underline{\tilde{M}} \nabla_{\mathbf{Z}} Z_j \rangle \\
&= \langle \nabla_{\mathbf{Z}} Z_i | \underline{M}\, \underline{J}\, \underline{\tilde{M}} | \nabla_{\mathbf{Z}} Z_j \rangle \\
&= \sum_{\mu,\nu,\rho,\sigma} [(\nabla_{\mathbf{Z}} Z_i)_\mu M_{\mu\nu}] J_{\nu\rho} [\tilde{M}_{\rho\sigma} (\nabla_{\mathbf{Z}} Z_j)_\sigma] \\
&= \sum_{\nu,\rho} M_{i\nu} J_{\nu\rho} \tilde{M}_{\rho j} \\
&= (\underline{M}\, \underline{J}\, \underline{\tilde{M}})_{ij}
\end{aligned}
\tag{A.1}
$$

The fundamental Poisson brackets relations are equivalent to our definition of a canonical transformation, Eq. 2.17c.

A.2 Discontinuity of Angle Variables

The discontinuity of the angle variable ϕ_2 will be shown here. We begin by noting that we have a canonical transformation

$$xyp_xp_y \rightarrow \phi_1\phi_2\mathcal{I}_1\mathcal{I}_2 \tag{A.2}$$

A generating function $G(\mathbf{q}, \mathbf{I})$ can be defined such that

$$\phi_k = \frac{\partial G}{\partial \mathcal{I}_k}, \quad p_k = \frac{\partial G}{\partial q_k} \tag{A.3}$$

Integrating the p_k term and noting that $\mathbf{q}$ can point in any direction (x, y) leads to

$$\begin{aligned}
G(\mathbf{q}, \mathbf{I}) &= \int_{\mathbf{q}_o}^{\mathbf{q}} p_k(\mathbf{q}', \mathbf{I})d\mathbf{q}_k + G(\mathbf{q}_o, \mathbf{I}) \\
&= \int \frac{\partial G}{\partial x}dx + \int \frac{\partial G}{\partial y}dy + G_o \\
&= \int \vec{\nabla}G \cdot d\mathbf{q} + G_o \\
&= \int \vec{\nabla}G \cdot d\mathbf{q} + \cancel{G_o}^{\,0} \\
&= \int \mathbf{p} \cdot d\mathbf{q}
\end{aligned} \tag{A.4}$$

Differentiating A.4 with respect to $\mathcal{I}_k$ and substituting A.3 for the left hand side gives

$$\phi_k = \int \sum_j \frac{\partial p_j}{\partial \mathcal{I}_k}dq_j \tag{A.5}$$

Doing this integral is simpler in polar coordinates (ρ, ψ). Doing the ϕ_2 integral A.5 and substituting polar coordinates

$$\phi_2 = \int \frac{\partial p_\rho}{\partial \mathcal{I}_2} d\rho + \frac{\partial \ell}{\partial \mathcal{I}_2}^{\nearrow 1} d\psi \tag{A.6}$$

$$= \int \left(\frac{\partial p_\rho}{\partial \mathcal{I}_2} \right) d\rho$$

$$\left(\frac{\partial p_\rho}{\partial \mathcal{I}_2} \right)_{\mathcal{I}_2} = \left(\frac{\partial p_\rho}{\partial H} \right) \left(\frac{\partial H}{\partial \mathcal{I}_2} \right)_{\mathcal{I}_1} + \left(\frac{\partial p_\rho}{\partial \ell} \right)^{\nearrow 0} \left(\frac{\partial \ell}{\partial \mathcal{I}_2} \right)_{\mathcal{I}_1} \tag{A.7}$$

We can now evaluate the integral. For simplicity, we will take the case $V(\rho) = 0$, knowing that our result is generalizable to the $h > 0$ case in the Mexican-hat. Also, noting that $\left(\frac{\partial H}{\partial \mathcal{I}_2} \right)_{\mathcal{I}_1} = \dot{\phi}_2$ is positive when $\ell > 0$ and negative for $\ell \leq 0$, we have

$$\phi_2 = \int \left(\frac{\partial p_\rho}{\partial H} \right) (\pm) d\rho$$

$$= (\pm) \int \frac{m}{\sqrt{2m \left(h - \frac{\ell^2}{2m\rho^2} \right)}} d\rho \tag{A.8}$$

$$= \frac{(\pm)\rho\sqrt{2mh - \frac{\ell^2}{\rho^2}}}{2h}$$

Taking the limit $\ell \to 0$ from the positive and negative sides

$$\lim_{\ell \to 0^+} \phi_2 = \rho\sqrt{\frac{m}{2h}}, \quad \lim_{\ell \to 0^-} \phi_2 = -\rho\sqrt{\frac{m}{2h}} \tag{A.9}$$

Therefore, ϕ_2 is discontinuous at $\ell = 0, h > 0$

A.3   Fundamental Poisson Brackets of New Action-Angle Variables

Here we prove that the adjusted action-angle variables defined in Eqs. 3.21 and 3.20 are canonical by calculating their fundamental Poisson brackets, see Eq. 2.29.

$$
\begin{aligned}
\left[\mathcal{I}_1', \phi_1'\right] &= [\mathcal{I}_1 - \mathcal{I}_2, \phi_1] = 1 - 0 = 1 \\
\left[\mathcal{I}_1', \phi_2'\right] &= [\mathcal{I}_1 - \mathcal{I}_2, \phi_1 + \phi_2] = 1 - 1 = 0 \\
\left[\mathcal{I}_2', \phi_1'\right] &= [\mathcal{I}_2, \phi_1] = 0 \\
\left[\mathcal{I}_2', \phi_2'\right] &= [\mathcal{I}_2, \phi_1 + \phi_2] = 0 + 1 = 1
\end{aligned}
\tag{A.10}
$$

Appendix B

Code for Experiment

B.1   Arduino Code

```
// voltages for each coil for each time step as determined
by matlab code
int CentC[] = {255,255,255,255,...
,225,225,225,225,225,225,225};
int TorqEW[] = {128,127,127,127,...
,131,130,130,129,128,128,128,128,128};
int TorqNS[] = {172,172,172,...
,172,172,172,172,172,172,172,172,172,172};

// the setup routine runs once when you press reset:
void setup() {
        // initialize the digital pin as an output.
        pinMode(12,OUTPUT); //center coil
        pinMode(DAC0, OUTPUT); // torque NS
        pinMode(DAC1,OUTPUT); // torque EW
        pinMode(7,OUTPUT); // starter coil
        pinMode(6,OUTPUT); // LED
```

```
}


// the loop routine runs over and over again forever:
void loop() {
        int del = 15238; //timestep in microseconds
        int phasedelay = 0; //increase delay time depending on
        choice of position on initial loop
        analogWrite(12,CentC[1]); //writing initial voltages
        digitalWrite(7,LOW);
        digitalWrite(6,HIGH);
        analogWrite(DAC0,TorqNS[1]);
        analogWrite(DAC1,TorqEW[1]);
        delay(30000);  //initial setup time
        digitalWrite(7,HIGH);
        delay(phasedelay);
        digitalWrite(6,LOW);
        for(int i = 1; i<6301;i++){     //new voltages for
        each timestep
                analogWrite(12,CentC[i]);
                analogWrite(DAC0,TorqNS[i]);
                analogWrite(DAC1,TorqEW[i]);
                delayMicroseconds(del);
        }


}
```

Bibliography

[1] J. J. Duistermaat, "On global action-angle coordinates", Commun. Pure Appl. Math. **33**, 687 (1980).

[2] R. Cushman and L. Bates, *Global aspects of classical integrable systems* (Springer, 1997).

[3] L. Bates and M. Zou, "Degeneration of hamiltonian monodromy cycles", Nonlinearity **6**, 313 (1993).

[4] H. Dullin, A. Giacobbe, and R. Cushman, "Monodromy in the resonant swing spring", Physica D: Nonlinear Phenomena **190**, 15 (2004).

[5] R. Cushman and J. J. Duistermaat, "The quantum mechanical spherical pendulum", Bull. Amer. Math. Soc. (N.S.) **19**, 475 (1988).

[6] R. Cushman and D. Sadovskií, "Monodromy in the hydrogen atom in crossed fields", Physica D **142**, 166 (2000).

[7] C. Schleif and J. Delos, "Monodromy and the structure of the energy spectrum of hydrogen in near perpendicular electric and magnetic fields", Phys. Rev. A **76**, 013404 (2007).

[8] C. Schleif and J. Delos, "Semiclassical theory of the structure of the hydrogen spectrum in near-perpendicular electric and magnetic fields: derivations and formulas for einstein-brillouin-keller-maslov quantization and description of monodromy", Phys. Rev. A **77**, 043422 (2008).

[9] K. Efstathiou, O. V. Lukina, and D. A. Sadovskií, "Most typical 1:2 resonant perturbation of the hydrogen atom by weak electric and magnetic fields", Phys. Rev. Lett. **101**, 253003 (2008).

[10] K. Efstathiou and D. A. Sadovskií, "Normalization and global analysis of perturbations of the hydrogen atom", Rev. Mod. Phys. **82**, 2099 (2010).

[11] H. Waalkens and H. R. Dullin, "Quantum monodromy in prolate ellipsoidal billiards", Ann. of Phys. **295**, 81 (2002).

[12] H. Waalkens, H. R. Dullin, and P. H. Richter, "The problem of two fixed centers: bifurcations, actions, monodromy", Physica D **196**, 265 (2004).

[13] M. S. Child, T. Weston, and J. Tennyson, "Quantum monodromy in the spectrum of h2o and other systems: new insight into the level structure of quasi-linear molecules", Molec. Phys. **96**, 371 (1999).

[14] I. N. Kozin and R. M. Roberts, "Monodromy in the spectrum of a rigid symmetric top molecule in an electric field", Journ. of Chem. Phys. **118**, 10523 (2003).

[15] C. A. Arango, W. W. Kennerly, and G. S. Ezra, "Quantum monodromy for diatomic molecules in combined electrostatic and pulsed nonresonant laser fields", Chem. Phys. Lett. **392**, 486 (2004).

[16] A. Giacobbe, R. H. Cushman, D. A. Sadovskií, and B. I. Zhilinskií, "Monodromy of the quantum 1:1:2 resonant swing spring", J. Math. Phys. **45**, 5076 (2004).

[17] R. H. Cushman, H. R. Dullin, A. Giacobbe, D. D. Holm, M. Joyeux, P. Lynch, D. A. Sadovskií, and B. I. Zhilinskií, "Co2 molecule as a quantum realization of the 1:1:2 resonant swing-spring with monodromy", Phys. Rev. Lett. **93**, 024302 (2004).

[18] H. Waalkens, "Quantum monodromy in trapped bose condensates", Europhys. Lett. **58**, 162 (2002).

[19] N. N. Nekhoroshev, D. A. Sadovskií, and B. I. Zhilinskii, "Fractional monodromy of resonant classical and quantum oscillators", Comp. Rend. Math. **335**, 985 (2002).

[20] N. N. Nekhoroshev, D. A. Sadovskií, and B. I. Zhilinskií, "Fractional hamiltonian monodromy", Ann. Inst. Henri Poincaré **7**, 1099 (2006).

[21] K. Efstathiou and D. Sugny, "Integrable hamiltonian systems with swallowtails", Journ. of Phys. A **43**, 085216 (2010).

[22] D. Sadovskií and B. Zhilinskií, "Hamiltonian systems with detuned 1:1:2 resonance: manifestation of bidromy", Ann. of Physics **322**, 164 (2007).

[23] E. Assémat, K. Efstathiou, M. Joyeux, and D. Sugny, "Fractional bidromy in the vibrational spectrum of hocl", Phys. Rev. Lett. **104**, 113002 (2010).

[24] P. Cejnar, M. Macek, S. Heinze, J. Jolie, and J. Dobeš, "Monodromy and excited-state quantum phase transitions in integrable systems: collective vibrations of nuclei", J. Phys. A **39**, L515 (2006).

[25] D. Sugny, A. Picozzi, S. Lagrange, and H. R. Jauslin, "Role of singular tori in the dynamics of spatiotemporal nonlinear wave systems", Phys. Rev. Lett. **103**, 034102 (2009).

[26] M. Kloc, P. Stránský, and P. Cejnar, "Monodromy in dicke superradiance", J. Phys. A **50**, 315205 (2017).

[27] J. Delos, G. Dhont, D. A. Sadovskií, and B. I. Zhilinskií, "Dynamical manifestation of hamiltonian monodromy", Europhys. Lett. **83**, 24003 (2008).

[28] C. S. J.B. Delos and G. Dhont, "Static and dynamical manifestations of hamiltonian monodromy", J. of Phys.: Conf. Ser. **99**, 012005 (2008).

[29] C. Chen, M. Ivory, S. Aubin, and J. B. Delos, "Dynamical monodromy", Phys. Rev. E **89**, 012919 (2014).

[30] M. Winnewisser, B. P. Winnewisser, I. R. Medvedev, F. C. D. Lucia, S. C. Ross, and L. M. Bates, "The hidden kernel of molecular quasi-linearity: quantum monodromy", Journ. Mol. Struct. **798**, 1 (2006).

[31] N. J. Fitch, C. A. Weidner, L. P. Parazzoli, H. R. Dullin, and H. J. Lewandowski, "Experimental demonstration of classical hamiltonian monodromy in the 1:1:2 resonant elastic pendulum", Phys. Rev. Lett. **103**, 034301 (2009).

[32] K. Efstathiou, R. Cushman, and D. Sadovskií, "Fractional monodromy in the 1:2 resonance", Advances in Mathematics **209**, 241 (2007).

[33] R. H. Cushman, H. R. Dullin, H. Hanßmann, and S. Schmidt, "The 1:2 resonance", Regular and Chaotic Dynamics **12**, 642 (2007).

[34] K. E. Henk Broer and O. Lukina, *A geometric fractional monodromy theorem*, 2010.

[35] J. Finn, *Classical mechanics*, Engineering series (Jones and Bartlett Publishers, 2009).

[36] V. Arnol'd, *Mathematical methods of classical mechanics*, Graduate Texts in Mathematics (Springer, 1979).

[37] W. Fulton, *Algebraic topology: a first course* (Springer, 1995).

[38] V. Arnol'd, *Geometrical methods in the theory of ordinary differential equations* (Springer New York, 1988).

[39] M. P. Nerem, D. Salmon, S. Aubin, and J. B. Delos, "Experimental observation of classical dynamical monodromy", Phys. Rev. Lett. **120**, 134301 (2018).

[40] T. Bergeman, G. Erez, and H. J. Metcalf, "Magnetostatic trapping fields for neutral atoms", Phys. Rev. A **35**, 1535 (1987).

[41] A. Savitzky and M. J. E. Golay, "Smoothing and differentiation of data by simplified least squares procedures.", Anal. Chem. **36**, 1627 (1964).

[42] V. G. Minogin, J. A. Richmond, and G. I. Opat, "Time-orbiting-potential quadrupole magnetic trap for cold atoms", Phys. Rev. A **58**, 3138 (1998).

[43] M. M., "Equations for the magnetic field produced by one or more rectangular loops of wire in the same plane", J. Res. Natl. Inst. Stand. Technol. **105** (2000).

[44] B. Zhilinskii, "Interpretation of quantum hamiltonian monodromy in terms of lattice defects", Acta Applicandae Mathematica **87**, 281 (2005).

[45] C. Chen and J. B. Delos, "Topological changes of wave functions associated with hamiltonian monodromy", Phys. Rev. E **97**, 062216 (2018).

[46] J. F. Rodriguez-Nieva and L. S. Levitov, "Berry phase jumps and giant nonreciprocity in dirac quantum dots", Phys. Rev. B **94**, 235406 (2016).